The impact of advection schemes on lateral shear and baroclinic instability

Dissertation zur Erlangung des Doktorgrades

an der Fakultät für Mathematik, Informatik und Naturwissenschaften

Fachbereich Geowissenschaften

der Universität Hamburg

vorgelegt von

Mahdi Mohammadi-Aragh

Hamburg, 2014

Tag der Disputation: 05.12.2014

Folgende Gutachter empfehlen die Annahme der Dissertation:

Prof. Dr. Hans Burchard

Prof. Dr. Carsten Eden

Eidesstattliche Erklärung

Hiermit erkläre ich an Eides statt, dass ich die vorliegende Dissertationsschrift - abgesehen von der Beratung durch meine akademischen Lehrer - selbst verfasst und keine anderen als die angegebenen Quellen und Hilfsmittel benutzt habe. Diese Arbeit hat weder ganz, noch in Teilen, bereits an anderer Stelle einer Promotionskommission zur Erlangung des Doktorgrades vorgelegen.

Hamburg, 06.10.2014

Acknowledgement

First and foremost I would like to express my special appreciation and thanks to my supervisors Prof. Dr. Hans Burchard and Prof. Dr. Carsten Eden for providing me with the opportunity to join their research team and supporting me with their invaluable advises. I highly appreciate the cooperation with Dr. Nils Brüggemann and Dr. Knut Klingbeil throughout the last years. I wish to thank the whole Coastal-Ocean-Physical-Processes group at the Institute of Baltic Sea Research for the very friendly atmosphere and for all wonderful moments that we had together in beautiful Warnemünde. Finally, I would like to dedicate this thesis to my beloved family for their love.

Zusammenfassung

Die vorliegende Arbeit quantifiziert an Hand idealisierter Experimente mit einem Ozeanmodell, zu lateraler Scherung und baroklinen Instabilitäten, die künstliche Dissipation und Mischung, die von verschiedenen Advektionsschemata hervorgerufen wird. Die Advektionsschemata werden nach ihrem dissipativen Verhalten kategorisiert, wobei verschiedenen Maße, wie z.B. die potentialle Hintergrundenergie und numerische Dissipation, zur Anwendung kommen. Derartige Analysen helfen, unter Abwägung von Genauigkeit und Rechenaufwand, bei der Entscheidnung zwischen sehr genauen und komplexen Schemata und weniger komplexen Schamata niedriger Ordnung. Als hochpräzise aber komplexe Schemata werden das *Weighted Essentially Non-Oscillatory (WENO)* und das *5-point-stencile Monotonicity Preserving (MP5)* Schema verwendet. Als Vergleich werden die *Total Variation Diminishing (TVD)* Schemata und einfache Upwind-Schemata verwendet. Eine genaue Analyse offenbart, dass das MP5 und das *SPL-max-$\frac{1}{3}$ (Symmetric Piecewise-Linear)* Schema die besten Ergebnisse liefern, wobei das MP5 Schema ungefär 2.3 mal numerisch aufwendiger ist als das SPL-max-$\frac{1}{3}$ Schema. Die verschiedenen Advektionsschemata verhalten sich sehr ähnlich bei Simulationen mit großen Rossby-Zahlen. Im Gegensatz dazu werden signifikante Unterschiede deutlich, wenn man Simulationen von baroklinischen Instabilitäten mit kleinen Rossby-Zahlen durchführt. Ein weiteres Hauptergebnis der vorliegenden Studie ist, dass eine global positive numerische Dissipation und positive potentielle Hintergrundenergie die vertikale Einschichtung der Wassersäule verzögern.

Abstract

This research quantifies spurious dissipation and mixing of several different advection schemes in some idealised experiments including lateral shear and baroclinic instabilities in the framework of one ocean model. The advection schemes are categorised based on their dissipative behaviour using several different methods such as background potential energy and numerical dissipation analysis. Such analyses help to choose between highly accurate but complex schemes and lower order less complex schemes balancing accuracy and computational costs. The Weighted Essentially Non-Oscillatory (WENO), the 5-point-stencil Monotonicity Preserving (MP5) advection schemes are used as highly accurate complex schemes. The Total Variation Diminishing (TVD) schemes and the simple upwind schemes as less complex advection schemes are also compared. The analyses show that the MP5 scheme and the SPL-max-$\frac{1}{3}$ (Symmetric Piecewise-Linear) as a TVD advection scheme provide the best results although the MP5 scheme is approximately 2.3 times more expensive than the SPL-max-$\frac{1}{3}$ scheme in this implementation. In contrast to the configuration of baroclinic instability test case with a small Rossby number, when significant differences between schemes become apparent, the different advection schemes behave similarly for a larger Rossby number. Another major outcome of the present study is that positive global numerical dissipation and positive background potential energy evolution delay the restratification process.

Contents

1 Introduction

Despite the enormous progress in the ocean modelling over the past decades, such as refined numerical schemes and increased computational resources, numerical inaccuracies are still one of the most prominent factors hampering quantitative analysis. This, specifically, is the case for analysis of turbulence, mixing and transport, processes which are often blurred by discretisation errors. Analysing one dimensional partial differential equations as a reasonable initial step for developing complicated multidimensional complex flow solvers, has revealed the complex characteristic of discretisation errors of the advection terms. These errors cause numerical mixing and dissipation in ocean models which are inseparable from turbulent mixing and dissipation.

The intensity of numerical mixing and dissipation highly depends on the method of discretisation, the resolution, the computation method of advective fluxes and the type of interpolation functions for computing interface value. Appropriate design of these parameters can increase the level of model predictability. In addition, improving the knowledge about the effects of numerical mixing and numerical dissipation on flow and transport of tracer can help to optimise the model and enhance the simulation results. In this research, the effects of several advection schemes on the development of flow are quantified in idealised numerical experiments for different dynamical regimes using various analyses and diagnostic methods.

1.1 Scientific background

It is well known that discretisation errors of the advection terms lead to spurious mixing and dissipation and may interact nonlinearly with parameterisations of turbulent mixing and transport. Hecht (2010), for example, attributes spurious cooling within and below the thermocline to interactions between dispersive centered tracer advection schemes and eddy parameterisations. Holland et al. (1998) discuss the local Gibb's phenomenon in the light of local anomalies due to overshooting and undershooting oscillations in the tracer field. Farrow and Stevens (1995) observe unphysical negative surface temperatures and spurious heating in some regions of an eddying Antarctic model. Griffies et al. (2000) suggest to minimise the amount of spurious diapycnal mixing in the ocean pycnocline by properly resolving the admitted scales of motion.

Lee et al. (2002) report excessive diapycnal fluxes and effective diffusion due to numerical mixing and suggest using less diffusive horizontal advection schemes and appropriate vertical resolution.

In ocean modelling, the first attempts to remove the stability problems of the simple central advection schemes have been to use more diffusive schemes. Holland et al. (1998), for example, discuss a simulation with a physically more realistic tracer pattern in a global model by using upstream schemes instead of central advection schemes. Similar methods dealing with the control of generation of spurious anomalies are now widely implemented in ocean modelling. The Flux Limiter Method (FLM; Sweby, 1984), the Flux-Corrected Transport (FCT) algorithm (Boris and Book, 1973; Zalesak, 1979) and the Piecewise Parabolic Method (PPM; Colella and Woodward, 1984) are examples. Notwithstanding the substantial progress, these schemes often suffer from diffusive or antidiffusive effects (e.g., Čada and Torrilhon, 2009). The WENO scheme (Liu et al., 1994) aims to minimise these problems by using a convex combination of all possible stencils for computing the interface value providing higher order accuracy in smooth regions and seeking the smoothest solution near discontinuities. MP5 (Suresh and Huynh, 1997) employs a five-point stencil in a complex geometric approach to approximate the advective flux. One of the aims of this research is to compare the effects of these two more recent schemes with the more established flux limited schemes.

Due to the lack of analytical solutions, the quantification of discretisation errors is difficult in complex three-dimensional model simulations. Following Winters et al. (1995) and Winters and D'Asaro (1996), the estimation of spurious diapycnal mixing from the variations in the background potential energy is suggested by Griffies et al. (2000). Getzlaff et al. (2010) compute effective diffusivity and Ilıcak et al. (2012) quantify the global spurious dianeutral transport. Urakawa and Hasumi (2014) quantify the numerical mixing in terms of spurious water mass transformation rates. Burchard and Rennau (2008), inspired by the work of Maqueda and Holloway (2006), quantify the local numerical mixing in terms of the local tracer variance decay induced by the advection scheme. This is generalised to a similar approach to quantify numerical dissipation as a kinetic energy loss due to the discretisation of the momentum advection (see Burchard, 2012; Klingbeil et al., 2014). In this thesis the energy variation due to both numerical dissipation and numerical mixing is investigated using the numerical dissipation (Klingbeil et al., 2014) and the background potential energy analyses (e.g., Winters et al., 1995).

1.2 Scientific goals and motivation

The performance of advection schemes are investigated in a wide range of fluid dynamic applications from engineering scales to large, synoptic scales (e.g. Gerdes et al., 1991; Hólm, 1995; Pietrzak, 1998; Winton et al., 1998; James, 2000; Wang and Hutter, 2001a; Namin et al., 2004; Fringer and Armfield, 2005; Maqueda and Holloway, 2006; Ezer, 2006). However, in oceanic applications, just a few advection schemes are used. Therefore, little is known about the effects of the modern complex advection schemes on oceanic flow. Despite this, the studies which compare the performance of advection schemes did not use a single ocean model for the comparison. For example, Ilıcak et al. (2012) use the PPM advection scheme from the Modular Ocean Model (MOM) and the Piecewise Linear Method (PLM) from the Generalised Ocean Layered Model (GOLD). Since the structures of ocean models are different, it is hard to attribute the observed differences in the results only to the performance of advection schemes. Furthermore, the numerical experiments suggested for the comparison in the literature are either designed for very specific conditions (e.g. fresh water patch; James, 1996) or they include complex physical processes that makes the investigation challenging (e.g., Rennau and Burchard, 2009). This indicates a need to introduce a set of numerical experiments for investigating the effects of advection schemes on development of flow for different dynamical regimes.

The diagnosis of numerical dissipation is applied to idealised re-entrant channel simulations of lateral and baroclinic shear instability under different dynamical conditions. Such configurations are also used to develop and to test eddy parameterisations (Fox-Kemper et al., 2008; Brüggemann and Eden, 2014). Since the validation of such parameterisations depends on numerical effects of advection schemes, investigating such effects is the central aim of this study. The advection schemes are initially categorised based on their dissipative behaviour performing two 2D numerical experiments. Then, the effects of the categorised advection schemes are investigated on baroclinic and lateral shear instabilities. 2D test cases add to the results of the simple 1D initial value problems in the literature because they analyse the performance of the numerical schemes in a full ocean model for a steady state and a turbulent flow. This provides insight into the more complex test case of baroclinic instability which is performed for small and large Rossby numbers solving both the momentum and tracer equations. For all setups the modern WENO and MP5 schemes are compared to popular TVD schemes and the simple third-order upwind scheme. This study provides an opportunity to advance the knowledge of numerically modelling lateral mesoscale and submesoscale processes. The proper choice of advection scheme might reduce the bias towards vertical fluxes of buoyancy. Consequently, for eddy-resolving ocean models, new effective mixing parameterisations can be derived and highly accurate results might be obtained. Therefore, the key research question of this study

is whether the new complex accurate advection schemes can reduce the numerical energy loss of the experiments, for different horizontal resolutions and different dynamical regimes, or not.

1.3 Outline of the thesis

The *first chapter* reviews the reports of numerical problems occurring in ocean models due to discretisation errors of advection schemes. The scientific background of the diagnostic methods and the development of advection schemes are briefed. The significance and the purpose of performing a set of simulations for lateral and baroclinic shear instabilities are explained. The *second chapter* explains the algorithms of several advection schemes which are developed to fulfil accuracy and to minimise the associated numerical problems. The advection schemes are presented in three groups based on the type of errors occurring in a 1D solution of the advection equation. The *third chapter* introduces the equations of motion and corresponding approximations appropriate for large-scale oceanic flow. The recent methods in the literature for diagnosing and quantifying the numerical dissipation and mixing are reviewed. The presented methodology is designed in a way that first the advection schemes are categorised based on their dissipative or diffusive behaviour. Then their effects on instability processes are studied. This chapter connects the physical meaning of the main properties of the flow, e.g. viscosity to the numerical concepts of same quantities, e.g. numerical viscosity. The *fourth chapter* introduces a new system of steady state eddies with an approximation of the water elevation, the Honeycomb test case, for analysing the dissipative behaviour of the advection schemes. The *fifth chapter* is devoted to the numerical effects on lateral shear and baroclinic instabilities. The lateral shear experiment adds to the results from the Honeycomb experiment because it solves turbulent flow including sharp discontinuities in the initial velocity field. The baroclinic instability experiment is a more realistic 3D flow solving both momentum and tracer equations. This experiment is configured for two cases with small and large Rossby numbers. *Chapters 6 and 7* provide a summary and an outlook for future works.

Parts of this thesis have already been submitted for publication:

- Mohammadi-Aragh, M., Klingbeil, K., Brüggemann, N., Eden, C. and Burchard, H., 2014. Submitted: The impact of advection schemes on lateral shear and baroclinic instability. Ocean Modelling.

2 Evolution and development of advection schemes

2.1 Introduction

The focus of this chapter is on reviewing the development of different Eulerian-based advection schemes on a regular uniform grid from very simple first order upwind schemes to complex geometric algorithms (for irregular and unstructured grids, see e.g. Spekreijse, 1987; Friedrich, 1998; Burbeau et al., 2001; Wang et al., 2008; Shu, 2003). The main numerical problems due to discretisation errors of advection terms are introduced and the methods for removing or minimising them are discussed.

Nearly all of the fundamental mathematical research for developing new advection schemes starts off with considering a very simple initial value problem with a constant velocity field and an equidistant grid of points with the aim to improve the spatial discretisation methods and interpolation functions. It is demonstrated by Hirsch (2007) that improving time integration methods does not remove the well known numerical errors of advection schemes, e.g. oscillation near an extremum. If this principle is generalised to three dimensional flow solvers, the customary explicit discretisation method used for solving the advection terms in ocean models is not likely to be the source of the observed numerical problems. Nevertheless, the numerical models in geoscience application, e.g. Numerical Weather Prediction (NWP), need appropriate methods for high resolution setups with timely simulations. The computation costs of such simulations are very high for explicit discretisation method. Therefore, the leapfrog scheme, i.e. a simple central time integration, Lagrangian or semi-Lagrangian schemes might be alternatively chosen (for more discussion and details of Lagrangian and semi-Lagrangian see the comprehensive review of Staniforth and Côté, 1991). These methods, despite their fast algorithms, might not be appropriate for long simulations, e.g. ocean modelling, because the leapfrog scheme shows dispersion errors, the Lagrangian method might not be able to represent the main characteristics of the flow due to highly irregular final spaced set and the semi-Lagrangian method is suffering from the lack of conservation of quantities, e.g. mass (see e.g., Zerroukat et al., 2002, 2005). Therefore, this study is confined to an ocean model

with explicit discretisations.

In addition to the accuracy problem of advection schemes in long term simulations (see section 2.2), simple high order advection schemes generate oscillating solutions near an extremum (see section 2.3). The oscillations do not reflect relevant physical meaning of quantities, e.g. temperature. Negative values, or values out of the acceptable range are generated. In this chapter some of the approaches that remove or minimise these effects are reviewed. These methods are categorised in two groups. The methods in the first group control the generation of oscillations, e.g. the Total Variation Diminishing (TVD) schemes (see section 2.5) and those in the second group seek the least oscillative solution, e.g. the WENO scheme (see section 2.6). To ensure that the schemes do not generate oscillation, it is necessary that the condition of TVD is fulfilled (see section 2.2). In addition to this classification, the advection schemes, according to Zalesak (1987) and Yang and Przekwas (1992) categorisation, as reviewed by James (1996) and Pietrzak (1998), are divided in two groups of algebraic schemes and geometric schemes. The first group generally combines the lower order schemes with higher order schemes to reconstruct interpolation functions (see section 2.5) and the latter uses subcell curves to approximate the fluxes (see section 2.6). Although the development of these schemes is originated from different logical concepts, they might finally show mathematically equivalent schemes. Readers are referred to the work of Thuburn (1997) for similarity between TVD-schemes and Positive Schemes and the work of Spekreijse, 1987 and Berger et al., 2005 for similarities between SLM and FLM.

2.2 First order advection schemes

The discretisation of the advection equation

$$\frac{\partial S}{\partial_t} + u\frac{\partial S}{\partial_x} = 0, \tag{2.1}$$

can be written as:

$$S_i^{n+1} = \sum_j b_j S_{i+j}^n, \tag{2.2}$$

where S_i and b_i, n and u are tracer concentration, a nonlinear function for grid cell i, the current time step and the velocity, respectively. Figure 2.1 illustrates the relation between the concentration of computational cells in a general two time level scheme. Based on this approach, for example, the first and simplest discretisation of the 1D advection equation is

the First Order Upwind (FOU) scheme, written as:

$$S_i^{n+1} = crS_{i-1}^n + (1 - cr)S_i^n, \tag{2.3}$$

where cr is the Courant number. The first order advection schemes are not suggested for

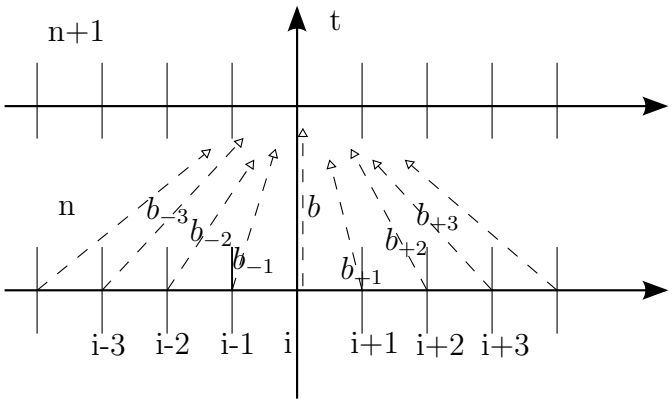

Figure 2.1: Explicit advection schemes compute the concentration of the computational cell S_i^{n+1} at time step $n + 1$ from the concentration of the neighbour computational cells at time step n. b_i is a nonlinear function which specifies the contribution of S_i^n in the new solution S_i^{n+1}. The vertical and horizontal axes are the time and space axes, respectively. This sketch is reproduced from Hirsch (2007).

ocean modeling, because their central scheme with forward time difference is unconditionally unstable and very noisy, their First Order Upwind (FOU) scheme is very diffusive due to discretisation errors and is consequently useless for long-term unsteady problems (e.g., Hirsch, 2007). Figure (2.2.a) compares the results of an initial value problem using the FOU scheme with analytical solution. The result shows that the FOU scheme is very diffusive.

2.3 High order advection schemes

Higher order schemes can fulfill the accuracy concept better than the first order schemes. Nevertheless, there are still some numerical errors. The second order schemes, e.g. the Lax-Wendroff scheme does not generate physical meaningful oscillation and phase errors next to discontinuities or extrema. Figure (2.2.b) compares the results of an initial value problem using a third order upwind scheme with analytical solution. It shows that increasing the spatial order of advection schemes does not remove the errors. Crowley (1968), for instance, developed first, second and forth order schemes of concentration equation in advective and flux form and Tremback et al. (1987) generalised that method to the order of ten. Nevertheless, oscillations might still be generated.

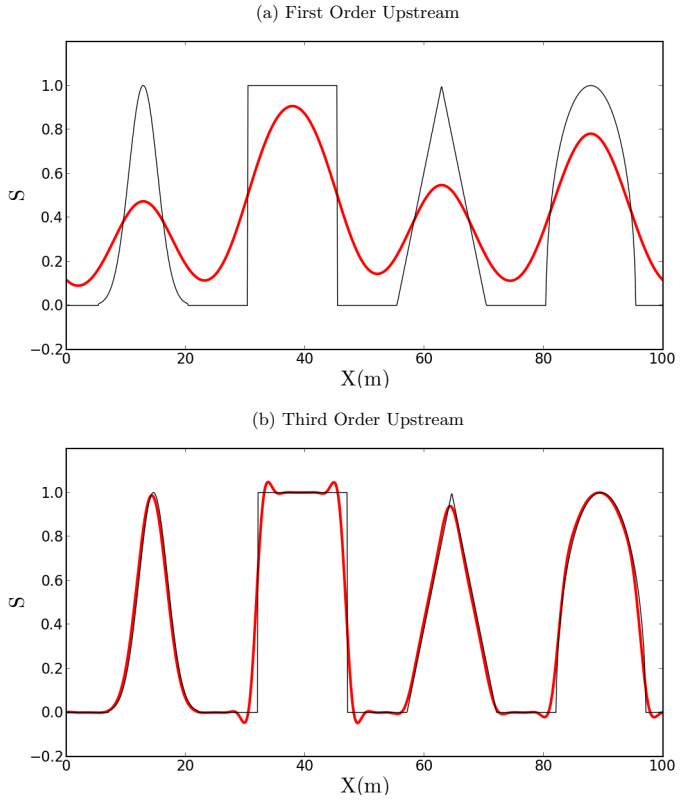

Figure 2.2: 1D advection transport problem with periodic boundaries, $cr = 0.5$, 1000 grid cells using a) the FOU scheme and b) the third order upstream scheme over three periods. The FOU scheme is diffusive and the third order upwind scheme generate oscillation and phase errors. The black line is the analytical solution.

2.4 Monotonicity, total variation diminishing and positive definite functions

Monotonicity condition are introduced to ensure that the advected quantities such as salinity and density have a relevant physical meaning. "A method is monotonicity preserving if it will preserve monotone-increasing or monotone-decreasing initial data" (Durran, 2010). The generation of oscillations increases the total variation

$$TV(S) = \sum_{i=1}^{M} |\Delta S|, \tag{2.4}$$

where M is the number of computational cells in a one dimensional row and $\Delta S = S_i - S_{i-1}$. If the total variation satisfies

$$TV\left(S^{n+1}\right) \leq TV\left(S^{n}\right) \qquad \text{for all } n, \tag{2.5}$$

the numerical scheme is Total Variation Diminishing (TVD) and the monotonicity condition is fulfilled. In addition to TVD schemes, Total Variation Bounded (TVB) schemes, fulfilling

$$TV\left(S^{n+1}\right) \leq \text{const.} \qquad \text{for all } n, \tag{2.6}$$

provide less restrictions and let schemes be more accurate. However, a scheme which is TVD is certainly TVB as the total variation ($TV\left(S^{n+1}\right)$) of the scheme is bounded to its initial value (e.g., Leveque, 2002; Shu, 1987). In addition to TVD schemes, the positive-definite advection schemes are introduced to generate physically plausible results. The positive-definite schemes like monotone schemes do not produce negative values from positive values and the positive define quantities remain positive through the whole advection process (e.g., Bott, 1988; Smolarkiewicz, 1984). However, there is no straightforward relation between TVD and monotonicity preserving schemes and positive-definite schemes (Durran, 2010).

2.5 Algebraic schemes

2.5.1 Filling algorithms and uniform viscosity

The simplest approach for removing the induced numerical oscillations in ocean models is substituting negative values occurred in the numerical solution for zero, namely, filling algorithms. This approach failed because it violates the mass conservation in the system. To fix that, for each occurring negative value that is changed to zero, somewhere else a positive value should be reduced to keep the scheme conservative. In addition, ocean modelers generally introduce viscosity uniformly to the model to remove or reduce oscillations. Introducing viscosity smoothes the gradients of scalar or vector quantities in other regions.

2.5.2 Boundary conditions and artificial viscosity

The other attempt to avoid oscillations, as reviewed by Hirsch (2007), is to implement boundary conditions on two sides of a discontinuity. This technique is used in engineering applications and is very complicated because the shock surfaces are in motion relative to the grids of the differential equation and boundary conditions are nonlinear. Later, the concept of artificial viscosity is introduced by VonNeumann and Richtmyer (1950) as an alternative to implement-

ing boundary conditions to ignore the presence of a discontinuity. Artificial viscosity damps the shock and makes the discontinuity smoother. The dissipative mechanism is presented by adding a new term in the pressure, which has a considerable value when is near the discontinuity. This concept which is expanded also by Lax and Wendroff (1960) is considered the omitted quadratic term when there is discontinuity. The coefficient of this term is called artificial viscosity because it appears in the equations similar to the artificial terms deployed by VonNeumann and Richtmyer (1950).

2.5.3 Flux Corrected Transport (FCT)

The flux Corrected Transport (FCT) technique, after some efforts of using artificial viscosity, is introduced by Boris and Book (1973) (see also Book et al., 1975; Boris and Book, 1976; Zalesak, 1979; Patnaik et al., 1987). The FCT technique is originally proposed to modify the solution of second order schemes. Each FCT technique consists of three operations namely, transport, diffusion and antidiffusion. The transport stage (might be simultaneous with diffusion stage) can be any kind of diffusive and dispersive finite differential scheme. Then, an antidiffusion operation is designed in a way that sufficient antidiffusion is introduced everywhere to eliminate or reduce numerical effects, although it is desirable to know where and how much antidiffusion should be applied. The simplest antidiffusion is computed in the SHASTA scheme (Sharp And Smooth Transport Algorithm; a simple explicit geometric interpretation that considers the solution as initial concentration function but with shifted position; Boris and Book, 1973) with setting velocity to zero in a second order scheme and considering the remaining diffusion type terms with opposite sign as antidiffusion. Thus, it is expected that the original fluxes are limited or corrected without generating new extrema, although the results might be very sensitive to antidifussion operation and it might insert other kind of numerical errors to the model. The reader is referred to the works of Gerdes et al. (1991) and Griffies et al. (2000) for the performance of FCT in ocean models.

2.5.4 Hybrid methods

Simultaneous with FCT, Harten and Zwas (1972) suggested hybrid methods as the approaches that gains monotonicity from combining a monotone advection scheme and a higher order advection scheme. This method suggests an algorithm which switches automatically and smoothly from higher order scheme to the monotone scheme in case of a discontinuity or when a global value like background potential energy is reduced or increased from the initial value (e.g., Fringer and Armfield, 2005).

2.5.5 Flux Limiter Method (FLM)

An extension to the hybrid methods, the Flux Limiter Method (FLM), is systemically explained by Sweby (1984). FLM is very similar to FCT and deploys a first order monotone scheme and an antidiffusion flux. However, FLM is a single-step procedure while FCT is at least a two-step algorithm. According to Hirsch (2007), the discretised higher order advection scheme (e.g., Lax Wendroff)

$$S_i^{n+1} = \underbrace{S_i^n - cr\left(S_i^n - S_{i-1}^n\right)}_{\text{Monotonic}} - \underbrace{FL\left(r\right)\left(\frac{1}{2}\left(1-cr\right)cr\left(S_i^n - S_{i-1}^n\right) - \frac{1}{2}\left(1-cr\right)cr\left(S_{i-1}^n - S_{i-2}^n\right)\right)}_{\text{Antidiffusive Flux}}, \tag{2.7}$$

is reformulated as a combination of a first order monotone scheme and an additional nonlinear term (antidiffusive flux) which is multiplied by a flux limiter function, $FL\left(r\right)$. The flux limiter function is designed in a way that the limited antidiffusive flux makes the scheme TVD and the advection scheme has the most possible nonlinearity property. The flux limiter is a function of successive gradients, r_i,

$$r_i \equiv \frac{S_{i+1} - S_i}{S_i - S_{i-1}} \leq 1, \tag{2.8}$$

which should remain less than unity to fulfill the first monotonicity condition. The left sketch of the figure 2.3 shows that r is positive and the monotonicity condition is satisfied. On the other hand, the successive gradient seen in the right sketch is negative, and shows the general pattern of numerical oscillation. In addition, it is shown that any limiter function has to satisfy

$$0 \leq \frac{FL\left(r\right)}{r} \leq 2, \tag{2.9}$$

and

$$0 \leq FL\left(r\right) \leq 2, \tag{2.10}$$

to make the scheme TVD. This TVD constraint for FLM is illustrated in Figure 2.4 in a $r - \mathrm{FL(r)}$ domain. Although using a FLM scheme improves the numerical solution to some extend and does not let oscillations be generated in the solution, the TVD schemes suffer from smearing and squaring effects. Figure 2.5, shows the results of a 1D simulation of advection transport problem using two different FLM schemes. Figure 2.5.a shows that the sharp edges of the solution are smeared, so called smearing effect. Figure 2.5.b shows that the smooth

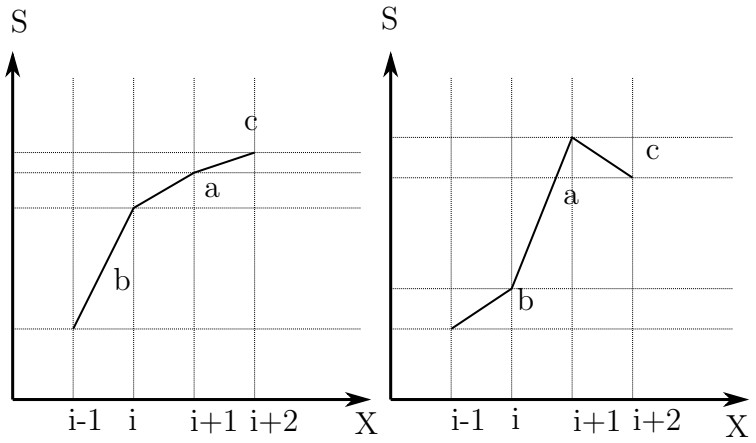

Figure 2.3: The left and right panels compare the monotonic and nonmonotonic solutions, respectively. The successive gradient r_i is used to diagnose the monotonic and nonmonotonic zones. r_i for the left and right panels are negative and positive, respectively. $a = S_{i+1} - S_i$, $b = S_i - S_{i-1}$ and $r_i = \frac{a}{b}$. This sketch is reproduced from Hirsch (2007).

extrema are gradually changed to edgy corners, so called squaring effect. Wang and Hutter (2001b) compare the efficiency of some advection schemes including first order schemes, not limited second order schemes, third order advection schemes, one FCT scheme, the most frequently applied TVD schemes and the modified TVD-schemes regarding their numerical diffusivity, and the production of spurious oscillations for convective dominated problems. It is concluded that for all schemes a refinement of the grid size decreases the errors. It is shown that for high resolution simulations FCT does not show any advantages to the third order schemes and the modified TVD scheme is the most competent method.

2.5.6 Godunov's scheme

The first order finite-volume conservative method suggested by Godunov (1959) is the basis of a new series of effective higher order schemes to solve the Riemann problems, i.e. a conservation law together with piecewise constant data including a single discontinuity e.g., discretised domains at grid interfaces (see e.g., Van Leer, 1984).

2.5.7 Essentially Non-Oscillatory (ENO) scheme

Harten et al. (1987) introduce a class of nonlinear high order schemes, Essentially Non-Oscillatory (ENO) schemes, as an extension to the Godunov scheme. The central idea of ENO is to select a certain number of adjacent computational cells for a stencil using a smoothness function (the function that diagnose the local smoothness of the interpolation function) to reconstruct the smoothest possible interpolation function. Using such an interpolation func-

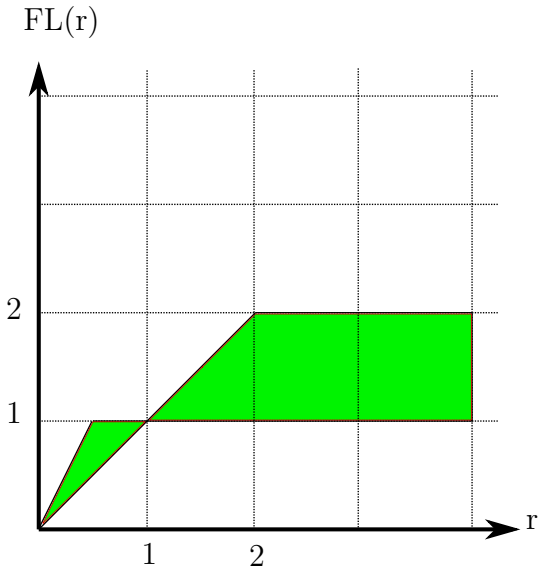

Figure 2.4: The permissible region for flux limiter functions to make higher order advection schemes TVD schemes.

tion to approximate the advective fluxes generates higher order accuracy in smooth regions and prevents oscillations at discontinuities. The freely adaptive stencil feature of ENO and its high sensitivity to very small perturbations in the order of machine round-off might cause that algorithm to make mistake in designing the most appropriate stencil.

2.5.8 Weighted Essentially Non-Oscillatory (WENO) scheme

As a remedy for the drawback of the ENO (see section 2.5.7) method to reduce the cost of the algorithm for seeking the most appropriate stencil in ENO, a new version of ENO, the Weighted Essentially Non-Oscillatory (WENO) scheme is suggested (Liu et al., 1994). Each individual stencil $(St_r(i), r = 0, \ldots, k-1)$ among k possible candidate stencils produces an interpolation function for approximating the interface value $S^r_{i+1/2}$ which is used for approximating the fluxes (see figure 3.3). WENO deploys a convex combination

$$S_{i+1/2} = \sum_{0}^{k-1} \omega_r S^r_{i+1/2}, \tag{2.11}$$

of all approximated interface values as the final approximation of the interface value $S_{i+1/2}$. The nonlinear weights ω_r have the following properties

$$\omega_r = \frac{\alpha_r}{\sum_{m=0}^{k-1} \alpha_m}, \quad r = 0, \ldots, k-1, \quad \omega_r \geq 0, \quad \sum_{r=0}^{k-1} \omega_r = 1, \tag{2.12}$$

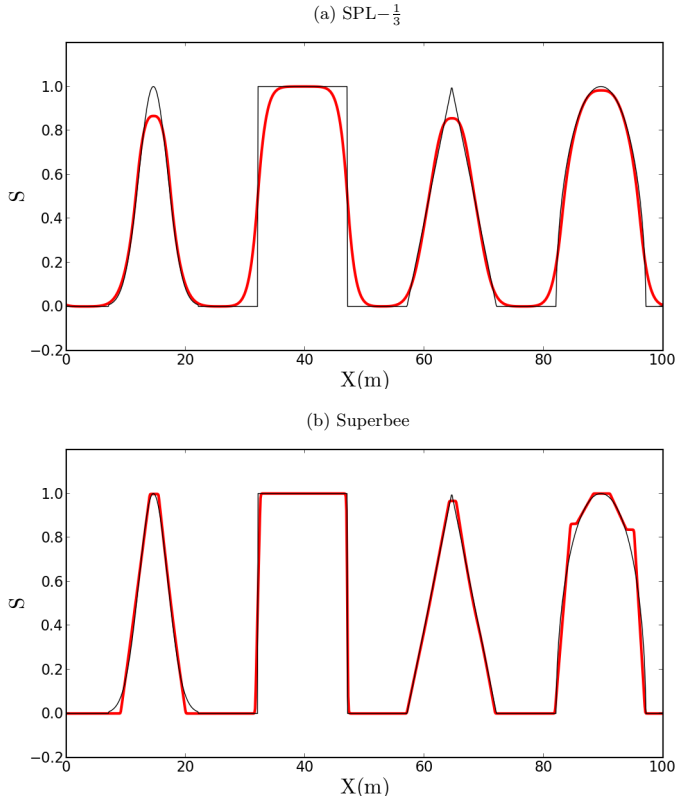

Figure 2.5: 1D advection transport problem with periodic boundary, cr = 0.5, 1000 cells using a) the SPL-$\frac{1}{3}$ scheme b) the Superbee scheme over 21 periods. The SPL-$\frac{1}{3}$ scheme causes smearing effect the Superbee scheme causes squaring effect. The black line is the analytical solution.

where

$$\alpha_r = \frac{d_r}{(\epsilon + \beta_r)^2}, \quad d_r > 0, \quad \sum_{r=0}^{k-1} d_r = 1, \tag{2.13}$$

are computed from the relative local smoothness measurement of interpolation functions, β_r. The smoothness measurement is designed so that the scheme provides a higher order of accuracy in smooth regions and minimises the effect of the stencil which includes discontinuity. Table 2.1 summarises the parameters used in this research for $k = 3$. β_r, for $k = 3$, is computed as follows:

$$\beta_0 = \frac{13}{12}\left(S_i - 2S_{i+1} + S_{i+2}\right)^2 + \frac{1}{4}\left(3S_i - 4S_{i+1} + S_{i+2}\right)^2, \tag{2.14}$$

$$\beta_1 = \frac{13}{12}\left(S_{i-1} - 2S_i + S_{i+1}\right)^2 + \frac{1}{4}\left(S_{i-1} - S_{i+1}\right)^2, \tag{2.15}$$

$$\beta_2 = \frac{13}{12}\left(S_{i-2} - 2S_{i-1} + S_i\right)^2 + \frac{1}{4}\left(S_{i-2} - 4S_{i-1} + 3S_i\right)^2 \tag{2.16}$$

In general, the WENO scheme is more stable than ENO and their resulting fluxes are smoother

ϵ	d_0	d_1	d_2
10^{-6}	$3/10$	$3/5$	$1/10$

Table 2.1: The resolutions and parameters used in the baroclinic test case.

(Shu, 2003). The abundant suggestions for computing the combination weights show the sensitivity of the approximated fluxes to β_r. In contrast to the earlier reviewed one-step schemes, the effective ENO (e.g., Shu and Osher, 1988, 1989) schemes and the WENO schemes are discretised in semi-discrete (separated time and spatial integration) format using TVD-Runge-Kutta time-marching schemes (e.g., Gottlieb and Shu, 1998; Gottlieb et al., 2001). This increases the costs of computation, but provides better accuracy. Figure 2.6.a illustrates that the WENO scheme does not cause smearing and squaring effects.

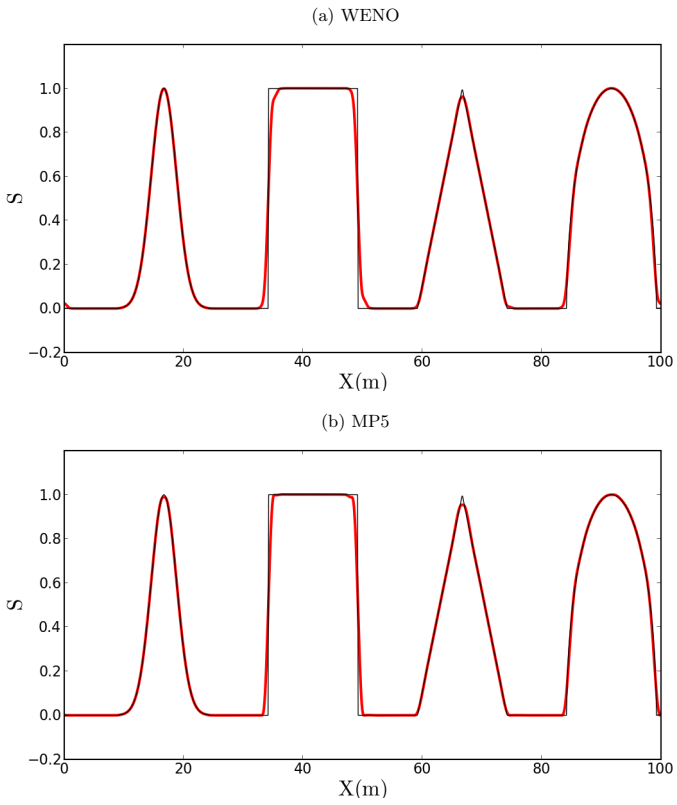

Figure 2.6: 1D advection transport problem with periodic boundary, cr = 0.5, 1000 cells using a) the WENO scheme b) the MP5 scheme over 21 periods. Smearing and squaring effects are not observed. The black line is the analytical solution.

2.6 Geometric schemes

Geometrical algorithms include three steps, namely reconstruction, involvement and remapping (see e.g., Van Leer, 1973). First, a one-dimensional Lagrangian curve is reconstructed. Then, the curve evolves and finally, slope limited (i.e. using the Slope Limiter Method; SLM) interface values are computed from remapping the final curve onto the Eulerian grid. The interface fluxes are approximated by solving Riemann problems at grid interfaces. The new generation of geometric schemes substitute higher order curves for the existing subcell curve. Van Leer's scheme (Monotone Upstream-centered Schemes for Conservation Laws; MUSCL), for example, is in fact an improved Godunov's scheme by substituting a piecewise subcell linear curve for a constant value. Similarly, the Piecewise Parabolic Method (PPM) (Colella and Woodward, 1984; Colella and Sekora, 2008), the Parabolic Spline Method (PSM) (Zerroukat et al., 2006) and the Quadratic Spline Method (QSM) (Zerroukat et al., 2010) are examples for attempts to improve the method by deploying higher order subcell interpolation function and introducing new slope limiters. The main drawbacks of the SLM schemes are the degeneration to first order scheme near an extremum. This problem is solved effectively by the work of Suresh and Huynh (1997) (see section 2.6.2).

2.6.1 Slope Limiter Method (SLM)

Van Leer (1973) as a pioneer of developing advection schemes in a geometrical framework introduces the basics of Slope Limiter Method (SLM) by explaining how introducing viscosity can tune the Lax-Wendroff scheme. The numerical tests and analyses present the limitations for the viscosity, q, to keep the Godunov's scheme

$$S_i^{n+1} = S_i^n - cr/2\left(S_{i+1}^n - S_{i-1}^n\right) + q/2\left(S_{i+1}^n - 2S_i^n + S_{i-1}^n\right) \tag{2.17}$$

stable and monotone. The condition for numerical stability and monotonicity is that the viscosity satisfies the following conditions:

$$cr^2 \leq q \leq 1 \tag{2.18}$$

and

$$|cr| \leq q \leq 1. \tag{2.19}$$

Figure 2.7 shows all possible monotonic and non-monotonic results of the Lax-Wendroff scheme (Van Leer, 1973). Each black curve is a parabola which is fitted to the points. A viscosity less

than the Courant number causes the fitted parabola curve through three adjacent points in the potential non monotonic region to dip under (over) the minimum (maximum) level of the points, respectively. Figure 2.7 demonstrates that for a smoothness coefficient (co) between -1 and 1, the parabola dedicated to the Lax-Wendroff (LW) dips under LL line (the black horizontal line) which shows the lowest level of the three points. For smoothness coefficient

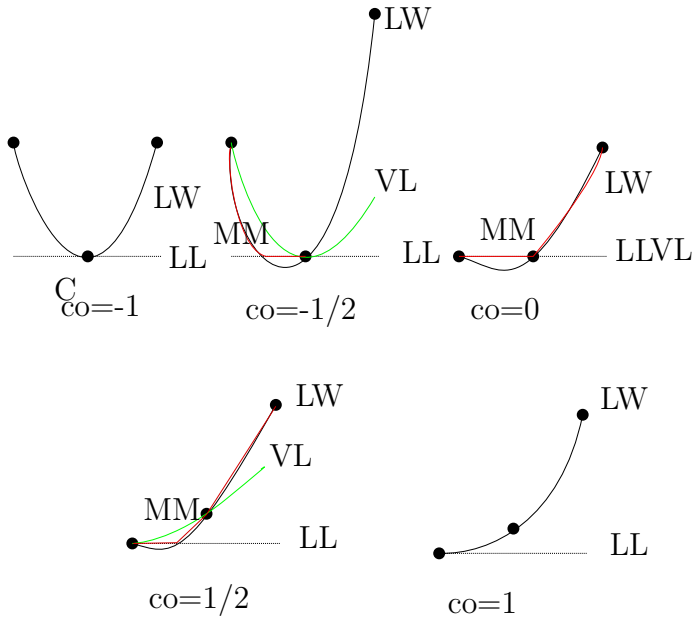

Figure 2.7: The non-monotonic zone of Lax-Wendroff scheme. This sketch is reproduced from Van Leer (1973). In this figure, *co* is the smoothness coefficient characterised by $\mathrm{co} = 2\left(S_i^n - S_{i-1}^n\right) / \left(\left(S_{i+1}^{n+1}\right) - \left(S_{i+1}^n - S_{i+1}^n\right)\right)$.

equal to 1 and -1 and smoothness coefficients out of this range, the curve is just tangent to the LL line and the advection scheme does not generate oscillations. There are no reasons to accept that such lower values occur in the exact solution. Therefore, a monotone curve must be substituted for the LW curve to enhance monotonicity (Van Leer, 1973). The very first idea is to get the MM curve (mean mod curve, the red line) as an alternative for LW when it goes lower than LL, but according to the idea of implementing nonlinearity it is better to apply a curve (VL; Van Leer curve; the green line) above the LW curve. The simplest one is a curve which is tangent to the LL line and goes through two adjacent points. In addition, the VL curve fits to the LW curve in case that the coefficient is in the range of -1 and 1. Therefore, the proposed scheme can be reformulated for the non-monotonic area as follows:

$$S_i^{n+1} - S_i^n = -cr^2\left(S_i^n - S_{i-1}^n\right) \qquad -1 < co < 0, \tag{2.20}$$

and

$$S_i^{n+1} - S_i^n = -cr\,(2 - cr)\left(S_i^n - S_{i-1}^n\right) \qquad 0 \leq co < 1. \tag{2.21}$$

To keep the nonlinearity (higher accuracy) and monotonicity properties, it is suggested to apply a curve tangent to the horizontal line passing from the target point and going through two other points which is possible by selecting appropriate viscosity. Thus, this scheme is the same as substituting q for the term $cr\,(1 - cr)\,(1 - |co|)$ in case of $|co| < 1$.

2.6.2 Five point-stencil Monotonicity Preserving (MP5) scheme

Suresh and Huynh (1997) introduce a new limiting geometric algorithm using a five-point stencil due to the fact that at least five points are needed to distinguish between an extremum and a discontinuity (see figure 2.8). This method introduces a new monotonicity preserving algorithm that does not degenerate the accuracy into the accuracy of a first order scheme near an extremum. Figure 2.6.b illustrates that MP5 provide high accuracy and does not cause smearing and squaring effects. Following Suresh and Huynh (1997) some definitions are presented as follows:

$$I[S_i, \ldots, S_{i+M}] = [\min(S_i, \ldots, S_{i+M}), \max(S_i, \ldots, S_{i+M})], \tag{2.22}$$

and

$$\operatorname{minmod}(x, y) = \frac{1}{2}(\operatorname{sgn}(x), \operatorname{sgn}(y)) \min(|x|, |y|), \tag{2.23}$$

and

$$\operatorname{median}(x, y, z) = x + \operatorname{minmod}(y - x, z - x), \tag{2.24}$$

where M is here the number of computational cells in the stencil. In addition, $\operatorname{sgn}(x)$ is equal to 1 if $x > 0$, -1 if $x < 0$ otherwise it is equal to zero. Similar to the other geometric methods, the MP5 scheme consists of two steps. In the first step, the reconstruction step, the original interface values of the left side and right side of the interface are computed. The final limited interface values are determined based on the point value in upwind direction or solving the Riemann problem. In this section, just the reconstruction and limiting algorithms of the left original interface value are reviewed. The right interface value is computed with the same approach but using a shifted stencil. In the first stage the original interface value

$$S_{i+1/2} = (2S_{i-2} - 13S_{i-1} + 47S_i + 27S_{i+1} - 3S_{i+2}), \tag{2.25}$$

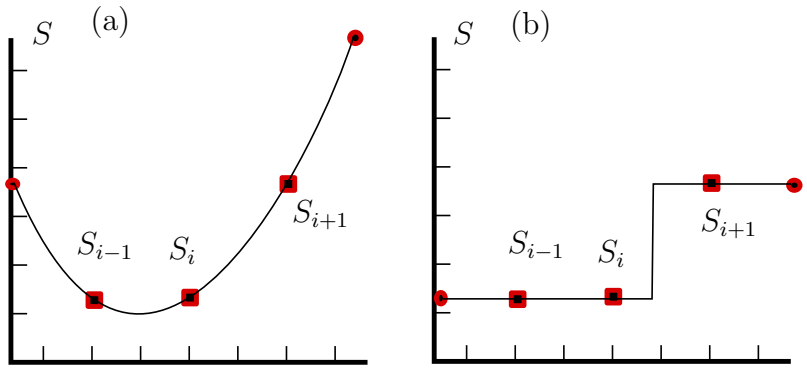

Figure 2.8: The three identical values S_{i-1}, S_i and S_{i+1} in (a) and (b) resemble an extremum and a discontinuity, respectively. This sketch is reproduced from Suresh and Huynh (1997).

is approximated using a fourth order polynomial. Moreover, a mth order ENO scheme can also be used for higher order schemes. For example, for m=4,

$$S_{i+1/2} = \left(-3S_{i-3} + 25S_{i-2} - 101S_{i-1} + 319S_i + 214S_{i+1} - 38S_{i+2} + 4S_{i+3}\right)/420, \qquad (2.26)$$

is obtained from a seven-point stencil. In the second step, a geometric monotonicity preserving

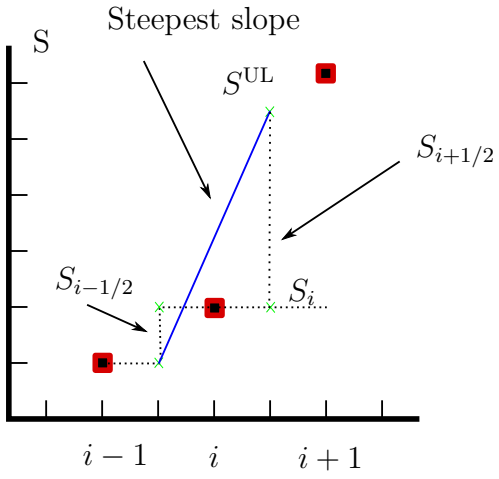

Figure 2.9: For monotonicity it is necessary that $S_{i-1/2} \in I\left[S_{i-1}, S_i\right]$ and $S_{i+1/2} \in I\left[S_i, S^{\mathrm{UL}}\right]$. This sketch is reproduced from Suresh and Huynh (1997).

algorithm is used. Figure 2.9 illustrates the monotonicity preserving constraints. It is assumed that

$$S_{i-1/2} \in I\left[S_{i-1}, S_i\right], \qquad (2.27)$$

and

$$S_{i+1/2} \in I\left[S_i, S^{UL}\right], \tag{2.28}$$

where S^{UL}, the upper limit value at the interface $i+1/2$ is extrapolated linearly

$$S^{UL} = S_i + \alpha\left(S_i - S_{i-1}\right). \tag{2.29}$$

It is shown (Suresh and Huynh, 1997) that the first Runge-Kutta intermediate value of S_i is located between S_{i-1} and S_i in case that $cr \leq 1/(1+\alpha)$. For Runge-kutta time stepping, $\alpha = 4$ is suggested (Suresh and Huynh, 1997). Since substituting i with $i+1$ implies that

$$S_{i+1/2} \in I\left[S_i, S_{i+1}\right], \tag{2.30}$$

(2.28) and (2.30) cause $S_{i+1/2}$ to be located in the interval $I\left[S_i, S^{\mathrm{MP}}\right]$ where

$$S^{\mathrm{MP}} = S_i + \mathrm{minmod}\left(S_{i+1} - S_i, \alpha\left(S_i - S_{i-1}\right)\right), \tag{2.31}$$

is the median of S_i, S_{i+1} and S^{UL}. To fulfill the monotonicity preserving condition, the original interface value is fitted into the interval $I\left[S_i, S^{\mathrm{MP}}\right]$ by substituting the median of $S_{i+1/2}$, S_i and S^{MP} for $S_{i+1/2}$. for the proof of the monotonicity see work of Suresh and Huynh (1997). However, the resultant monotonicity similar to the previous advection schemes degenerates the accuracy near an extremum to first order by determining the interface value by the upwind point value. Figure 2.10, for example, illustrates two conditions that the final interface values is equal to the upwind point value. Suresh and Huynh (1997) suggest to solve this problem by enlarging the constraining intervals and introducing a new monotonicity condition. Figures 2.11.a and 2.11.b illustrate the interval $I\left[S_i, S_{i+1}\right]$ and $I\left[S_i, S^{\mathrm{UL}}\right]$ being enlarged to $I\left[S_i, S_{i+1}, S^{\mathrm{MD}}\right]$ and $I\left[S_i, S^{\mathrm{UL}}, S^{LC}\right]$, respectively. In the first enlarged monotonicity interval, S^{MD} is the median of three values S^{AV}, the average of the two adjacent point values, S^{FL} and S^{FR}, the linearly extrapolated values from the left and right point values at interface, respectively. In the second enlarged monotonicity interval,

$$S^{\mathrm{LC}} = S_i + \frac{1}{2}\left(S_i - S_{i-1}\right) + \frac{4}{3} d^{\mathrm{MM}}_{i-1/2}, \tag{2.32}$$

is computed at interface as a point on a parabola determined by S_i, S_{i-1} and $d = 4d^{\mathrm{MM}}_{i-1/2}$ where $d^{\mathrm{MM}}_{i+1/2} = \mathrm{minmod}\left(d_i, d_{i+1}\right)$ and $d_i = S_{i-1} + S_{i+1} - 2S_i$. To fulfill the monotonicity preserving condition, the original interval value is fitted into the accuracy-monotonicity-preserving interval $S_{i+1/2} \in \left[S^{\min}, S^{\max}\right]$ by substituting the median of $S_{i+1/2}$, $S^{\min}$ and $S^{\max}$ for $S_{i+1/2}$.

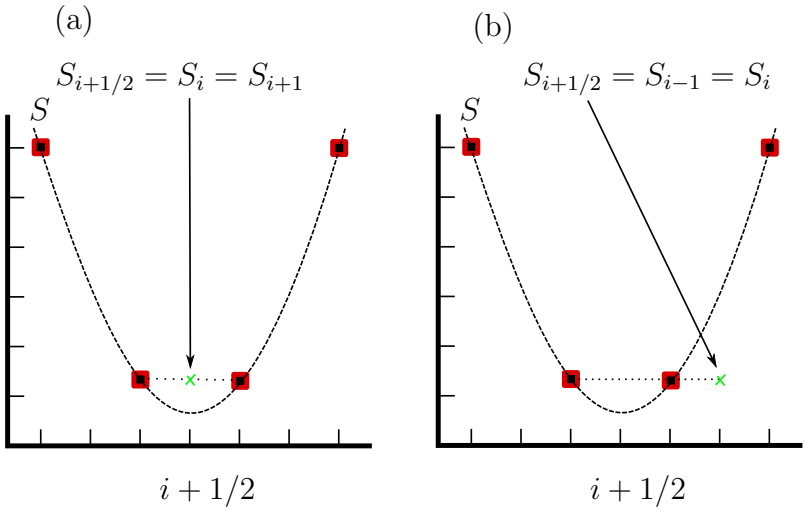

Figure 2.10: Two examples that $S^{\mathrm{MP}} = S_i$ and the scheme is degenerated to a first order upwind scheme. In case a) $S_i = S_{i+1}$ and in case b) $S_{i-1} = S_i$. This sketch is reproduced from Suresh and Huynh (1997).

$S^{\min}$,$S^{\max}$ is computed from the intersection of two enlarged intervals by

$$S^{\min} = \max\left[\min\left(S_i, S_{i+1}, S^{\mathrm{MD}}\right), \min\left(S_i, S^{\mathrm{UL}}, S^{\mathrm{LC}}\right)\right] \tag{2.33}$$

$$S^{\max} = \min\left[\max\left(S_i, S_{i+1}, S^{\mathrm{MD}}\right), \max\left(S_i, S^{\mathrm{UL}}, S^{\mathrm{LC}}\right)\right] \tag{2.34}$$

2.7 Quadratic conservative properties

It is well known that the finite difference schemes for two-dimensional incompressible flow violate the physical quadratic conservation, e.g. the conservation of mean kinetic energy and enstrophy (e.g., Arakawa, 1966). The need of predicting the mean state of the flow accurately is the reason for developing other type of advection schemes which conserve the physical quadratic properties for two dimensional flow. Arakawa and Lamb (1977), for example, design the interaction between computational cells in a 2D horizontal stencil such that the schemes conserves the quadratic quantities for a long time simulation. However, these schemes do not control the generation of oscillations. It is conceivable that viscosity or friction should be added to the model to remove the unwanted effects. For a comprehensive review of this type of advection schemes readers are referred to the work of Ketefian and Jacobson (2009, 2011).

2.8 Modern advection schemes

The main idea behind all new advection schemes is to improve the accuracy in smooth regions, providing sharp nonoscillatory results near discontinuities and reducing the drawbacks of the

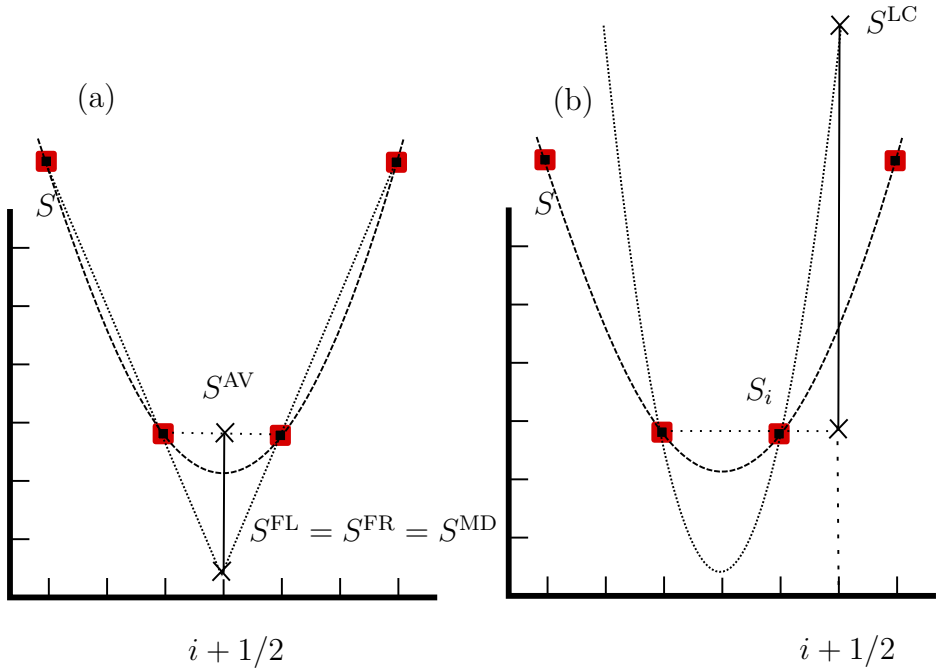

Figure 2.11: The existing monotonicity intervals are relaxed to new intervals to avoid loss of accuracy near an extremum. a) $S_{i+1/2} \in I\left[S_i, S_{i+1}\right] \longrightarrow S_{i+1/2} \in I\left[S_i, S_{i+1}, S^{\mathrm{MD}}\right]$, b) $S_{i+1/2} \in I\left[S_i, S^{\mathrm{UL}}\right] \longrightarrow S_{i+1/2} \in I\left[S_i, S^{\mathrm{UL}}, S^{\mathrm{LC}}\right]$. This sketch is reproduced from Suresh and Huynh (1997).

previous monotonicity constraints. Hybrid schemes, for instance, as an option for getting the best performance of two individual schemes are still popular. Fringer and Armfield (2005), for example, suggest a hybrid scheme which deploys a compressive universal limiter (e.g. Hyper-C) when the background potential energy (see section 3.3.6) is higher than its initial value and uses a diffusive TVD-scheme (e.g. Van Leer limiter) when the background potential energy is lower than its initial value. Another hybrid scheme was developed by Zahran (2009) using a cheap fourth order TVD scheme for smooth regions and an expensive seventh order WENO scheme near discontinuities. Čada and Torrilhon (2009) further generalise the idea of logarithmic reconstruction instead of polynomial reconstruction. The attempts of improving the performance of advection schemes is not limited to combining schemes. Hólm (1995); McCorquodale and Colella (2011), for example, suggest two dimensional and three dimensional stencils for computing the fluxes.

2.9 Conclusions

In this chapter the most well known effective advection schemes were reviewed. The purpose of this chapter was to categorise the advection schemes based on their unwanted numerical effects using the results of a 1D advection transport problem. In general, the higher order

advection schemes can be divided into three groups. The first group are the higher order advection schemes without any mechanisms to control the numerical oscillations, e.g. the third order upwind scheme. This group might be appropriate for the momentum advection schemes. The second group does not generate numerical oscillation but still suffer from squaring and smearing effects, e.g. FLM, FCT. The last group presents the least amount of the mentioned numerical problems with higher accuracy than the other advection schemes, e.g. the WENO and MP5 schemes. Therefore, it is interesting to see their performance in geophysical applications. However, these methods deploy highly complex expensive algorithms. Thus, they need to show improvement to the level of truth to the results of 3D geophysical models to be nominated for simulations. A third order upwind scheme from the first group, some FLM advection schemes from the second group and both WENO and MP5 schemes are selected to be tested in geophysical application in the form of several idealised test cases in chapters 4 and 5.

3 Governing equations, numerical ocean model and methodology

In order to show the importance of advective transport in oceanic flows and to elucidate the connection between the physical processes investigated in this research and the discretisation errors of the advection schemes, the governing equations of the used ocean model are reviewed in the first part. The used fundamental physical concepts in designing methodology and test cases are explained. Then, in the second part, the details of the deployed ocean model are reviewed. Finally, in the last part, the methodology for quantifying numerical errors in ocean models and their impacts on the model results are presented.

3.1 Governing equations and approximations[1]

In this section, the equations of motion and the associated approximations appropriate for large-scale oceanic flows are briefly introduced. Since the numerical ocean model and the corresponding diagnostic tools used in this study are developed based on the mode splitting method[2], the necessary 1D governing equations are also presented.

3.1.1 Conservation and transport equations

For an arbitrary fixed element in space with volume V which is bounded by surface A (see figure 3.1), the conservation law

$$\frac{\partial}{\partial t}\int_V \rho S \mathrm{d}V = -\oint_A \boldsymbol{F}.\mathrm{d}\boldsymbol{A} + \int_V S_{\mathrm{src}}\mathrm{d}V, \tag{3.1}$$

where ρ is the density of water demonstrates that the concentration[3] $S(\mathbf{x},\mathbf{t})$ is changed in time due to the net fluxes $\boldsymbol{F}$ including advective $\boldsymbol{F}(\mathbf{x},\mathbf{t})^{\mathsf{adv.}}$ and nonadvetive $\boldsymbol{F}(\mathbf{x},\mathbf{t})^{\mathsf{nonadv.}}$

[1] The governing equations and the approximations are explained in this section mainly following Olbers et al. (2012).

[2] The splitting methode decomposes the ordinary differential equations into separate integrable algorithms (see e.g. Banas et al., 2007)

[3] in unit per mass.

fluxes through the boundaries, interior sinks and sources $S_{src}(\mathbf{x}, \mathbf{t})$. The surface integration

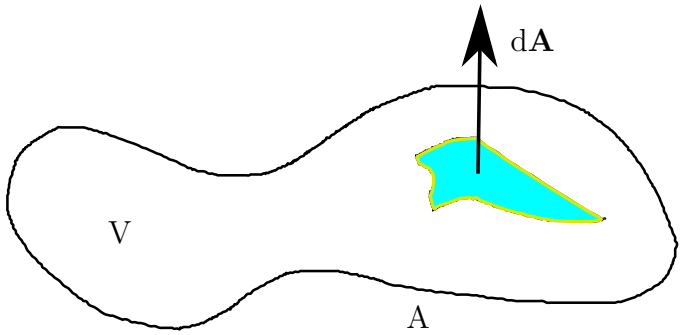

Figure 3.1: The sketch shows a very small arbitrary volume V enclosed by surface A. The property is fluxed through a surface element $d\mathbf{A}$ in the direction of the normal vector.

in equation (3.1) is replaced by a volume integral

$$-\int_V \nabla.\boldsymbol{F}\ \mathrm{d}V, \tag{3.2}$$

using Guass's theorem[4]. Since the volume and surfaces are fixed in an inertial frame[5], (3.1) can be rewritten as

$$\int_V \left[\frac{\partial(\rho S)}{\partial t} + \nabla.\boldsymbol{F} - S_{\mathrm{src}}\right] \mathrm{d}V = 0, \tag{3.5}$$

The value of bracket in (3.5) needs to be zero, since the size and the shape of the volume are arbitrary. This yields the general conservation equation for S:

$$\frac{\partial}{\partial t}(\rho S) + \nabla.\boldsymbol{F} - S_{\mathrm{src}} = 0. \tag{3.6}$$

[4]The Gaussian integral theorem, for the finite volume V

$$\int_V \nabla\ .\ \boldsymbol{u}\mathrm{d}V = \oint_A \boldsymbol{u}\ .\mathrm{d}A \tag{3.3}$$

[5]

$$\frac{d}{dt}\int_V \rho S \mathrm{d}V = \int_V \frac{\partial}{\partial t}(\rho S)\,\mathrm{d}V \tag{3.4}$$

1D transport equation

If the sink and source term in (3.5) are neglected, the 1D transport equation of concentration S, may be written as

$$\frac{\partial S}{\partial t} + \frac{\partial \left(\boldsymbol{F}_x\right)}{\partial x} = 0, \tag{3.7}$$

where the one dimensional flux $\boldsymbol{F}_x$ consists of advective $\boldsymbol{F}_x{}^{\mathrm{adv}} = uS$ and diffusive $\boldsymbol{F}_x{}^{\mathrm{diff}} = -k\frac{\partial S}{\partial x}$ fluxes:

$$\boldsymbol{F}_x = \boldsymbol{F}_x{}^{\mathrm{adv}} + \boldsymbol{F}_x{}^{\mathrm{diff}}, \tag{3.8}$$

where k is diffusivity.

3.1.2 Mass conservation

In fluid dynamics, because of the flux of fluid from boundaries, and the variation of the fluid density due to temperature and dissolved materials e.g. salt, an explicit equation of mass conservation

$$\frac{\partial \rho}{\partial t} + \nabla.\left(\rho \boldsymbol{u}\right) = 0, \tag{3.9}$$

is needed to close the equations of motion of the fluid (Vallis, 2006). This equation can be obtained by using $S = 1$, $\boldsymbol{F}^{\mathsf{nonadv}} = 0$, $\boldsymbol{F}^{\mathsf{adv}} = \rho \boldsymbol{u} S$ and $S_{src} = 0$ in (3.6) (Olbers et al., 2012) where $\boldsymbol{u} = (u, v, w) = u_i$ is the velocity vector.

3.1.3 Conservation of momentum

According to the Newton's second law

$$\rho \frac{\mathsf{D}\boldsymbol{u}}{\mathsf{D}t} = \boldsymbol{f}_{rc}, \tag{3.10}$$

the force per unit volume $\boldsymbol{f}_{rc}$ applied on the infinitesimal fluid element is balance with the mass and the acceleration of the infinitesimal fluid. Since $\boldsymbol{f}_{rc}$ is a combination of the gravity force $\rho \boldsymbol{g}$, and the surface force per unit volume $\frac{\partial \boldsymbol{\tau}}{\partial \boldsymbol{x}}$, an equation for the motion of the fluid, the Cauchy's equation, is obtained as follows (Kundu and Cohen, 2008):

$$\rho \frac{D\boldsymbol{u}}{Dt} = \rho \boldsymbol{g} + \frac{\partial \boldsymbol{\tau}}{\partial \boldsymbol{x}}, \tag{3.11}$$

where $\boldsymbol{\tau}$ is a stress tensor. For the fixed volume V, adding $\boldsymbol{u}$ times (3.9) to the left side of (3.11)

$$\frac{D\left(\rho \boldsymbol{u}\right)}{Dt} = \rho \boldsymbol{g} + \frac{\partial \boldsymbol{\tau}}{\partial \boldsymbol{x}}, \tag{3.12}$$

is obtained (Kundu and Cohen, 2008). The volume integral of (3.12) gives a conservation law of momentum

$$\frac{d\boldsymbol{M}^{\text{in}}}{dt} + \boldsymbol{M}^{\text{out}} = \boldsymbol{F}_{rc} \tag{3.13}$$

where $\boldsymbol{F}_{rc}$, $\boldsymbol{M}^{\text{in}} \equiv \int_V \rho \boldsymbol{u}\ \mathrm{d}V$ and $\boldsymbol{M}^{\text{out}} \equiv \int_{\mathrm{A}} \rho \boldsymbol{u}\boldsymbol{u}\mathrm{d}A$, are the applied force, the internal momentum and the net rate of outflux momentum, respectively. Conservation of the momentum states that the total force on the volume is equal to the net rate of changes in the momentum within the volume and the total flux of momentum through the surfaces (e.g. Kundu and Cohen, 2008). If the stress tensor $\boldsymbol{\tau}$ for a moving fluid is decomposed into isotropic[6] and viscous[7] tensors and in addition the shear of the molecular stresses is incorporated into (3.12) by relating the viscous tensor of the water as a Newtonian fluid to strain tensor as [8]

$$\frac{\partial \Sigma_{ij}}{\partial x_j} = \nu \left(\frac{\partial^2 u_i}{\partial x_j^2} + \frac{1}{3} \frac{\partial^2 u_j}{\partial x_i \partial x_j} \right) \tag{3.14}$$

and formulating the surface and volume forces as a combination of the Coriolis $-2\rho\boldsymbol{\Omega} \times \mathbf{v}$, the centrifugal and geopotential forces, the Navier-Stokes equation for rotating frame is obtained as follows:

$$\rho \frac{\mathrm{D}\boldsymbol{u}}{\mathrm{D}t} = -2\rho\boldsymbol{\Omega} \times \boldsymbol{u} - \nabla p + \nabla.\Sigma - \rho\nabla\Phi \tag{3.15}$$

where ν, $\boldsymbol{\Omega}$ and $\Phi(z) \approx \boldsymbol{g}z$ are the viscosity, angular velocity of the earth and gravity potential of the Earth, respectively. Note that the gravity potential of the Earth includes the effects of the centrifugal force (Olbers et al., 2012).

3.1.4 Viscosity and time averaging

Viscosity is a property of the fluid that causes resistant forces, i.e. viscous forces, against the shear flows due to the internal motion of the molecules. The viscous forces are proportional to the intensity of the shear and the kinematic viscosity ν (e.g. Vallis, 2006). The tangential

[6]The normal components of stress on a surface when fluid is at rest.
[7]The additional components of tensor due to viscosity.
[8](3.14) is defined using the Einstein notation, i,j=(1,2,3)

molecular viscous stress per unit mass[9], for example, is formulated approximately as $\Sigma_{yx} = \nu \frac{\partial u}{\partial y}$ for a shear flow $u(y)$ which is in the xy plan and the x direction (Olbers et al., 2012). In addition to the molecular viscosity, the concept of eddy viscosity has been introduced to parameterised the interaction of the small scale and large scale flows. Although the equations of motion are valid for a large range of scales from micro millimeter to synoptic scales, the turbulent flows are random and it may be impossible to virtually predict the details of motion of eddies. Therefore, studying the evolution of the statistical properties of the quantities such as time averages which are less affected by the unpredictability property of turbulence are more practical (Vallis, 2006). Thus, the oceanic flows in this work are studied for large scales and the small scale flows are filtered using Reynolds averaging method which decomposes each quantity, e.g. velocity into fluctuating $\boldsymbol{u}'$ and mean values $\widehat{\boldsymbol{u}}$ defined per volume as follows:

$$\boldsymbol{u} = \widehat{\boldsymbol{u}} + \boldsymbol{u}' \tag{3.16}$$

where $\widehat{(\ldots)}$ denotes averaging over a finite period of time or some form of ensemble mean (Vallis, 2006). The idea is to substitute (3.16) into (3.15) to obtain an equation for the mean quantity. However, due to the nonlinearity of the equations some new terms including the correlation between the perturbations, i.e. Reynolds stress terms, are appeared which represent the effects of the unresolved small scale flows on the mean flow (e.g. Vallis, 2006; Olbers et al., 2012). According to the classical theory of cascading energy, such interaction is downscaling and the turbulent fluxes are parameterised in terms of the mean state[10]. In analogy with the kinematic viscosity, the eddy viscosity is introduced to parameterise the turbulent momentum flux

$$\Sigma^{turb.} = -\bar{\rho}\widehat{\boldsymbol{u}'\boldsymbol{u}'} \tag{3.17}$$

For example, the vertical turbulent fluxes of momentum in x direction can be parameterised using the standard closure as follows[11]:

$$\Sigma_{xz}^{\mathsf{turb.}} = -\nu_t \frac{\partial u}{\partial z}, \tag{3.18}$$

where ν_t is eddy viscosity. Many parameterisations are suggested to estimate ν_t, as a function of time and space (see e.g., Olbers et al., 2012; Baumert et al., 2005). In contrast to the

[9] The viscosity force per unit volume is defined as $\mu\nabla^2\boldsymbol{v}$.

[10] The down-gradient parameterisation sometimes fails, for example, the interaction of horizontal mesoscale eddy momentum with the mean momentum gradient is often upgradient (Olbers et al., 2012) which is in contrast to the classical downscaling theory of cascading energy.

[11] The vertical turbulent fluxes are parameterised in the used ocean model using second-moment closure schemes, a feature which is however not applied in the present models studies based on frictionless dynamics.

kinematic viscosity, the eddy viscosity is a property of the flow. The magnitude of molecular viscosity is much smaller than eddy viscosity and is usually ignored in large scale flows[12]. Using down-gradient parameterisation, the continuity equation and the momentum balance may be rewritten as below:

$$\frac{\partial \rho}{\partial t} + \nabla . (\rho \boldsymbol{u}) = 0 \tag{3.19}$$

and

$$\rho \frac{\mathrm{D}\boldsymbol{u}}{\mathrm{D}t} = -2\rho \boldsymbol{\Omega} \times \boldsymbol{u} - \nabla p - \rho \nabla \Phi + \boldsymbol{M} \tag{3.20}$$

where $\boldsymbol{u}$ is the Reynolds average velocity field and

$$\boldsymbol{M} = \nabla . \left(\Sigma^{\mathsf{turb.}} + \Sigma \right) \tag{3.21}$$

is the sum of the flux divergency of the turbulent and the mean molecular fluxes.

3.1.5 Approximations for large-scale motions

There are several reasons that make using the Navier-Stokes equations infeasible in ocean modeling such as the speed of the high frequency waves that limits the time step and solving all terms of the vertical momentum that does not effectively increase the predictability of the oceanic scale flows but increases the simulation cost. Using approximation in ocean modelling is quite acceptable in some extent. This section reviews some of the important approximations to large scale oceanic flows due to smallness of oceanic density variation, the geometry of the Earth and the scales of oceanic flows.

Boussinesq approximation

For the approximations involving density, following the approach presented by (Olbers et al., 2012), all fields are decomposed into a reference value and a variable quantity, i.e.

$$p = p_r(z) + \tilde{p} \quad , \quad \rho = \rho_r(z) + \tilde{\rho} \quad , \quad S_l = S_{lr} + \widetilde{S}_l \quad , \quad \theta = \theta_r + \tilde{\theta} \tag{3.22}$$

[12] The kinematic viscosity of pure water at 10°C is $1.3 \times 10^{-6} \mathrm{m^2 s^{-1}}$. Two typical vertical eddy viscosity magnitudes are $0.1 \mathrm{m^2 s^{-1}}$ and $1.0 \times 10^{-4} \mathrm{m^2 s^{-1}}$ in the mixed layer and interior, respectively. The constant horizontal eddy viscosity for a southern ocean test case and the resolution of $2^o \times 1^o \mathrm{m^2 s^{-1}}$ is assigned as $4 \times 10^4 \mathrm{m^2 s^{-1}}$ (Olbers et al., 2012). For example, Mahadevan et al. (1996) states that molecular viscous force is neglected since the ratio of the molecular viscous force to the inertial force is about 10^{-3}.

where S_l, θ are salinity and potential temperature[13], respectively. The reference state is a fluid at rest with constant values for potential temperature and salinity. However, the reference pressure $p_r(z)$ and the reference density $\rho_r(z)$ are both depth dependent. Since any state of the rest is hydrostatically balanced[14], the pressure gradient force and gravity force in (3.20) are only dynamically relevant parts of the pressure.

$$-\nabla p - \rho\nabla\Phi \equiv -\nabla\tilde{p} - \tilde{\rho}\nabla\Phi, \tag{3.23}$$

In addition, the dynamically relevant part of the density

$$\tilde{\rho} = \rho\left(S_{lr} + \tilde{S}_l, \theta_r + \tilde{\theta}, p_r + \tilde{p}\right) - \rho\left(S_{lr}, \theta_r, p_r\right), \tag{3.24}$$

is much smaller than the reference density[15]. It is also shown that the dynamic variation of density is very small. Therefore, $\tilde{\rho}$ is neglected when it is compared to reference density. This approximation leads to an approximation which is appropriate for numerical large-scale atmospheric models, since the variations of reference density are small in the ocean (Olbers et al., 2012). Therefore, the errors of the variations of reference density in depth is ignored and ρ_r is substitute for a constant density ρ_0. The similar approximation to the reference pressure shows that the reference pressure variations is linear with depth, i.e. $\partial p_r(z)/\partial z \approx \partial p_0(z)/\partial z = -g\rho_0$ (see e.g., Olbers et al., 2012). In addition, the approximation in the magnitude of density variations[16]

$$\Delta\tilde{\rho} = C_{S_l}\Delta\tilde{S}_l - C_\theta\Delta\tilde{\theta} + C_p\Delta\tilde{p}, \tag{3.25}$$

shows that the contribution of variations of pressure in computing the variations of density is ignorable. Thus, (3.19) and (3.20) are approximated as follows

$$\nabla.\boldsymbol{u} = 0, \tag{3.26}$$

$$\rho_0\frac{\mathrm{D}\boldsymbol{u}}{\mathrm{D}t} = -2\rho_0\boldsymbol{\Omega}\times\boldsymbol{u} - \nabla\tilde{p} - \tilde{\rho}\nabla\Phi + \boldsymbol{M}. \tag{3.27}$$

Note that (3.26) corresponds to a fluid with constant density. Therefore, the variation of density is given by

$$\tilde{\rho} = \boldsymbol{F}\left(S_{lr} + \tilde{S}_l, \theta_r + \tilde{\theta}, p_0(z)\right) - \boldsymbol{F}\left(S_{lr}, \theta_r, p_0(z)\right), \tag{3.28}$$

[13] $\widetilde{(\ldots)}$ and $(\ldots)_r$ denote here the variable and the reference values, respectively.
[14] see (3.31).
[15] The equation of state: $\rho = \rho(S_l, \theta, p)$
[16] C_{S_l}, C_θ, C_p are the coefficients of the equation of state.

The equations in Boussinesq approximation include the equations (3.26), (3.27), (3.28) and two equations for potential temperature and salinity

$$\rho_0 \frac{D}{Dt} \widetilde{S}_l = N_s, \tag{3.29}$$

$$\rho_0 \frac{D}{Dt} \widetilde{\theta} = N_\theta, \tag{3.30}$$

where N_s and N_θ are parameterisations for the potential temperature and salinity equations, respectively.

Geometrical and scale approximation

The equations of motion are more simplified by choosing a coordinate system that the gravity acceleration has nonzero component only in the vertical direction. In addition, it is important that the Earth's geometry can be expressed in the coordinate system effectively (Olbers et al., 2012). Therefore, the equations of motion are transformed to spherical coordinates[17]. Furthermore, the equations of Boussinesq are more simplified by taking into account the facts that the ocean is a thin-shell layer and the aspect ratio δ of the vertical scale, H to the horizontal scale of large scale motions, L, is very small. The scaling analysis, presented by Olbers et al. (2012), shows that in the vertical momentum budget, all inertial terms and the mechanical friction terms are by a factor of δ^2 smaller than the vertical pressure gradient. In addition, the contribution of the Coriolis force to the vertical momentum budget is by a factor of δ smaller than the vertical pressure gradient. Therefore, for most large scale oceanic flows the acceleration of the vertical component of the momentum equation, $\frac{\mathrm{D}w}{\mathrm{D}t}$, is ignorable in comparison to the gravitational term. Furthermore, the buoyancy term is balanced by the pressure gradient which is called hydrostatic balance. Applying these geometrical approximations to the Boussinesq momentum equations obtain the momentum primitive equations as follows:

$$\frac{\partial \tilde{p}}{\partial z} = -\tilde{\rho} g, \tag{3.31}$$

$$\rho_0 \left(\frac{\mathrm{D}u}{\mathrm{D}t} - \frac{uv}{r} \tan\varphi - fv \right) = -\frac{1}{r \cos\varphi} \frac{\partial \tilde{p}}{\partial \lambda} + M_u, \tag{3.32}$$

$$\rho_0 \left(\frac{\mathrm{D}v}{\mathrm{D}t} + \frac{u^2}{r} \tan\varphi + fu \right) = -\frac{1}{r} \frac{\partial \tilde{p}}{\partial \varphi} + M_v, \tag{3.33}$$

[17] Although it is argued that the oblate spherical coordinates are the most appropriate coordinate system for the oceanic flows, it is impractical since there are some nonconstant coefficients (Olbers et al., 2012).

where r, λ, φ and f are the mean radius of the Earth, eastward longitude, northward latitude and the vertical component of the rotation vector[18] $\boldsymbol{\Omega}$, respectively.

The f-plane approximations

The effects of the sphericity of the Earth on the flows with the scales much smaller than global scale can be neglected. Therefore, a Cartesian coordinate system,

$$(x, y) \approx (r\lambda \cos\varphi, r\,(\varphi - \varphi_0))\,, \tag{3.34}$$

is defined on a plane tangent to the surface of the Earth at a specific latitude, φ_0 where $\boldsymbol{u}_h = (u, v)$ is the horizontal velocity field on the tangent plane in the east-west and the north-south directions, respectively. Thus (3.33) and (3.32) may be simplified as[19]

$$\frac{\mathrm{D}\boldsymbol{u}_h}{\mathrm{D}t} + f_0 \times \boldsymbol{u}_h = -\frac{1}{\rho_0}\nabla_h \tilde{p} + \boldsymbol{M}, \tag{3.35}$$

where $\boldsymbol{k}$ is the normal vector of the tangential plane and $f_0 = 2\boldsymbol{\Omega}\sin\varphi_o\boldsymbol{k}$. Since the numerical test cases applied in this research are in a limited latitudinal extent, the latitudinal variation of the Coriolis parameter can be neglected. The obtained tangent plane is called f-plane (Vallis, 2006).

3.1.6 The three dimensional momentum equations of the ocean model

The ocean model used in this research (GETM, see section 3.2) which is similar to some other geophysical coastal sea and ocean dynamics models (e.g., Blumberg and Mellor, 1987) uses the flux form of (3.35) as follows[20]:

$$\frac{\partial u}{\partial t} + \frac{\partial uw}{\partial z} + \frac{\partial u^2}{\partial x} + \frac{\partial uv}{\partial y} + M_u - f_0 v - \int_z^\eta \frac{\partial b}{\partial x} dz = -g\frac{\partial \eta}{\partial x}, \tag{3.36}$$

$$\frac{\partial v}{\partial t} + \frac{\partial vw}{\partial z} + \frac{\partial v^2}{\partial y} + \frac{\partial vu}{\partial x} + M_v + f_0 u - \int_z^\eta \frac{\partial b}{\partial y} dz = -g\frac{\partial \eta}{\partial y}, \tag{3.37}$$

where w, the vertical velocity, can be calculated from continuity equation:

$$\partial_x u + \partial_y v + \partial_z w = 0. \tag{3.38}$$

[18] see Olbers et al. (2012) for the remaining equations and the definition of substantial derivative $\frac{D}{Dt}$ in the spherical coordinate system

[19] For the mesoscale dynamical regime, the vertical advection of horizontal momentum is small and is neglected (see section 12.2.6 of Olbers et al. (2012).

[20] The numerical test cases in this research are simulated solving the primitive equations in f-plane.

The pressure term p in (3.35) is eliminated by vertically integrating (3.35) from depth z to water surface using Leibniz's rule (Blumberg and Mellor, 1987). The pressure gradient in x-direction, for example, may be written as follows:

$$-\frac{1}{\rho_0}\frac{\partial p}{\partial x} = -g\frac{\partial \eta}{\partial x} - \frac{g}{\rho_0}\int_z^\eta \frac{\partial \rho}{\partial x}\mathrm{d}z = -g\frac{\partial \eta}{\partial x} + \int_z^\eta \frac{\partial b}{\partial x}\mathrm{d}z, \tag{3.39}$$

where η and z are the water elevation, depth of an arbitrary point, respectively. The flux divergence of the turbulent and the mean molecular fluxes in x direction on Cartesian coordinate system is parameterised using down-gradient parameterisation:

$$M_u = -\frac{\partial\left(\left(\nu_t+\nu\right)\partial_z u\right)}{\partial z} - \frac{\partial\left(2A_h^M\partial_x u\right)}{\partial x} + \frac{\partial\left(A_h^M\left(\partial_y u+\partial_x v\right)\right)}{\partial y}, \tag{3.40}$$

$$M_v = -\frac{\partial\left(\left(\nu_t+\nu\right)\partial_z v\right)}{\partial z} - \frac{\partial\left(2A_h^M\partial_y v\right)}{\partial y} + \frac{\partial\left(A_h^M\left(\partial_x v+\partial_y u\right)\right)}{\partial x}, \tag{3.41}$$

where ν, ν_t and A_h are molecular, vertical and horizontal eddy viscosity, respectively.

3.1.7 Dynamical aspects of oceanic flows

The relative importance of the advection terms (and the rotation term) in the horizontal momentum budget is measured by the Rossby number

$$Ro \equiv \frac{U_0}{\boldsymbol{\Omega} L_0} \tag{3.42}$$

which is a dimensionless number defined as the ratio of the magnitude of the relative acceleration to the Coriolis force (see e.g. Olbers et al., 2012) where U_0 and L_0 are defined as the typical velocity and length scales of the dynamical regimes. The Rossby number and the Richardson number

$$Ri \equiv \frac{N^2}{\left(\partial \boldsymbol{u}_h/\partial z\right)^2}, \tag{3.43}$$

defined as the ratio of the vertical buoyancy gradient N^2 to the squared of the vertical shear of horizontal velocity $\boldsymbol{u}_h$, are the most applied dimensionless numbers for classification of the dynamical regimes. For dynamical regimes with $R0 \ll 1$ and $Ri \gg 1$ a detailed classification are presented using the complete vorticity equation (Beltrami's equation; see Olbers et al., 2012 chapter 5). The geostrifically balanced motions are categorised into three groups of *quasi-geostrophic*, *planetary-geostrophic* and *planetary wave* dynamical regimes which are relevant for mesoscale flow, gyre-scale flow and the adjustment of the circulation to changes in the forcing, respectively. The large scale and the mesoscale flows contain the large portion of

the kinetic energy of the oceans which are mainly two dimensional flows in geostrophic[21] and hydrostatic balances. Their vertical velocity component w_0 is much smaller than the typical lateral velocity. Table 3.1 summarises the typical aspects of gyre scale and mesoscale flows.

	Mesoscale	Gyre-Scale
U_0 (m s^{-1})	0.2	0.05
W_0 (m s^{-1})	2×10^{-4}	3×10^{-5}
L_0 (m)	10^5	10^6
$\ell = L_0/r$	0.015	0.15
Ro	0.03	7×10^{-4}

Table 3.1: List of typical scales and nondimensional numbers associated with large scale flows (Olbers et al., 2012). r is the mean radious of the earth.

The relative importance of the advection terms in the horizontal momentum budget increases for the dynamical regimes with smaller horizontal wavelength. For example, the Coriolis force for the small scale flows ($0.1 \sim 100$ m) are almost unimportant. The flows in this dynamical range are more three dimensional which contributes to mixing and dissipation in the ocean. For the dynamical regime between the small-scale and mesoscale regimes, i.e. submesoscale regime ($L_0 \sim 1$ km), the relative acceleration and the Coriolis force of the horizontal momentum balance are approximately in the same order. This dynamical regime is developed in local regions with $Ro \sim 1$ and $Ri \sim 1$, e.g. the eddying regime trapped in the mixed layers[22]. The submesoscale dynamics in the mixed layer similar to the mesoscale regime contribute to restratification and buoyancy transport, but in a smaller domain and with a shorter time scale. In fact, submesoscale is a bridge between the physical processes forced from the state of atmosphere, e.g. vertical mixing in the mixed layer and the adiabatic processes in the interior, e.g. internal waves (see e.g., Boccaletti et al., 2007; Thomas et al., 2008; Fox-Kemper et al., 2008). The interaction of the mesoscale, submesoscale and small-scale dynamical regimes are studied in the terms of transfer of energy between the scales. The main question is if the route of energy to dissipation is cascading from the large scale flows to the small scale flows (see e.g., Skyllingstad and Samelson, 2012). In the baroclinic instability test case of this research two series of simulations are performed resembling the physical properties of the mesoscale and submesoscale dynamical regimes. Table 3.2 compares different dynamical aspects of these two configurations.

[21] When the inertial term in the horizontal momentum balance is much smaller than the Coriolis force, the horizontal pressure term is in balance with the Coriolis force. This condition, geostrophic balance, is another fundamental balance.

[22] The mixed layers are not the only regions for developing submesoscale flows. They can be also recognised, for example, in the ocean interior and abyss (Thomas et al., 2008).

Dynamical regime	L_0 (km)	U_0 (m s^{-1})	Ro	δ	Ri
Mesoscale	40	0.2	0.1	4×10^{-2}	100
Submesoscale	5	0.2	0.8	4×10^{-2}	1.562

Table 3.2: List of the nondimensional numbers, the typical wavelength and the velocity magnitude used to design the baroclinc instability simulations in chapter 4 resembling the mesoscale and submesoscale dynamical regimes.

3.1.8 Available Potential Energy (APE)

Analysing the evolution of potential energy in two separate portions of Available Potential Energy (APE) and Background Potential Energy (BPE) provides insight into the physical processes of density-stratified flows such as mixing, turbulence and conversion of energy. The concept of APE is introduced to quantify the minimum attainable potential energy which can be extracted from potential energy by adiabatic processes[23](e.g. Olbers et al., 2012). Explicitly partitioning the variations of potential energy due to diabatic mixing and adiabatic processes is useful to quantify the energetics of mixing (see the BPE and APE analyses in chapter 5). BPE as a portion of potential energy which is changed only due to irreversible, diabatic processes, is defined as the minimum potential energy of a system[24] after an adiabatic rearrangement of the density field (e.g. Olbers et al., 2012). APE is defined as the difference between the total potential energy of the system and the background potential energy (see sections 3.3.6 and 3.3.7 for the computational methods). It can be inferred that the rearrangement of the density of the fluid parcels due to adiabatic processes leads to exchange of energy between kinetic and available potential forms.

3.1.9 Variance and rate of variance decay[25]

Although the mean value of the oceanic quantities

$$\overline{S} = \frac{1}{V} \int S \mathrm{d}V, \tag{3.44}$$

such as mean surface temperature and salinity provides useful information, it is necessary to measure the variance of the quantities

$$\sigma_s^2 = \overline{\left(S - \bar{S}\right)^2}, \tag{3.45}$$

[23] "Adiabatic describe a process in which there is no heat or molecular mass transfer (Winters et al., 1995)."
[24] This research is limited to the closed systems.
[25] This section follows the approach explained by Klingbeil et al. (2014)

to interpret the distribution of the quantities around their mean values. In fact, the variance is the mean squared deviation of the quantities from their mean value. The zero variance of the scalar quantities, e.g. buoyancy, can be inferred as a mixed fluid e.g., the fluid in the mixed layers. The variance of the vector quantities, e.g. velocity, presents either a fluid in rest or a uniform one-dimensional flow. In this section variance decay is motivated as mixing and dissipation rate.

The transport equation (3.7) describes the temporal variation of the spatial distribution of a quantity due to advective and diffusive fluxes. The diffusion term in the transport equation leads to mixing. By multiplication of (3.7) with $2S$ and also considering the incompressibility condition, a new prognostic equation for the variance of the concentration is derived (Burchard and Rennau, 2008; Klingbeil et al., 2014):

$$\frac{\partial S^2}{\partial t} + \frac{\partial}{\partial_x}\left\{uS^2 - k\frac{\partial S^2}{\partial x}\right\} = -2k\left(\frac{\partial S}{\partial x}\right)^2. \tag{3.46}$$

If the diffusivity of the field is ignored, the fluid is only stirred and there is no mixing:

$$\frac{\partial S^2}{\partial t} + \frac{\partial\left(uS^2\right)}{\partial_x} = 0 \tag{3.47}$$

However, the advective and diffusive fluxes of equation (3.46) are eliminated by volume averaging and the only decaying term is the sink term:

$$\overline{\frac{\partial\left(S\right)^2}{\partial t}} = \overline{-2k\left(\frac{\partial S}{\partial x}\right)^2}. \tag{3.48}$$

On the other hand, mixing can be measured by the rate of scalar variance decay $-\frac{\partial}{\partial t}\left\{\sigma_s^2\left(t\right)\right\}$ as the basic characteristic of mixing. With some simple algebraic manipulation the expression for the variance can be expanded:

$$\sigma_s^2\left(t\right) = \overline{\left(S-\overline{S}\right)^2} = \overline{S^2} - 2\overline{S}\ \overline{S} + \overline{S}^2 = \overline{S^2} - \overline{S}^2, \tag{3.49}$$

Since in a closed or in a periodic domain the mean value does not change ($\partial_t\overline{S} = 0$), the global Analytical Variance Decay (AVD) rate $-\frac{\partial}{\partial t}\left\{\sigma_s^2\left(t\right)\right\}$ can be written as below (Klingbeil et al., 2014):

$$-\frac{\partial}{\partial t}\left\{\sigma_s^2\left(t\right)\right\} = -\frac{\partial}{\partial t}\left\{\overline{S^2} - \overline{S}^2\right\} = -\frac{\partial}{\partial t}\overline{S^2}. \tag{3.50}$$

It is concluded that the rate of mean squared concentration decay presents the same concept. Based on (3.48) and (3.50) a connection between the rate of decay of average squared of concentration and diffusivity is achieved:

$$-\frac{\partial}{\partial t}\left\{\sigma_s^2\left(t\right)\right\} = \overline{-2k\left(\frac{\partial S}{\partial x}\right)^2}. \tag{3.51}$$

Thus, $-2k\left(\frac{\partial S}{\partial x}\right)^2$ is motivated to be the rate of local analytical variance decay rate, χ^{ana}, as a measure for local diffusion.

3.1.10 Instabilities mechanism

Although there are many steady state flows as solutions of the primitive equations e.g. pure zonal flows, they are not stable to small perturbations in the nature which leads finally to generation of eddies with various spatial scales. The transition of stable flow to turbulence is generally associated with initial instabilities (Bayly et al., 1988). In this process, the perturbations extract gradually energy from the mean flow and background potential energy. Then, growing waves are formed which evolve finally to certain wavelengths. In the last stage, the waves form eddies and turbulence flows are developed. Figures 5.7 and 5.8, for example, show the evolution of turbulent flow due to baroclinic instability. The largest eddies are generated mainly because of the barotropic[26] instabilities $(L_0 \sim 100\ \mathrm{km})$. The mesoscale $(L_0 \sim 10 - 100\mathrm{km})$ and submesoscale $(L_0 \sim 1\mathrm{km})$ eddies are mainly developed due to the slumping down of lateral buoyancy gradients which are associated with restratification. The instability processes are generally studied by investigating the growth or decay of the initial perturbations introduced to the flows. Since the theoretical analyses of instabilities generally linearise the instability problems by neglecting the quadratic terms in the perturbation variables, they are appropriate for comparison with the numerical solutions just in the initial stage of instabilities. This study focused only on lateral shear and baroclinic instabilities to make the interpretation of the effects of the advection schemes on the instability precess feasible. In this section, first, the baroclinic instability are explained using the Eady problem. Then, the turbulent phase of the flow are studied using the results of the baroclinic instability test case in chapter 5.

Baroclinic instability

"Baroclinic instability refers to a process by which perturbations draw energy from the mean flow potential energy" (Grotjahn, 2003). For the typical lateral oceanic stratification and

[26] A lateral shear instability affected by the latitudinal variation of the Coriolis parameter which may be observed in fluid with constant density.

vertical shear, the baroclinic instabilities can be classified in two groups of mesoscale and submesoscale flows. The first group is deep water mesoscale instabilities which are developed in the entire of the water column and the other type is ageostrophic shallow submesoscale instabilities which are generated faster and in a smaller scale than the earlier which are usually trapped in the mixed layer (Fox-Kemper et al., 2008). Although these instabilities might happen along each other in the ocean, the theoretical work studied their mechanisms separately. Eady (1949) derived an analytical solution mimicking main features of baroclinic instability for large Richardson numbers[27] and therefore quasi-geostrophic dynamics. The Eady model is suggested for a zonal, re-entrant, flat-bottom channel in the f-plane with a constant vertical and meridional buoyancy gradient. The initial velocity field includes a zonal background velocity which is in thermal wind balance (see section 5 for more details). However, for the Richardson number of order one, just approximate analytical solutions can be found (e.g., Stone, 1966). Thereby, the configurations in the baroclinic instability test case in chapter 5 are referred to be mesoscale if their background state is characterised by a small Rossby number. On the other hand, the simulations with the background state that are characterised by Rossby numbers of order one are introduced as submesoscale. These solutions are often used to estimate the growth rate[28] and the wave length of the fastest growing unstable wave. The maximum growth rate $\sigma_E \approx 0.3\frac{U_0}{L_0}$, Rossby deformation[29] radius $L_0 = \frac{NH}{f_0}$ and the scale of maximum instability $L_{\max} \approx 3.9\ L_0$ are approximated for the mesoscale configuration of the baroclinic test case in chapter 5 as 0.0054 day^{-1}, 40 km and 156 km, respectively. According to the Stone's approximation for $Ri < 1$, the scale of maximum instability $L_{\max} = 2\pi/ks$ where

$$ks = \sqrt{\frac{5/2}{1 + Ri}\frac{f_0}{U_0}} \tag{3.52}$$

is computed as 25.175 km.

[27] Brüggemann and Eden (2014) state based on a review of the work of Stone (1966) that Ri is a criteria to distinguish between the type of instabilities. Baroclinic instability can be generated for all range of Ri. However, the ageostrophic baroclinic instability occurred only for $Ri < 1$.

[28] The possibility of growing the solution is described by growth rate. If σ in the exponential part of solution has a non-zero imaginary component, the result is an oscillatory motion. However, if σ is a real number the amplitude of the perturbation will grow (Vallis, 2006).

[29] N^2 is vertical buoyancy gradient.

Perturbation Kinetic Energy Budget (PKE)

Following Skyllingstad and Samelson (2012), the time evolution of the domain average[30] perturbation kinetic energy

$$\text{PKE} =< u_i'^2 >=< \frac{1}{2}\left(u'^2 + v'^2\right) > \tag{3.53}$$

is calculated by domain averaging the results of the product of horizontal perturbation velocity u_i' with the horizontal momentum equations (3.36) and (3.37)

$$\begin{aligned}\frac{\partial \text{PKE}}{\partial \text{t}} = \underbrace{< u_i'.\frac{\partial u_i'}{\partial t} >}_{\text{storage}} = \underbrace{< -u_i'\left[\frac{\partial}{\partial_{x_j}}\left(u_i u_j\right) + \frac{\partial}{\partial z}\left(u_i w\right)\right] >}_{\text{shear production}} \\ + \underbrace{< u_i' \int_z^\eta \frac{\partial b}{\partial x_i}\text{dz} >}_{\text{buoyancy production}} \underbrace{- < g u_i' \frac{\partial}{\partial x_i}\eta >}_{\text{barotropic work}}\end{aligned} \tag{3.54}$$

where $\text{u}_\text{i}' = \text{u}_\text{i} - \overline{\text{u}_\text{i}}^z$, $\text{b} = -\text{g}\dfrac{\rho - \rho_\text{o}}{\rho_\text{o}}$, and η are a component of perturbation velocity, the buoyancy and the water surface elevation[31,32], respectively. The terms in equation (3.54) are referred to the rate of change of domain average of the PKE, shear production, buoyancy production and barotropic work, respectively. The dissipation term is neglected in (3.54). Figures 3.2.a and 3.2.b compare the time evolution of these terms for the submesoscale and mesoscale configurations in the baroclinic test case in section 5. For both configurations the production of PKE is dominated by the buoyancy production. The buoyancy production is always positive. The negative values of the shear production in both figures indicates that the perturbations amplify the background velocity. After approximately 35 and 150 days for the submesoscale and the mesoscale configurations, there are undulations in exchange of energy between mean kinetic energy and PKE. It shows that in the turbulent phase, the production of PKE is both dominated by buoyancy production and shear production.

[30] $< \ldots >$ denotes here domain average operator.
[31] $\overline{(\ldots)}^z$ denotes zonal average operator.
[32]

$$< u_i'.\frac{\partial u_i}{\partial t} >=< u_i'.\frac{\partial\left(u_i' + \overline{u_i}^z\right)}{\partial t} >=< u_i'.\frac{\partial u_i'}{\partial t} >, \qquad < u_i'.\frac{\partial\left(u_i'\right)}{\partial t} >\approx 0 \tag{3.55}$$

(a) Submesoscale configuration

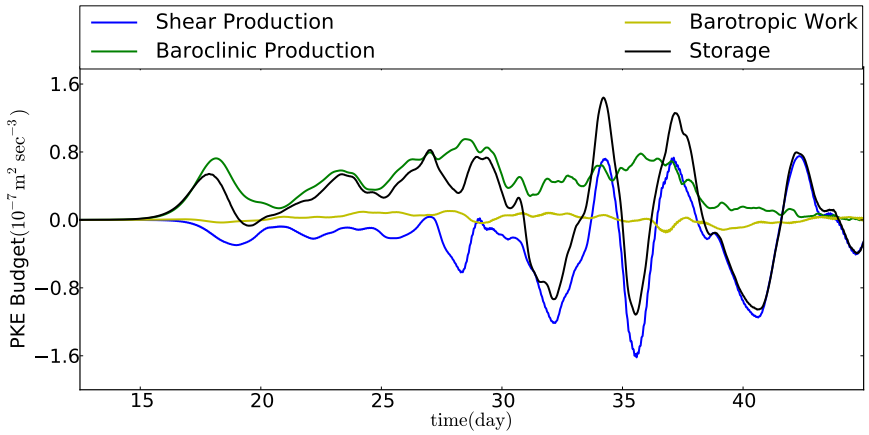

(b) Mesoscale configuration

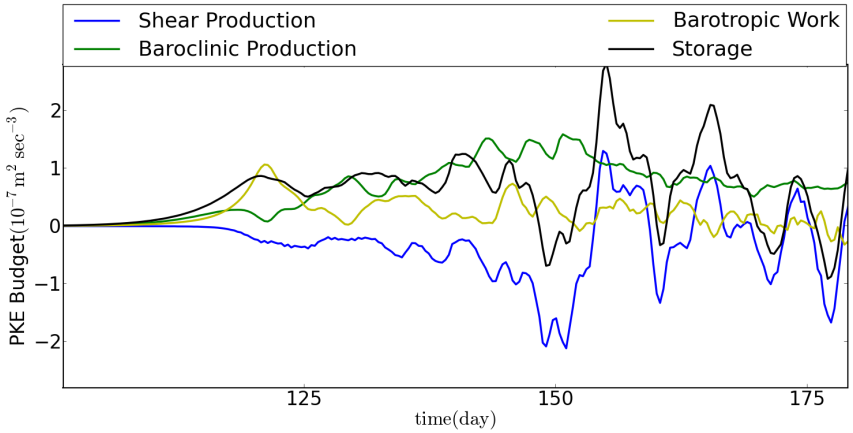

Figure 3.2: The perturbation kinetic energy budget of the baroclinic instability test case in chapter 5 for a) submesoscale configuration and b) mesoscale configuration.

3.2 Numerical ocean model

The General Estuarine Transport Model (GETM; for details see e.g., Hofmeister et al., 2010) is used in this study. GETM is a primitive-equation, finite-volume, structured-grid model on an Arakawa C-grid, with bottom- and surface-following general vertical coordinates and explicit mode-splitting into a vertically integrated barotropic mode and a vertically resolved baroclinic mode. For the simulations of this research a linear version of the equation of state is used. The model has mainly been applied for coastal (e.g. Banas et al., 2007), estuarine (e.g. Burchard et al., 2004, 2011), shelf sea (e.g. Van Leeuwen et al., 2013) and lake (e.g. Umlauf and Lemmin, 2005) applications.

3.3 Methodology

In this section, first the methods for diagnosing numerical errors are reviewed. The variation of kinetic energy and background potential energy due to numerical mixing and dissipation are introduced as the main index for categorising advection schemes. Then, the approaches to investigate the effects of numerical mixing and dissipation on dynamics of flow are discussed.

3.3.1 Discretised advection equation

The split method of numerical ocean circulation models, e.g. GETM divides the computational process into a sequence of steps (see e.g. Blanes et al., 2008). The advection terms are solved in all directions separately. Thus, their numerical mixing and dissipation are diagnosed separately (Burchard and Rennau, 2008; Burchard, 2012; Klingbeil et al., 2014). Then, the diagnostic method is generalised for 3D model. The one dimensional advective flux of an arbitrary quantity $Flx^{adv}_{\mathrm{i+1/2}} = U_{\mathrm{i+1/2}} S_{\mathrm{i+1/2}}$ in a discretised advection equation

$$\frac{V_i^{n+1} S_i^{n+1} - V_i^n S_i^n}{\Delta t} + Flx^{adv}_{i+1/2} - Flx^{adv}_{i-1/2} = 0, \tag{3.56}$$

is computed using an approximated interface value $S_{\mathrm{i+1/2}}$ deploying the advection schemes explained in chapter 2. V_i is the volume of the $i\mathrm{th}$ computational cell (see Figure 3.3).

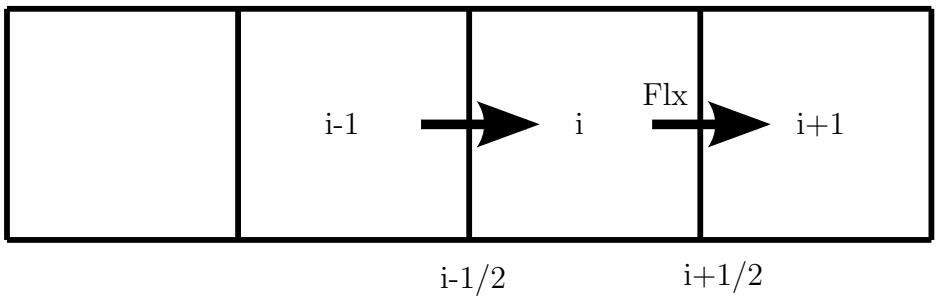

Figure 3.3: The sketch represents the schematic 1D computational discrete domain. The fluxes through boundaries are approximated using the interface value $S_{i+1/2}$.

3.3.2 Rate of discrete variance decay as a measure of numerical mixing and dissipation[33]

Klingbeil et al. (2014) generalised the earlier method of Burchard and Rennau (2008). In the new method the transport of the second order moment is approximated using equation (3.56).

$$\frac{V_i^{n+1}\left(S_i^2\right)^{n+1} - V_i^n\left(S_i^2\right)^n}{\Delta t} + Glx_{i+1/2}^{adv} - Glx_{i-1/2}^{adv} = 0, \tag{3.57}$$

Inspiring from the rate of analytical variance decay as a measure for mixing, the rate of discrete variance decay [34]

$$\begin{aligned} -\frac{\left(\Delta\sigma_s^2\right)^{n+1}}{\Delta t} &= -\frac{1}{\Delta t}\left\{\left[\left\langle S_i^2\right\rangle_v^{n+1} - \left(\left\langle S_i\right\rangle_v^{n+1}\right)^2\right] - \left[\left\langle S_i^2\right\rangle_v^{n} - \left(\left\langle S_i\right\rangle_v^{n}\right)^2\right]\right\} \\ &= -\frac{1}{\Delta t}\left\{\left[\left\langle S_i^2\right\rangle_v^{n+1} - \left\langle S_i^2\right\rangle_v^{n}\right]\right\}, \end{aligned} \tag{3.58}$$

in absence of physical mixing when the advection schemes is mass conservative, is considered as numerical mixing. However, it computes only the global decay rate and does not provide local information. Similar to (3.46), the sink term (or source term in case of negative value) on the right hand side of the equation of variance of the discrete variable

$$\frac{V_i^{n+1}\left(S_i^{n+1}\right)^2 - V_i^n\left(S_i^n\right)^2}{\Delta t} + Glx_{i+1/2}^{adv} - Glx_{i-1/2}^{adv} = -V_i^{n+1}\chi_i^{n+1}, \tag{3.59}$$

where explain the local discrete variance decay. Since $(S_i^n)^2 = (S_i^2)^n$, (3.59) is a diagnostic equation. This equation is derived by multiplication of $S_i^{n+1} + S_i^n$ by (3.56). The term of Glx in (3.59) is the advective flux of the squared quantity. As explained by Klingbeil et al. (2014), χ is needed to guarantee

$$\langle\chi\rangle^{n+1} \equiv -\frac{\left(\Delta\sigma_s^2\right)^{n+1}}{\Delta t}, \tag{3.60}$$

in a closed or periodic domain. It is shown that (Klingbeil et al., 2014), using (3.57) the local discrete variance decay in (3.59) is diagnosed as follows:

$$\chi_i^{n+1} = \frac{\left(S^2\right)^{n+1} - \left(S^{n+1}\right)^2}{\Delta t} \tag{3.61}$$

[33] This section is provided based on the approach explained by Klingbeil et al. (2014)

[34] The discrete (sample) mean value and discrete (sample) variance are defined as $\bar{S} = \frac{1}{M}\sum_{i=1}^{M} S_i$ and $\sigma^2 = \frac{1}{M}\sum_{i=1}^{M}\left(S_i - \bar{S}\right)^2$ for a population $\sum_{i=1}^{M}(S_i - \bar{S}) = 0$ with M number of scores (Thomson and Emery, 2001).

3.3.3 Numerical dissipation and kinetic energy loss

The conservation of discrete energy in numerical models is the focus of several studies, see e.g. Arakawa (1966), Marsaleix et al. (2008) and Klingbeil et al. (2014). They show that significant loss of (kinetic) energy is caused by discretisation errors associated with the numerical advection of discrete momentum. A 3D analysis method is developed by Klingbeil et al. (2014) to quantify this spurious (numerical) dissipation in each grid cell. Their analysis is based on the variance decay of the single velocity components and diagnoses a local numerical dissipation rate

$$\frac{1}{2}\chi_d\left(\mathbf{u}\right)_{i,j,k} = \frac{1}{\mathrm{d}V_{i,j,k}}\left(\chi_i + \chi_j + \chi_k\right), \tag{3.62}$$

where

$$\chi_i = \frac{1}{2}\left(\mathrm{d}V_{i-1/2,j,k}\left(\frac{1}{2}\chi^u_{i-1/2,j,k}\right) + \mathrm{d}V_{i+1/2,j,k}\left(\frac{1}{2}\chi^u_{i+1/2,j,k}\right)\right), \tag{3.63}$$

$$\chi_j = \frac{1}{2}\left(\mathrm{d}V_{i,j-1/2,k}\left(\frac{1}{2}\chi^v_{i,j-1/2,k}\right) + \mathrm{d}V_{i,j+1/2,k}\left(\frac{1}{2}\chi^v_{i,j+1/2,k}\right)\right), \tag{3.64}$$

$$\chi_k = \frac{1}{2}\left(\mathrm{d}V_{i,j,k+1/2}\left(\frac{1}{2}\chi^w_{i,j,k-1/2}\right) + \mathrm{d}V_{i,j,k+1/2}\left(\frac{1}{2}\chi^w_{i,j,k+1/2}\right)\right). \tag{3.65}$$

Based on the local numerical dissipation rate, in the present study the accumulated global numerically dissipated energy,

$$ND = \int\int \tfrac{1}{2}\chi_d\left(\mathbf{u}\right)\rho_0 \mathrm{d}V\mathrm{d}t, \tag{3.66}$$

is analysed.

3.3.4 2D horizontal mechanical energy budget and numerical viscosity

The purpose of this section is to first derive an equation for the mechanical energy budget from depth averaged equations according to Vreugdenhil and Wijbenga (1982). In the second step, the velocity variance method is applied to the mechanical energy equation to compute the local numerical viscosity. The depth averaged momentum equation and the equation for

the layer thickness read like follows:

$$\partial_t U + U\partial_x U + V\partial_y U - fV = -g\partial_x H + \frac{1}{H}\left(\partial_x\left(HT_{xx}\right) + \partial_y\left(HT_{xy}\right)\right) \tag{3.67a}$$

$$\partial_t V + U\partial_x V + V\partial_y V + fU = -g\partial_y H + \frac{1}{H}\left(\partial_x\left(HT_{xy}\right) + \partial_y\left(HT_{yy}\right)\right) \tag{3.67b}$$

$$\partial_t H + \partial_x\left(HU\right) + \partial_y\left(HV\right) = 0 \tag{3.67c}$$

where g, H, U and V are gravity acceleration, total water depth, zonal and meridional vertically averaged components of velocity, respectively. It is assumed that there is no bottom and surface stress and the bottom level is flat. The effective stresses are approximated by the turbulent stress terms and Boussinesq's eddy viscosity concept invoked to give $T_{xx} = 2\nu^{\mathrm{h}}\frac{\partial U}{\partial x}$, $T_{xy} = \nu^{\mathrm{h}}\left(\frac{\partial U}{\partial y} + \frac{\partial V}{\partial x}\right)$ and $T_{yy} = 2\nu^{\mathrm{h}}\frac{\partial V}{\partial y}$, where ν^{h} is the eddy viscosity coefficient (see e.g., Borthwick and Kaar (1993); Vreugdenhil and Wijbenga (1982)).

The equation for kinetic energy can be obtained by finding the scalar production of $(3.67\mathrm{a})$ and $(3.67\mathrm{b})$ and the transport vectors (UH and VH, respectively). Then, each resulting equation is combined with the continuity equation $(3.67\mathrm{c})$ which is multiplied by U^2 and V^2, respectively. Defining, $E = \frac{1}{2}H(U^2 + V^2)$, the kinetic energy budget can be written as:

$$\partial_t E + \partial_x\left(UE\right) + \partial_y\left(VE\right) + g\left(UH\partial_x H + VH\partial_y H\right) - \sum_{i,j=1}^{2}\partial_{x_j}\left(2U_i\nu^{\mathrm{h}}HS_{ij}\right) = -2\nu^{\mathrm{h}}HS_h^2 \tag{3.68}$$

where $S_{ij} = \frac{1}{2}\left(\partial_{x_j}U_i + \partial_{x_i}U_j\right)$ and $S_h^2 = \sum_{i,j=1}^{2} S_{ij}^2$ are used for horizontal shear. Finally following the approach of Burchard (2012), multiplication of equation $(3.67\mathrm{c})$ with gH and subsequent addition of the resulting equation to (3.68) and some mathematical rearrangement gives an equation for the mechanical energy budget $e = E + gH^2/2$:

$$\partial_t e + \partial_x\left(Ue\right) + \partial_y\left(Ve\right) + \frac{1}{2}g\left(\partial_x\left(UH^2\right) + \partial_y\left(VH^2\right)\right) - \sum_{i,j=1}^{2}\partial_{x_j}(2U_i\nu^{\mathrm{h}}HS_{ij}) = -2\nu^{\mathrm{h}}HS_h^2 = -D^{phys} \tag{3.69}$$

with the non-negative physically induced dissipation D^{phys}. Area integration of Eq. (3.69) results in:

$$\partial_t \int_0^{L_x}\int_0^{L_y} e\,\mathrm{d}x\mathrm{d}y = -\int_0^{L_x}\int_0^{L_y} D^{phys}\mathrm{d}x\mathrm{d}y \tag{3.70}$$

where L_x and L_y are zonal and meridional lengths of the domain which shows that global mechanical energy is conserved for $\nu^{\mathrm{h}} = 0$. For this inviscid case, numerical dissipation is the only mechanism changing the global mechanical energy. Computing numerical dissipation allows to approximate the numerical viscosity. Based on relation (3.69) between the physical dissipation and the physical viscosity, the effect of numerical dissipation can be estimated in terms of:

$$\nu^{\mathrm{h}}_{\mathrm{num}} = \frac{\frac{1}{2}\chi_d}{2HS_h^2} \tag{3.71}$$

In addition, the global effective numerical viscosity is computed by the assumption that the effective implicit eddy viscosity is constant for all grids. For the lateral shear instability experiment, the global numerical viscosity, $\nu^{\mathrm{h}}_{\mathrm{num,g}}$, associated with the depth-integrated momentum equations are computed by

$$\nu^{\mathrm{h}}_{\mathrm{num,g}} = \frac{\int \frac{1}{2}\chi_d \mathrm{d}V}{\int 2HS_h^2 \mathrm{d}V} \tag{3.72}$$

3.3.5 Global effective eddy viscosity

In addition to the global numerical viscosity, effective eddy viscosity provides comprehensive information. The effective eddy viscosity is computed here alternatively following the approach reviewed by Hólm (1996):

$$\nu_e = -\frac{1}{2E_\omega}\frac{dE}{dt} \tag{3.73}$$

with the volume average enstrophy, E_ω and the volume average kinetic energy E. In 2D viscous turbulent flow the vorticity and the momentum are redistributed by viscosity. Thus, the kinetic energy and enstrophy of an incompressible, 2D turbulent flow are dissipated. If the flow is assumed to be inviscid, the global effective viscosity should represent the global numerical viscosity. The results of global numerical viscosity introduced in the previous section and the effective eddy viscosity presented here will be compared in chapter 4 to show that the diagnosed numerical viscosity is plausible.

3.3.6 Background Potential Energy (BPE)

According to Winters et al. (1995), background potential energy,

$$BPE = g\int_V \rho z_*(x,t) dV, \tag{3.74}$$

is defined as the lowest level of potential energy of the system after an adiabatic rearrangement. In the above relation ρ and $z_*(\mathbf{x},\mathbf{t})$ denote the in situ density and the height of the fluid parcel from a reference at position $(\mathbf{x},\mathbf{t})$ after the rearrangement. Background potential energy is constant if there is no mixing of temperature and salinity. However, numerical diapycnal flux changes the background potential energy. Following the work of Winters et al. (1995) and Winters and D'Asaro (1996), Griffies et al. (2000) quantify the rate of numerical diapycnal mixing empirically diagnosing the effective diffusivity from

$$k_{eff}\left(z_*\left(\mathbf{x},\mathbf{t}\right)\right) = \frac{-F\left(z_*\left(\mathbf{x},\mathbf{t}\right)\right)}{\partial_{z_*(\mathbf{x},\mathbf{t})}\rho_{ref}\left(z_*\left(\mathbf{x},\mathbf{t}\right)\right)} \tag{3.75}$$

where $F\left(z_*\left(\mathbf{x},\mathbf{t}\right)\right)$, the averaged diapycnal flux, is computed as

$$F\left(z_*\left(\mathbf{x},\mathbf{t}\right)\right) = \frac{1}{A}\int dS\hat{\rho}.F_D. \tag{3.76}$$

In the relations (3.75) and (3.76), A, dS, $\hat{\rho}$, ρ_{ref} and F_D are horizontal cross-sectional area of the fluid domain, the differential area element for an isopycnal surface, a diapycnal unit vector, density of the stably stratified sorted fluid and the amount of flux crossing an isopycnal surface, respectively. For the comparison of the effects of advection schemes the vertically averaged effective diffusivity

$$k_{avg}^{num} = \frac{\int dz_*\left(\mathbf{x},\mathbf{t}\right)\left|k_{eff}(dz_*\left(\mathbf{x},\mathbf{t}\right))\right|}{\int dz_*\left(\mathbf{x},\mathbf{t}\right)} \tag{3.77}$$

is computed as a single number.

3.3.7 Eddy kinetic energy and available potential energy

Differences in the total eddy kinetic energy,

$$EKE = \frac{1}{2}\int \left(\left(u-\overline{u}\right)^2 + \left(v-\overline{v}\right)^2 + \left(w-\overline{w}\right)^2\right) dV \tag{3.78}$$

show the influence of advection schemes on the eddy field where $\overline{u}$, $\overline{v}$ and $\overline{w}$ are zonally averaged velocity components. In addition, available potential energy can quantify indirectly the stratification condition of the fluid. Available potential energy

$$APE = PE - BPE, \tag{3.79}$$

is computed as the difference between potential energy

$$PE = g \int_V \rho(z(\mathbf{x}, t)) z(\mathbf{x}, t) \, \mathrm{d}V, \tag{3.80}$$

and background potential energy.

3.4 Summary

The main goal of this chapter was to establish a framework for diagnosing and analysing the effects of advection schemes on development of flow. The most recent developed diagnostic methods in ocean models were reviewed and applied. These methods in general interpret the numerical errors as physical relevant quantities, e.g. numerical dissipation, background potential energy. In addition to the mentioned methods in the literature, diagnosing local and global numerical viscosity is a new diagnostic method which is suggested in this chapter. From other line of thought, global effective viscosity is also introduced as a method to verify the results of numerical eddy viscosity.

4 Idealised steady state flow

In this chapter, a system of steady state eddies (Honeycomb) is introduced for analysing the numerical effects of advection schemes. An approximate analytical solution to the water elevation is suggested. The dissipation of the kinetic energy in the model is numerical because of the following two reasons. First, it is assumed in this study that the flow is inviscid. Second, the numerical experiments reveal that the transfer of energy between the kinetic energy and the potential energy is ignorable. The advantages of conducting this numerical experiment over a simple 1D initial value problem, which was presented in chapter 2, are that firstly, the numerical schemes are analysed this time in a full ocean model and the advection terms of the momentum equations are solved; Second, since the Honeycomb experiment provides an opportunity to test the advection schemes for a simple oceanic flow, the level of numerical dissipation observed in the model is more realistic. In addition, the conclusions learned from this experiment help to better interpret the complex results of instabilities and 3D numerical experiments presented in chapter 5. The wave length of these eddies are designed in the same order of the mesoscale eddies obtained in the two dimensional phase of flow in the baroclinic instability experiment presented in chapter 5. In this chapter, several advection schemes are selected for analysis from all three groups of advection schemes presented in section 2.9. Then, the advection schemes used in this section are categorised again based on their dissipative behaviour, namely dissipative, antidissipative and neutral schemes.

4.1 Honeycomb

Taylor (1923) advances the earlier works in deriving analytical solutions for specific cases in which solution of equations of motion for two dimensional viscous flow might be obtained. The privilege of this solution is because of including the inertia term in the equations. Same and similar classes of solutions are applied by Arakawa and Lamb (1977), Bell et al. (1989) and Hólm (1996) to investigate the behaviour of specific advection schemes. These types of solutions are obtained under the rigid lid approximation, i.e. the approximation that the water surface is considered to be flat. Section 4.2 introduced an approximated analytical solution to the water elevation of a system of alternately rotating eddies (see (4.10)) with the assumption of an inviscid flow. The velocity field, equation (4.11), is computed by choosing the stream

function as $\psi = A\cos(ax)\cos(ay)$ where ψ, a, A are the streamfunction, wave number and a constant, respectively. Figure 4.1 shows the streamfunction and the resultant water elevation and the velocity field. Since the inviscid, stationary flow results from a balance between pressure gradient and centrifugal force (established by advection terms), variations of kinetic energy is mainly caused by numerical dissipation due to the discrete advection terms. Section 4.3 presents a sensitivity analysis to compare the advection schemes for different resolutions. The experiment is performed for double periodic boundary conditions. It is expected that the accurate advection schemes present the least accumulated global numerically dissipated.

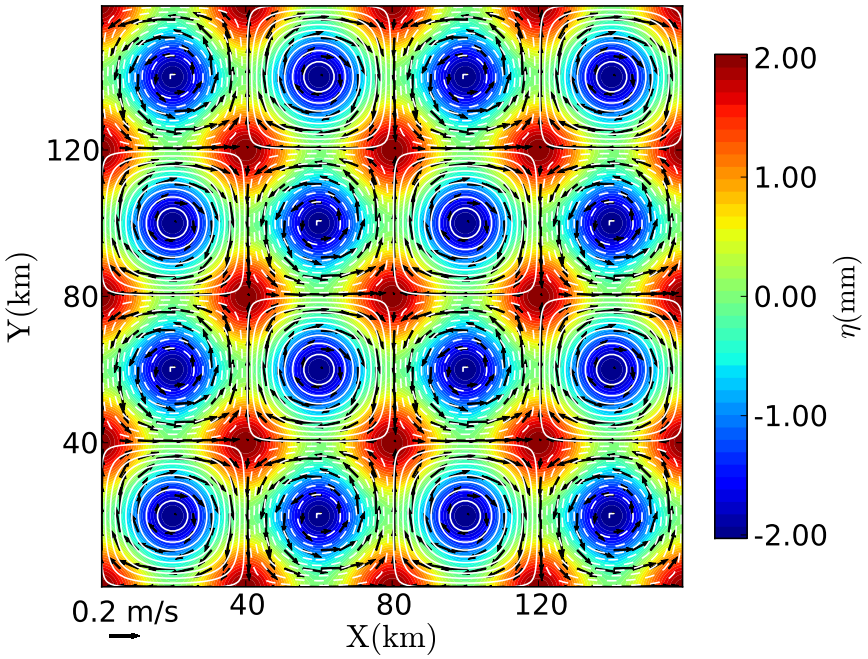

Figure 4.1: Initial velocity field (arrows) and water elevation (color code) for the Honeycomb test case using (4.11) and (4.10), respectively. The white contours (positive: full lines; negative: dashed lines) show the streamfunction.

4.2 Analytical approximation

It is shown by Taylor (1923) that a specific family of streamfunctions ($\psi = \psi_1 e^{\nu K t}$) is the solution of vorticity equation

$$\nabla^2 \psi = \zeta, \tag{4.1}$$

and stream function equation

$$\left(\frac{\partial}{\partial_t} - \frac{\partial\psi}{\partial_y}\frac{\partial}{\partial_x} + \frac{\partial\psi}{\partial_x}\frac{\partial}{\partial_y} - \nu\nabla^2\right)\nabla^2\psi = 0, \tag{4.2}$$

if $\nabla^2\psi = K\psi$ and $\partial\psi/\partial t - \nu K\psi = 0$. where ζ, ν and K indicate vorticity, kinematic viscosity and a constant, respectively.

In this section an approximate analytical solution of the water elevation (see (4.7) and (4.10)) of inviscid, steady state, depth averaged (Vreugdenhil and Wijbenga, 1982) equations,

$$U\frac{\partial U}{\partial_x} + V\frac{\partial U}{\partial_y} = -g\frac{\partial H}{\partial_x}, \tag{4.3a}$$

$$U\frac{\partial V}{\partial_x} + V\frac{\partial V}{\partial_y} = -g\frac{\partial H}{\partial_y}, \tag{4.3b}$$

$$\frac{\partial HU}{\partial_x} + \frac{\partial HV}{\partial_y} = 0, \tag{4.3c}$$

is derived where g, H, U and V are gravity acceleration, total water depth, zonal and meridional vertically averaged components of velocity, respectively. Similar to the work of Borthwick and Kaar (1993), the depth-averaged stream function ψ_d is defined as follows:

$$U = \frac{1}{H}\partial_y\psi_d, \tag{4.4a}$$

$$V = -\frac{1}{H}\partial_x\psi_d. \tag{4.4b}$$

By using (4.4) and the definition of vorticity ($\zeta = \frac{\partial V}{\partial x} - \frac{\partial U}{\partial y}$) an elliptic Poisson equation for the stream function may be written as:

$$\frac{\partial}{\partial x}\left(\frac{1}{H}\frac{\partial\psi_d}{\partial x}\right) + \frac{\partial}{\partial y}\left(\frac{1}{H}\frac{\partial\psi_d}{\partial y}\right) + \zeta = 0. \tag{4.5}$$

In addition, a depth-averaged vorticity transport equation

$$U\frac{\partial \zeta}{\partial x} + V\frac{\partial \zeta}{\partial y} + \zeta\left(\frac{\partial U}{\partial x} + \frac{\partial V}{\partial y}\right) = 0, \tag{4.6}$$

is obtained by cross-differentiation and subtraction of $(4.3\mathrm{a})$ and $(4.3\mathrm{b})$ (see Borthwick and Kaar (1993) for further details). If $\nabla^2\psi_d = K\psi_d$ is valid, the stream function satisfies (4.5) and (4.6). By substituting (4.4) into $(4.3\mathrm{a})$ and $(4.3\mathrm{b})$ with some rearrangement, applying a dimensional analysis, arbitrary choice of stream function as $\psi = A\cos(ax)\cos(ay)$ without a decaying term due to inviscid property of flow, an approximate analytical solution for water elevation might be written as

$$\eta = \left(-\frac{3}{4g}a^2A^2\left(\cos 2\left(ax\right) + \cos 2\left(ay\right)\right) + H_0^3\right)^{\frac{1}{3}} - H_0 \tag{4.7}$$

In addition, the zonal and meridional velocity components are computed as follows:

$$U = \frac{1}{H}\partial_y\psi_d = -\frac{aA}{H}\cos\left(ax\right)\sin\left(ay\right), \tag{4.8a}$$

$$V = -\frac{1}{H}\partial_x\psi_d = \frac{aA}{H}\sin\left(ax\right)\cos\left(ay\right), \tag{4.8b}$$

where A and a are a constant and wave number, respectively. It might be possible to obtain a different approximate analytical solution if a more complex streamfunction is used (see e.g. Kuvshinov and Schep, 2000 for some examples). In addition to the above approximation, much simpler expressions than (4.7) can be obtained for water elevation, if the continuity equation $(4.3\mathrm{c})$ is simplified as below:

$$\frac{\partial U}{\partial_x} + \frac{\partial V}{\partial_y} = 0 \tag{4.9}$$

Therefore, a new approximate analytical solution for water elevation

$$\eta = -\frac{a^2A^2}{4g}\left(\cos\left(2ax\right) + \cos\left(2ay\right)\right) \tag{4.10}$$

is obtained where the depth averaged velocity components are as follows:

$$U = \partial_y \psi = -aA \cos(ax) \sin(ay) \tag{4.11a}$$

$$V = -\partial_x \psi = aA \sin(ax) \cos(ay) \tag{4.11b}$$

4.3 Numerical experiment

The eddies of Honeycomb experiment are designed in a way that they mimic the features of the mesoscale eddies occurred in the baroclinic experiment configured for $Ro = 0.8$ in chapter 5. In this test case, the wavelength, the maximum velocity of eddies are $40\ \mathrm{km}$ and $0.2\ \mathrm{ms}^{-1}$, respectively. There are sixteen eddies in a flat bottom basin with double periodic boundaries, $200\ \mathrm{m}$ depth and $160\ \mathrm{km}$ width (see figure 4.1 for more detail). The steady state flow is studied with the depth-integrated barotropic mode of GETM in Cartesian coordinates. A series of numerical simulations are performed using different advection schemes for three horizontal resolutions of 5 km, 2.5 km and 1.25 km. Tables 4.1 and 4.2 present the list of advection schemes and the parameters used for this experiment, respectively.

The comparison of the results of each advection scheme in figures 4.2.a and 4.2.b shows that the accumulated global numerical dissipation of all simulations are in the same order of their kinetic energy loss. It indicates that the transfer of energy between kinetic energy and potential energy are ignorable. Thus, the kinetic energy loss is only due to numerical dissipation. Table 4.2 compares the ratio of numerical dissipation to initial kinetic energy in the last day of simulation. As it is expected from chapter 2, the results show that the FOU scheme is the most dissipative scheme. It dissipate more than 90 percent of the initial kinetic energy after 25 days. Even increasing the resolution can not decrease the numerical dissipation significantly. The FOU scheme dissipates the kinetic energy in a high resolution configurations more than the dissipation of a dissipative TVD scheme for low resolution configurations. The advection schemes of the first group categorised in section 2.9 (e.g. the third order upwind scheme) dissipate kinetic energy in the same order of the accurate advection schemes of the second group in the same categorisation (e.g., P2-PDM scheme). The MP5 and WENO schemes, the advection schemes of the third group in this categorisation, dissipate kinetic energy less than all schemes. The TVD schemes dissipate energy approximately 10 times more than the MP5 and WENO schemes for the same resolution. However, there is one advection scheme from the second group, the SPL-max-$\frac{1}{3}$ scheme, that dissipates kinetic energy approximately in the same order of the MP5 and WENO schemes. The advection schemes that change the kinetic energy slightly are called neutral schemes. Table 4.2 shows that the numerical dissipation and

global numerical viscosity are decreased with increasing the resolution.

The advection schemes that increase kinetic energy (e.g. Superbee, Super-C schemes) and the ones that decrease kinetic energy (e.g. MUSCL, SPL-$\frac{1}{3}$ schemes) are classified as antidissipative and dissipative schemes, respectively. It is concluded that the third group of the advection schemes presented in section 2.9 includes neutral advcetion schemes. Moreover, according to the results the advection schemes which cause smearing and squaring effects are dissipative and antidissipative schemes, respectively.

Moreover, figures 4.2.c and 4.2.d compare the global effective viscosity and the global

Name	**Limiter**	**Reference**
MUSCL	$\max[0, \min(2r, 1/2 + r/2, 2)]$	Van Leer (1979)
Superbee	$\max[0, \min\{2r, \max(r, 1), 2\}]$	see Waterson and Deconinck (2007)
Super-C	$[\{r > 1 \rightarrow \min(r, 2/(1 - \lvert C_r\rvert), 0 \leq r \leq 1 \rightarrow \min(1, 2r/\lvert C_r\rvert), r = 0 \rightarrow 0\}]$	see Fringer and Armfield (2005)
P2-PDM	$\{\max(0, \min(\phi, 2/(1 - C_r), 2\frac{r}{C_r})), \phi = (1/2+x)+(1/2-x)r, x = (1-2C_r)/6\}$	see Pietrzak (1998)
SPL- $\frac{1}{3}$	$\max[0, \min(2r, 1/3+2r/3, 2/3+r/3, 2)]$	see Waterson and Deconinck (2007)
SPL-max-$\frac{1}{2}$	$\max[0, \min(2r, \max(1/4 + 3r/4), 3/4 + r/4), 2)]$	Waterson and Deconinck (2007)
SPL-max-$\frac{1}{3}$	$\max[0, \min(2r, \max(1/3 + 2r/3, 2/3 + r/3), 2)]$	Waterson and Deconinck (2007)
Van Albada	$r(r + 1)/(r^2 + 1)$	Van Albada et al. (1997)
GPR-0	$r(3r + 1)/(2r^2 + r + 1)$	Waterson and Deconinck (2007)
OSPRE	$3r(r + 1)/[2(r^2 + r + 1)]$	see Waterson and Deconinck (2007)
Name	**Type**	**Reference**
MP5	Geometrical approach (monotonicity preserving, fifth order)	Suresh and Huynh (1997)
WENO	Adaptive stencil (fifth order)	Shu (1998)

Table 4.1: The advection schemes deployed in the Honeycomb test case. The first group of advection schemes is expressed in flux-limiter form. $r = \frac{S_{i+1}-S_i}{S_i-S_{i-1}}$, S and C_r are concentration and Courant number, respectively.

numerical viscosity, respectively. The results of both methods depict a good agreement. The comparison indicates that both methods can compute equal viscosity from different line of thought. The global numerical viscosity and the global effective viscosity are almost constant during the simulation. Therefore, the global numerical viscosity are only compared in the last stage of the simulation. The results show that the antidissipative advection schemes present negative global numerical viscosity and the dissipative advection schemes positive, respectively.

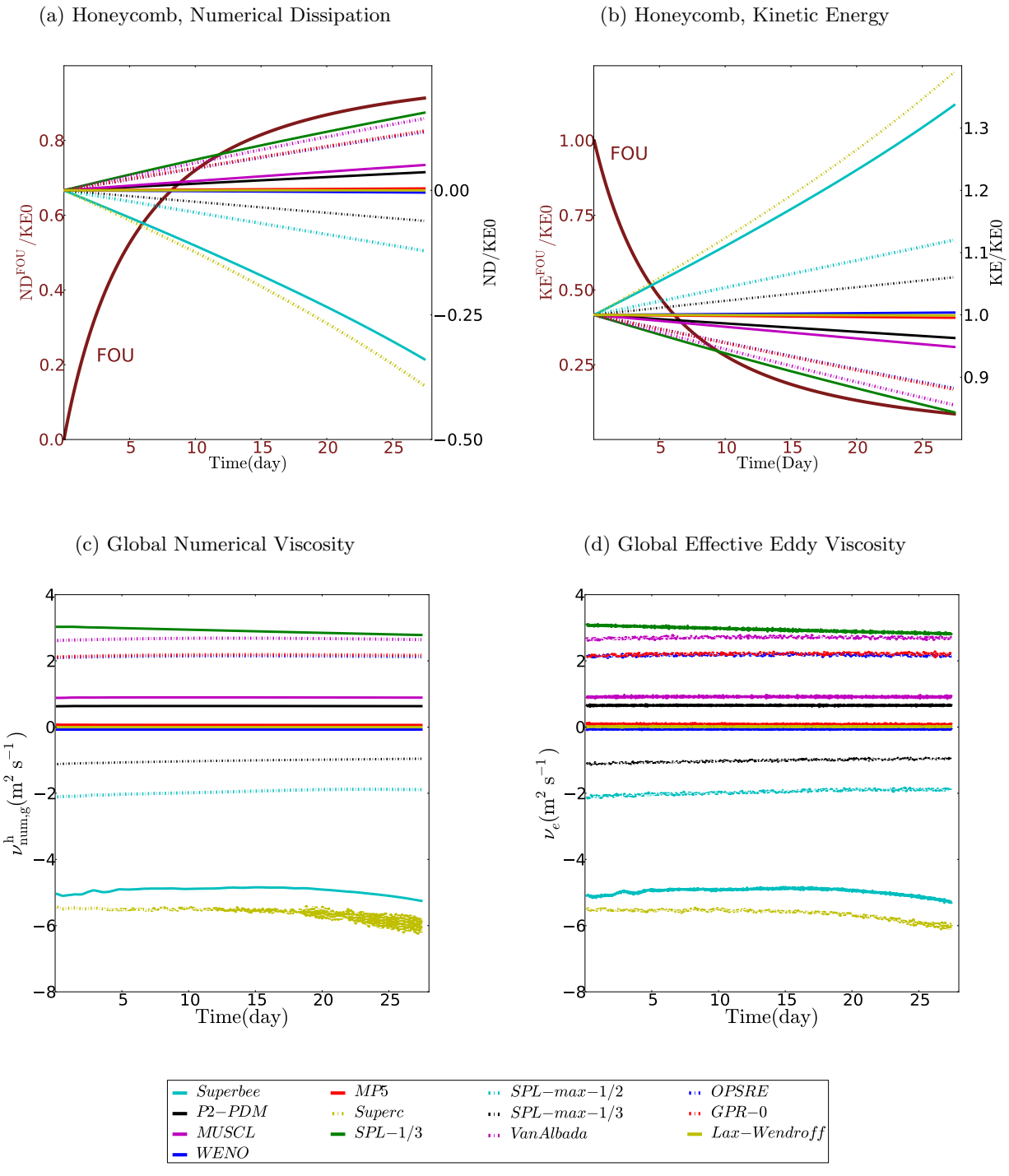

Figure 4.2: Honeycomb test case. (a) Ratio of global accumulated numerical dissipation (ND) to initial kinetic energy (KE0); (b) Ratio of kinetic energy (KE) to initial kinetic energy; (c) Evolution of global numerical viscosity (see section 3.3.4); (d) Evolution of global effective eddy viscosity (see section 3.3.5).

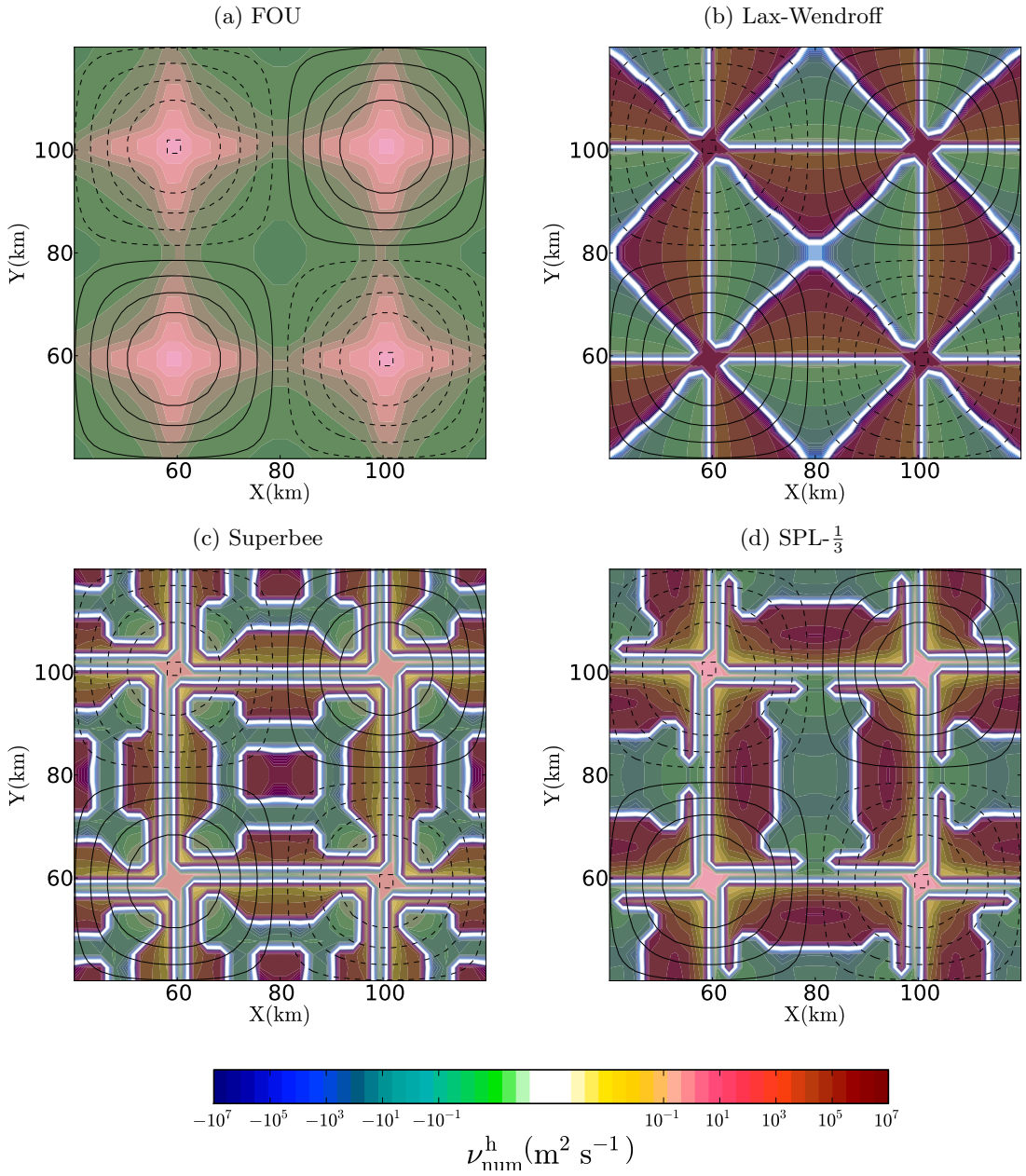

Figure 4.3: Local numerical viscosity for the Honeycomb test case computed from the local numerical viscosity method (see Eq. 3.48) after 2500 seconds.

Grids Properties						
Name	A		B	C		
Number of cells	32*32		64*64	128*128		
Grid size (Δx)	5 km		2.5 km	1.25 km		
Time step (Δt)	5 s		2.5 s	1.25 s		
	Effective viscosity (m^2s^{-1})			**ND/E0**		
Advection scheme	A	B	C	A	B	C
MUSCL	7.345	0.913	0.115	0.335	0.052	0.007
Superbee	-5.189	-4.962	-1.507	-0.340	-0.336	-0.092
Super-C	-15.327	-5.624	-1.548	-0.399	-0.389	-0.094
P2-PDM	5.553	0.652	0.081	0.266	0.038	0.005
SPL-$\frac{1}{3}$	13.298	2.940	0.657	0.523	0.157	0.0380
SPL-max-$\frac{1}{2}$	-0.408	-1.958	-0.691	-0.022	-0.120	-0.0409
SPL-max-$\frac{1}{3}$	1.743	-1.013	-0.421	0.0929	-0.0600	-0.024
Van Albada	15.156	2.699	0.366	0.570	0.145	0.022
GPR-0	12.590	2.202	0.300	0.505	0.12	0.018
OPSRE	13.246	2.168	0.286	0.522	0.118	0.0170
WENO	0.130	-0.064	-0.006	0.008	-0.0029	0.000
MP5	1.540	0.077	0.009	0.082	0.005	0.001
FOU	61.455	40.233	25.716	0.97	0.915	0.798
Lax-Wendroff	0.024	0.012	0.006	0.002	0.001	0.001
Third order upstream	4.156	0.573	0.0779	0.206	0.032	0.0045

Table 4.2: The parameters and results of the Honeycomb test case with a maximum velocity of 0.2 ms^{-1} and water depth of 200 m. Upper panel: resolution and grid size, Lower panel: time averaged global effective numerical viscosity based on the local numerical viscosity method (see Appendix) and ratio of the total accumulated Numerical Dissipation (ND) until the 28th day to initial total kinetic energy (E0).

The neutral schemes, with the least possible numerical dissipation such as the WENO and the MP5 schemes show the least absolute global numerical viscosity. Figure 4.3 displays snapshots of local numerical viscosity of the FOU, Lax-Wendroff, SPL-$\frac{1}{3}$ and Superbee schemes. The numerical viscosity of the FOU scheme as the most dissipative advection scheme is positive in the whole domain, while the Lax-Wendroff scheme generates symmetric pattern of equal positive and negative numerical viscosity. SPL-$\frac{1}{3}$ and Superbee also introduce symmetric pattern of negative and positive numerical viscosity but with different magnitude. A possible explanation for this might be that the local numerical viscosity of TVD schemes is a combination of the FOU scheme and a higher order scheme.

4.4 Summary and conclusion

In this chapter, a system of steady state eddies including an approximate analytical solution of the water elevation is introduced to diagnose the numerical dissipation of advection schemes.

This solution is distinct from the earlier analytical solutions, because it is appropriate for depth average solutions.

The main goal of this chapter was to categorise advection schemes based on their dissipative behaviour when the eddies are stationary. The schemes that generate negative and positive global numerical viscosity are considered as antidissipative and dissipative schemes, respectively. The advection schemes are called neutral schemes that generate the least numerical dissipation, e.g. the MP5, WENO and SPL-max-$\frac{1}{3}$ schemes. The results demonstrated that the schemes with smearing and squaring effects are dissipative and antidissipative, respectively. A notable result is that the Lax-Wendroff and third order upwind schemes conserve the total kinetic energy as well as accurate TVD advection schemes. This rises the question whether the advection schemes of the first group of categorisation in section 2.9 are also appropriate choices for the advection terms of the momentum equations. The second major finding was that the antidissipative and dissipative advection schemes present negative and positive global numerical viscosity, respectively. In addition, it was shown that both methods of computing global numerical viscosity and global effective viscosity generate same results, although they are developed from different line of thought. Since the simulations in chapter 5 are expensive, a few advection schemes are selected here only for continuing analysis. The WENO, MP5, SPL-max-$\frac{1}{3}$, P2-PDM advection schemes are selected as neutral schemes for the simulations which generates th least numerical dissipation in chapter 5. The Superbee and SPL-$\frac{1}{3}$ advection schemes are also selected as examples of antidiffusive and diffusive advection schemes, respectively.

5 Effects of advection schemes on lateral shear and baroclinic instabilities

Numerical mixing and dissipation are inseparable portions of mixing and dissipation in ocean models. Therefore, the lateral shear stresses, the intensity of buoyancy gradients and consequently the stratification processes are affected by the used advection schemes. In this chapter two numerical experiments are introduced to investigate the numerical effects of advection schemes on lateral shear instability and restratification process. All simulations are performed for inviscid flow, therefore the dissipation and loss of energy are due to numerical errors. The first experiment, the lateral shear instability adds to the results from the Honeycomb experiment, because in contrast to the Honeycomb experiment that is designed for smooth, stationary velocity field, it includes sharp discontinuities in the initial velocity field. Although these 2D experiments provid good insight into the dissipative behaviour of advection schemes, it is necessary to investigate the numerical effects of advection schemes for a more realistic 3D flow including both the momentum and the tracer equations. In the analysis presented in this chapter, first, the dissipative behaviour of advection schemes is studied. Then, their effects on instabilities are investigated. The baroclinic instability experiment is configured for two cases with small and large Rossby numbers that mimic the behaviour of mesoscale and submesoscale eddies, respectively. Since the numerical experiments are computationally demanding, only a few advection schemes are selected for further analyses.

5.1 Lateral shear instability

The lateral shear instability experience is designed as a mid latitude zonal jet. The physical properties of this experience i.e. water depth and maximum zonal velocity are adjusted so that the initial background flow may represent for instance the Gulf stream (see figure 5.1). It is assumed that the flow is inviscid and instability is studied in Cartesian coordinates with f-plane approximation. The instability is developed in a zonal, frictionless, flat bottom reentrant channel. Initially, the flow is a background zonal jet with 1000 m depth and 50 km

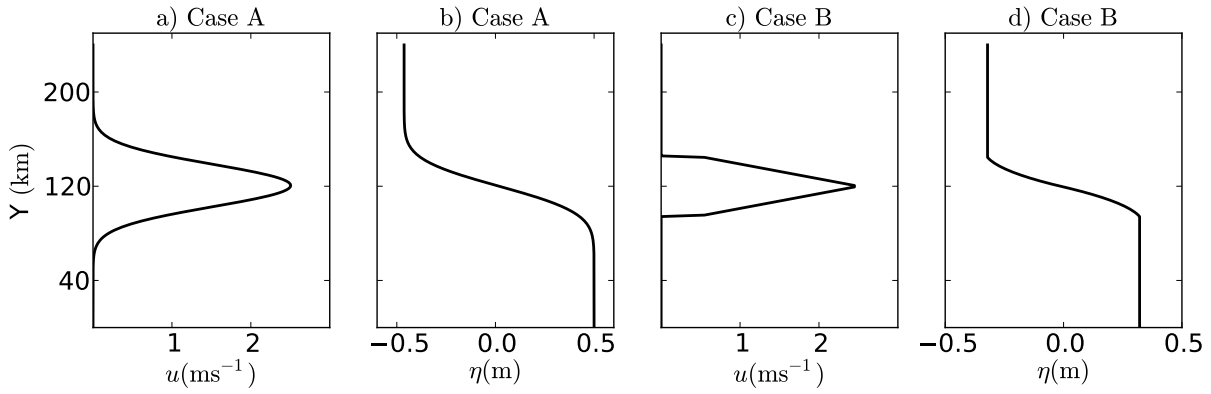

Figure 5.1: Initial conditions for the lateral shear instability test case. a,b : Zonal velocity and surface elevation for test case A; c,d : Zonal velocity and surface elevation for test case B; $u_{max} = 2.5\mathrm{ms}^{-1}$.

width. Since physical viscosity is not introduced to the model, all the dissipation are due to numerics. The simulation is conducted for three horizontal resolutions of 5 km, 2.5 km and 1.25 km. Since the high resolution configuration of the experiment generates the least numerical dissipation, the results of the finer grids are considered as reference. The experiment is configured for two different types of zonal velocity distribution to challenge the advection schemes in case of discontinuities and smooth conditions. Case A described by (5.1) is a jet with normal meridional distribution of zonal velocity and the velocity profile of case B explained by (5.2) is combination of a box and a point jet (concentration of vorticity at one point).

$$\mathrm{u(y)} = \mathrm{u_{max}} \exp[\frac{-(\mathrm{y}-\mathrm{yc})^2}{2\sigma^2}] \tag{5.1}$$

$$\mathrm{u(y)} = \begin{cases} 0 & \mathrm{y} > \mathrm{y_2} \\ \mathrm{u_{max}} - \mathrm{u_{box}} \frac{|\mathrm{y}-\mathrm{y_c}|}{\mathrm{y_2}-\mathrm{y_c}} & \mathrm{y_1} \leq \mathrm{y} \leq \mathrm{y_2} \\ 0 & \mathrm{y} < \mathrm{y_1} \end{cases} \tag{5.2}$$

In the above relation, y is the meridional distance from southern solid boundary, and $\sigma = 18000\ \mathrm{m}$, $\mathrm{u_{max}} = 2.5\ \mathrm{ms}^{-1}$, $\mathrm{u_{box}} = 2.0\ \mathrm{ms}^{-1}$, $\mathrm{y_c} = \mathrm{L_y}/2$, $\mathrm{y_1} = \mathrm{L_y}/4$, $\mathrm{y_2} = 3\mathrm{L_y}/4$ are chosen such that $\mathrm{L_y} = \mathrm{L_x} = 240\ \mathrm{km}$ denote the width and length of the channel, respectively. The geostrophically adjusted surface elevation η which are computed numerically using initial zonal velocity (see Fig. 5.1) is perturbed to generate lateral shear instability. The initial perturbations are amplified by extracting energy from the background flow. Then, unstable vortices are generated which finally evolve into much larger ones. This process causes an exchange of

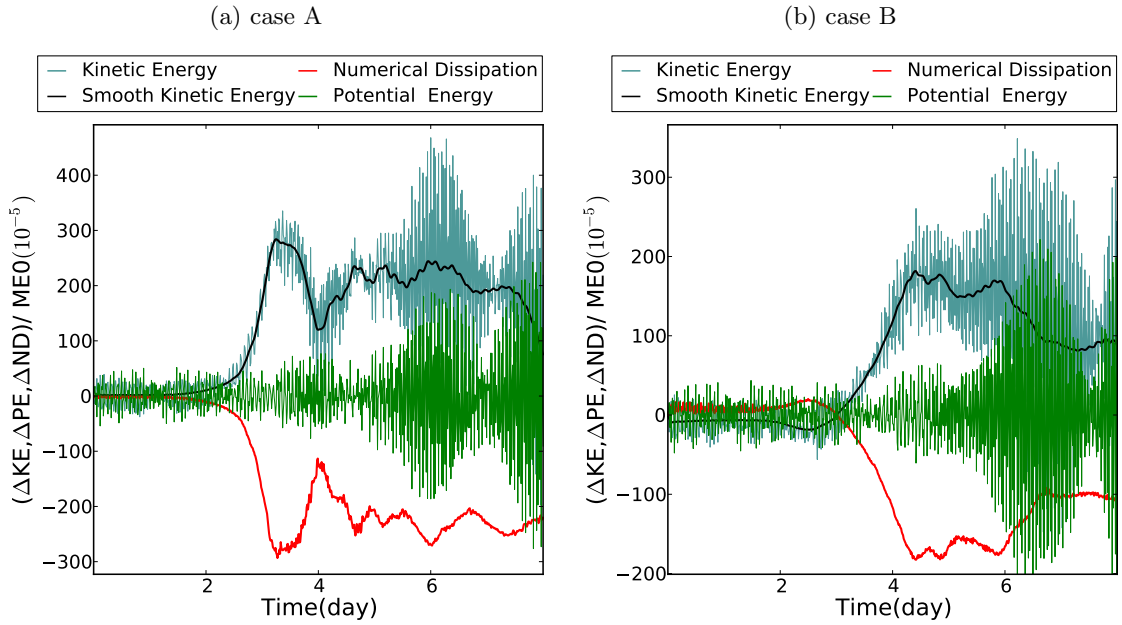

Figure 5.2: Exchange of energy between kinetic energy, potential energy and numerical dissipation. The noisy portion of kinetic energy is in balance with potential energy. The kinetic energy is dissipated just due to numerical dissipation. ΔKE, ΔPE, ΔND and ME0 are kinetic energy exchange rate, potential energy exchange rate, numerical dissipation rate and initial mechanical energy.

energy between mean and eddy energy. Figure (5.2) demonstrates that the kinetic energy are dissipated only due to numerical dissipation. The noisy portion of kinetic energy is balanced with the noisy portion of potential energy and the kinetic energy loss is equal to the global numerical mixing rate. The former is associated with fast surface gravity waves and the latter is associated with the vortical dynamics. Figure 5.3 shows the evolution of the vorticity field for both cases simulated by the MP5 scheme which generates the least numerical dissipation for the high resolution configuration.

Figures 5.4 and 5.5 compare snapshots of local numerical viscosity of the Superbee and the SPL-$\frac{1}{3}$ schemes. For both cases the Superbee scheme generates the largest area of negative values and the SPL-$\frac{1}{3}$ scheme generates mostly positive local numerical viscosity. Figures 5.6.a and 5.6.b compare numerical dissipation of lowest resolution configuration in cases A and B. The Superbee and SPL-$\frac{1}{3}$ advection schemes show antidissipative and dissipative behaviour for the both cases, respectively. Figures 5.6.c and 5.6.d demonstrate that the dissipative scheme, the SPL-max-$\frac{1}{3}$ scheme, shows positive and the antidissipative schemes, the Superbee scheme, shows negative global numerical viscosity. MP5 and SPL-max-$\frac{1}{3}$ (neutral schemes) demon-

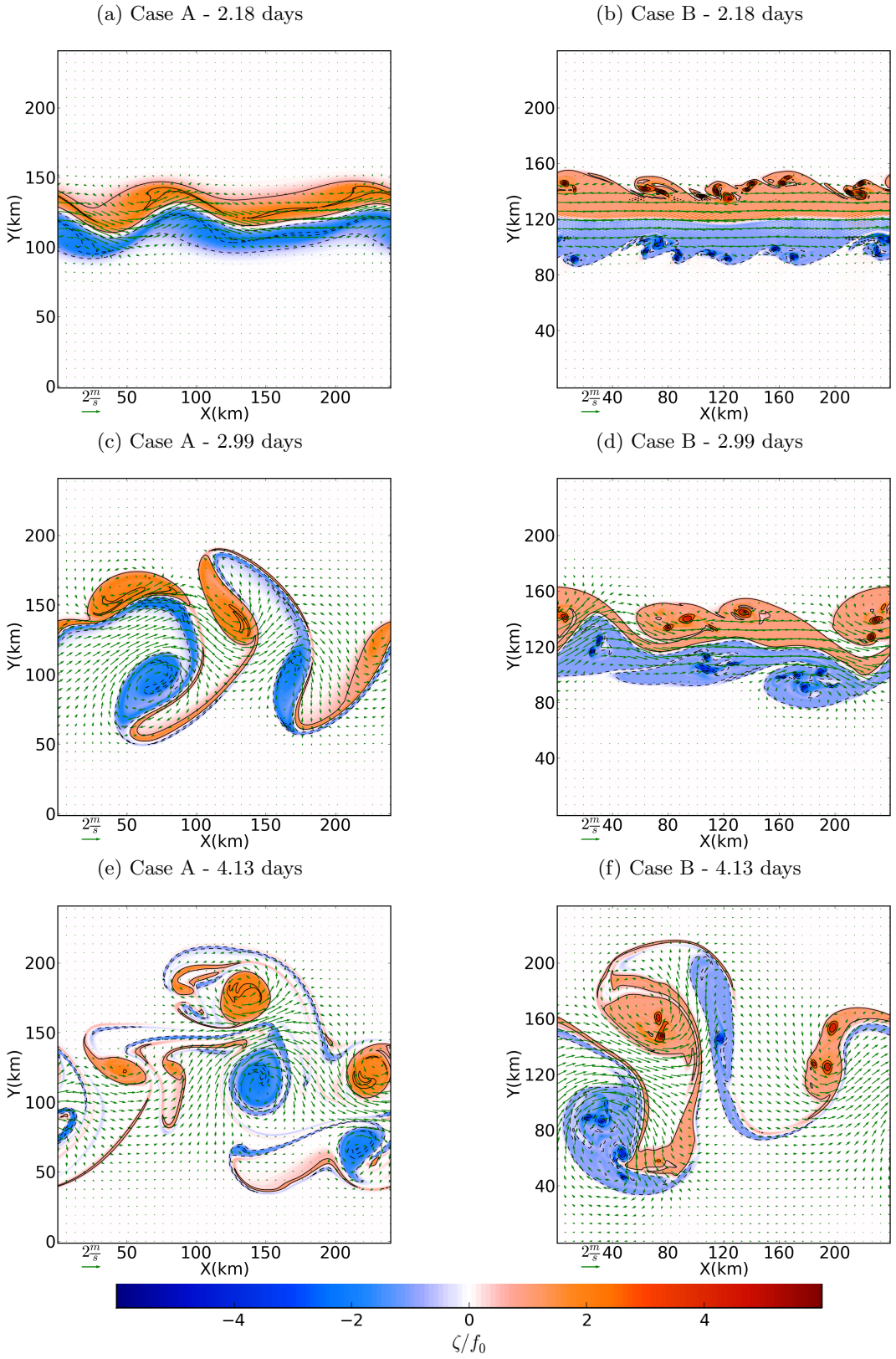

Figure 5.3: Time evolution of the vorticity and velocity field of case A (a,c,e) and case B (b,d,f) for the lateral shear instability test case using MP5 advection scheme for resolution R3.

strate a relatively small global numerical viscosity. In addition, global numerical viscosity of Superbee scheme in case B is positive in the earlier stage of instability. FLMs increase the portion of the first order upwind advection scheme in the solution to guarantee monotonicity and consequently damp the numerical oscillation. Later, the sharp gradients are smoothed and kinetic energy is increased again due to the antidissipative behaviour of Superbee scheme.

Table 5.1 compares the ratio of the total accumulated numerically dissipated energy to the total initial mechanical energy for three resolutions. For both cases increasing the resolution reduces the numerical dissipation. As it is expected, the first order upwind advection scheme shows the highest amount of dissipation. In addition, the Superbee and SPL-$\frac{1}{3}$ schemes have the highest negative and positive numerical dissipation among the TVD schemes. The SPL-max-$\frac{1}{3}$ and MP5 schemes generate the least absolute dissipation. The results of the third order upwind scheme for the high resolution experiment is comparable with the WENO and MP5 schemes. However, the Lax-Wendroff scheme that dissipates energy in the Honeycomb experiment, less than the third order upwind is numerically unstable for the parameter used in this experiment. It indicates that although the advection schemes of the first group of advection schemes categorised in section 2.9 might be appropriate choice for the advection terms of momentum equations, they might need artificial uniform viscosity to be numerically stable.

Figures 5.6.e and 5.6.f compare the total eddy kinetic energy of the cases A and B, respectively. For the case A, the low-resolution simulations using the WENO, MP5 and SPL-max-$\frac{1}{3}$ schemes generate similar eddy kinetic energy to the high-resolution simulation using the MP5 scheme. However, in case B, the higher resolution reference simulation resolves more eddies and generates higher level of eddy kinetic energy.

5.2 Baroclinic instability

Oceans have relatively large scale horizontal buoyancy gradients which is the main driver of the baroclinic instabilities. The consequence of such instabilities is restratification of the ocean by slumping isopycnals and mixing the tracer fields horizontally. Thus, advection schemes with different intensity of numerical mixing and dissipation may affect the stratification. Subsequently, the mixing parameterisation deduced from numerical experiments depend on the used advection scheme. An eddying channel flow experiment is used to diagnose the effects of numerical mixing and dissipation on baroclinic instabilities. Such configurations are often used to validate mixing parameterisations (e.g., Fox-Kemper et al., 2008; Eden, 2010, 2011;

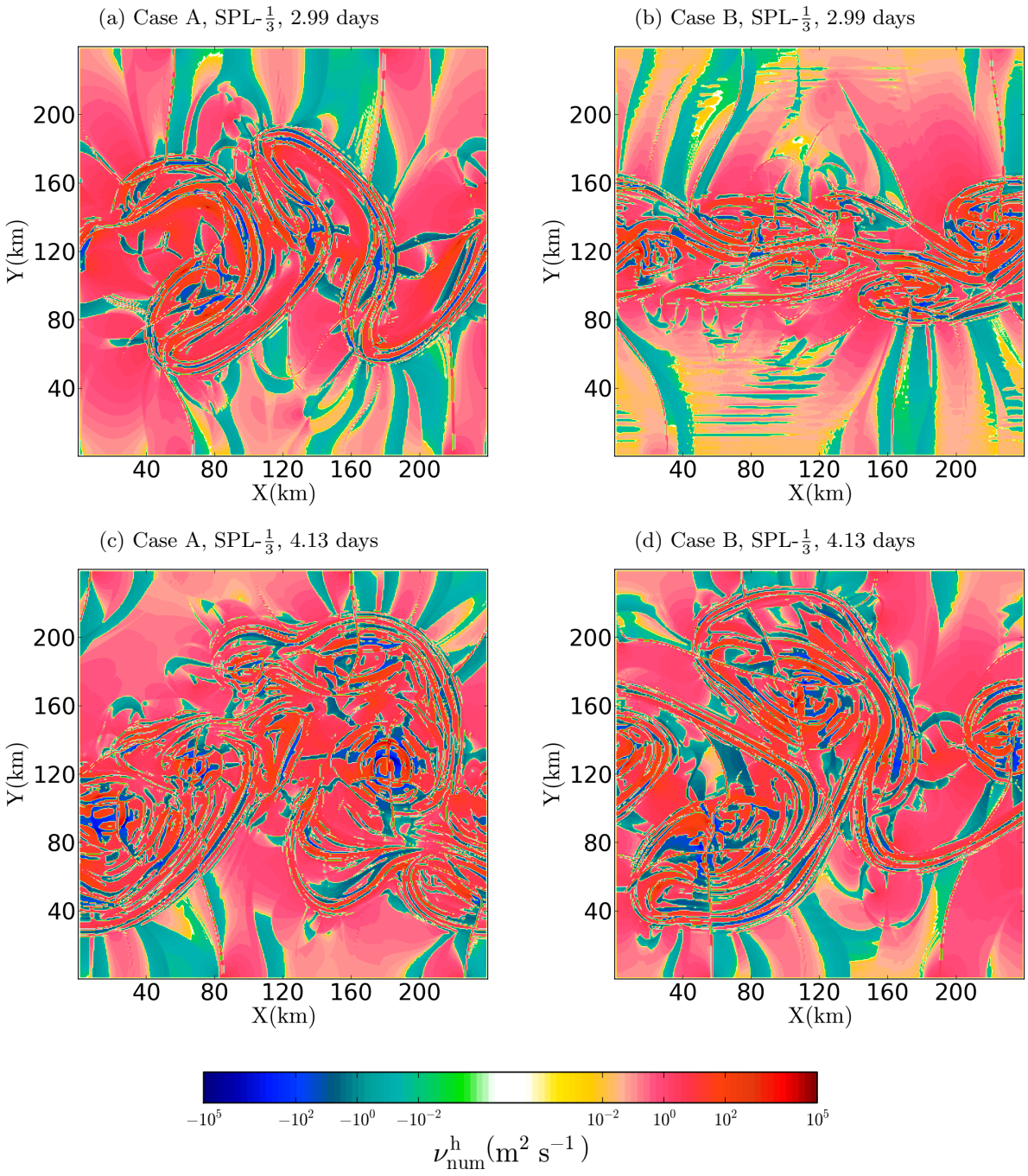

Figure 5.4: Local numerical viscosity (see Eq. 3.48). Panels for resolution R3 (a,b) display Superbee as anti-dissipative scheme, Panels (c,d) show SPL-$\frac{1}{3}$ scheme viscosity as dissipative scheme.

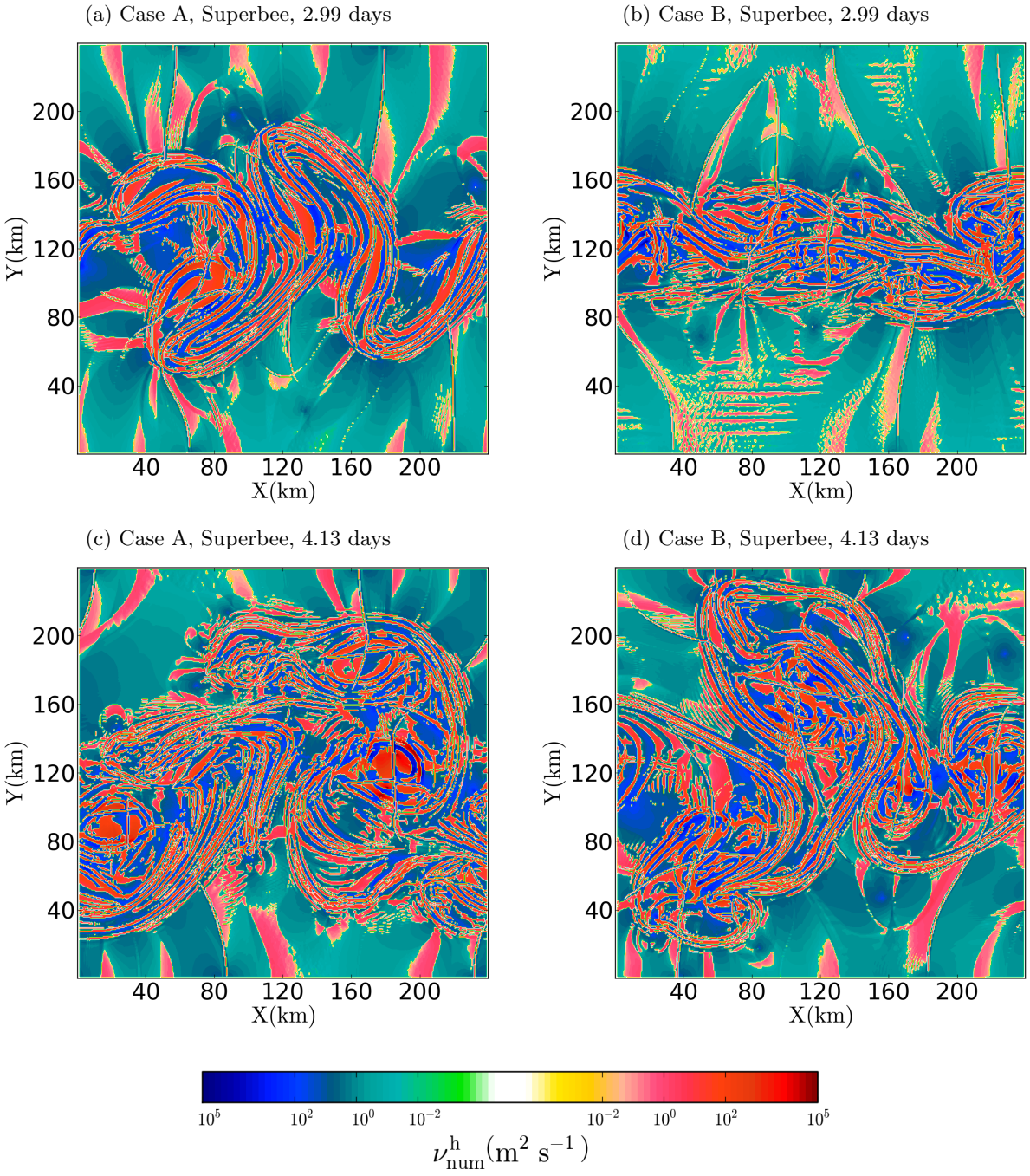

Figure 5.5: Local numerical viscosity (see Eq. 3.48). Panels for resolution R3 (a,b) display Superbee as anti-dissipative scheme, Panels (c,d) show SPL-$\frac{1}{3}$ scheme viscosity as dissipative scheme.

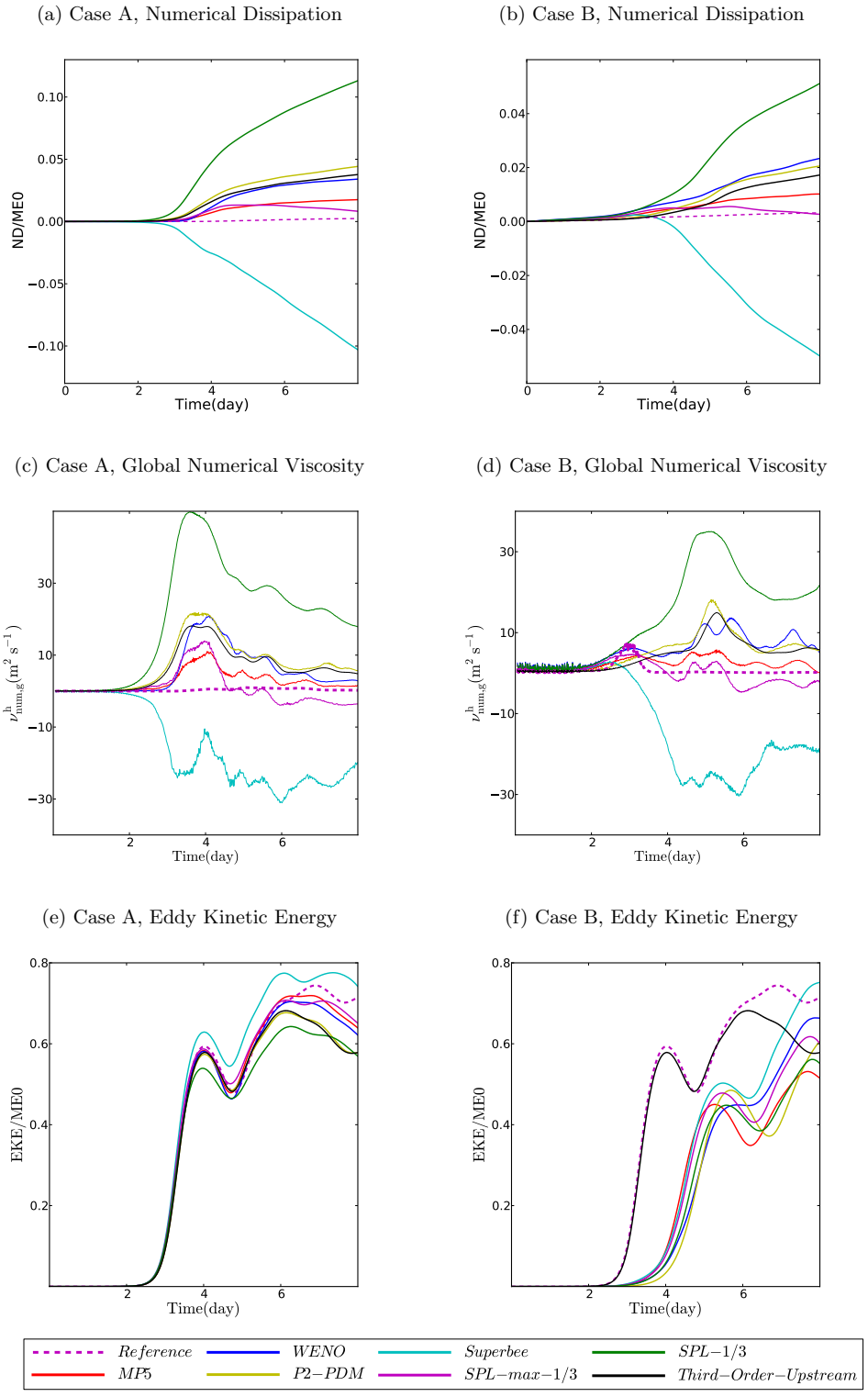

Figure 5.6: Lateral shear instability test case for resolution R1: (a,b): ratio of (accumulated) global numerically dissipated energy to initial mechanical energy;(c,d): ratio of total Eddy Kinetic Energy (EKE) to total initial mechanical energy; (e,f): comparison of global numerical viscosity.

Grids Properties						
Name	R1		R2		R3	
Number of cells	96*96		192*192		384*384	
Cell size (Δx)	2.5 km		1.25 km		0.625 km	
Time step (Δt)	1.0 s		0.5 s		0.25 s	
ND/ME0	Case A			Case B		
Advection scheme	R1	R2	R3	R1	R2	R3
FOU	0.5910	0.4996	0.3748	0.5910	0.3467	0.2237
Thirs Order Upstream	0.0417	0.0106	0.0028	0.0202	0.0075	0.0033
P2-PDM	0.0490	0.0120	0.0031	0.0241	0.0087	0.0035
Superbee	-0.1255	-0.0447	-0.0175	-0.0596	-0.0289	-0.0175
SPL-max-$\frac{1}{3}$	0.0057	-0.0046	-0.0030	0.0025	-0.0015	-0.0015
SPL-$\frac{1}{3}$	0.1263	0.0386	0.0119	0.0629	0.0218	0.0100
MP5	0.0189	0.0047	0.0012	0.0115	0.0078	0.0067
WENO	0.0362	0.0092	0.0026	0.0257	0.0118	0.0088

Table 5.1: The parameters and results of the lateral shear instability test case. First panel: resolution and grid size, Second panel: The ratio of the (accumulated) global numerically dissipated energy (ND) to initial total kinetic energy (ME0) until the 8th day.

Skyllingstad and Samelson, 2012). The configuration used in this study resembles the models from Eady (1949) and Stone (1966) (see Brüggemann and Eden (2014) for more details). The analytical solutions derived in (Eady, 1949; see section 3.1.10) are only valid for large Richardson numbers and therefore quasi-geostrophic dynamics. For Richardson number of order one, only approximate analytical solutions can be found (e.g., Stone, 1966). These solutions are often used to infer on the growth rate and the wave length of the fastest growing unstable wave in a baroclinically unstable environment (e.g., Boccaletti et al., 2007; Fox-Kemper et al., 2008; Skyllingstad and Samelson, 2012). The comparison demonstrates a good agreement between the length scale of the fastest growing wave in the model and the length scale suggest by linear theory.

This test case is a zonal, re-entrant, flat-bottom channel on the f-plane with a constant vertical and meridional buoyancy gradient and a zonal background velocity in thermal wind balance which is unstable to small perturbations. The northern and southern solid boundaries are considered as free slip. Table 5.2 summarises the parameters and variable used to design the configurations. The configurations differ in their horizontal grid sizes and dynamical regimes, namely with Rossby numbers of 0.1 and 0.8, respectively. Thereby, we refer simulations to be mesoscale if their background state is characterised by $Ro = 0.1$. On the other hand, simulations with a background state that is characterised by $Ro = 0.8$ are referred to as

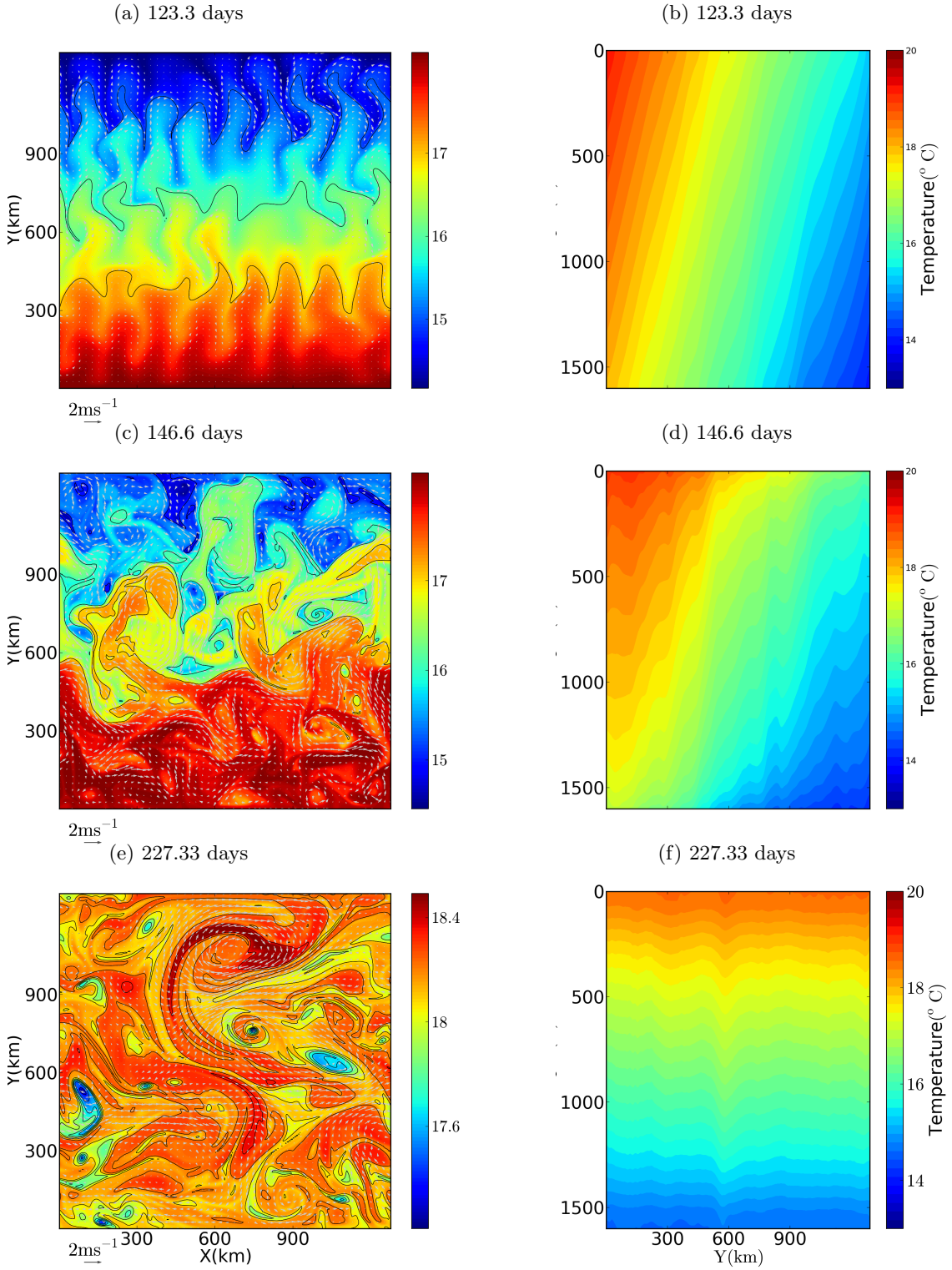

Figure 5.7: The configuration with $Ro = 0.1$ of baroclinic instability test case using MP5 advection scheme for resolution D. (a,c,e): contours of horizontal surface temperature and velocity field (arrows); (b,d,f): zonal average contours of temperature.

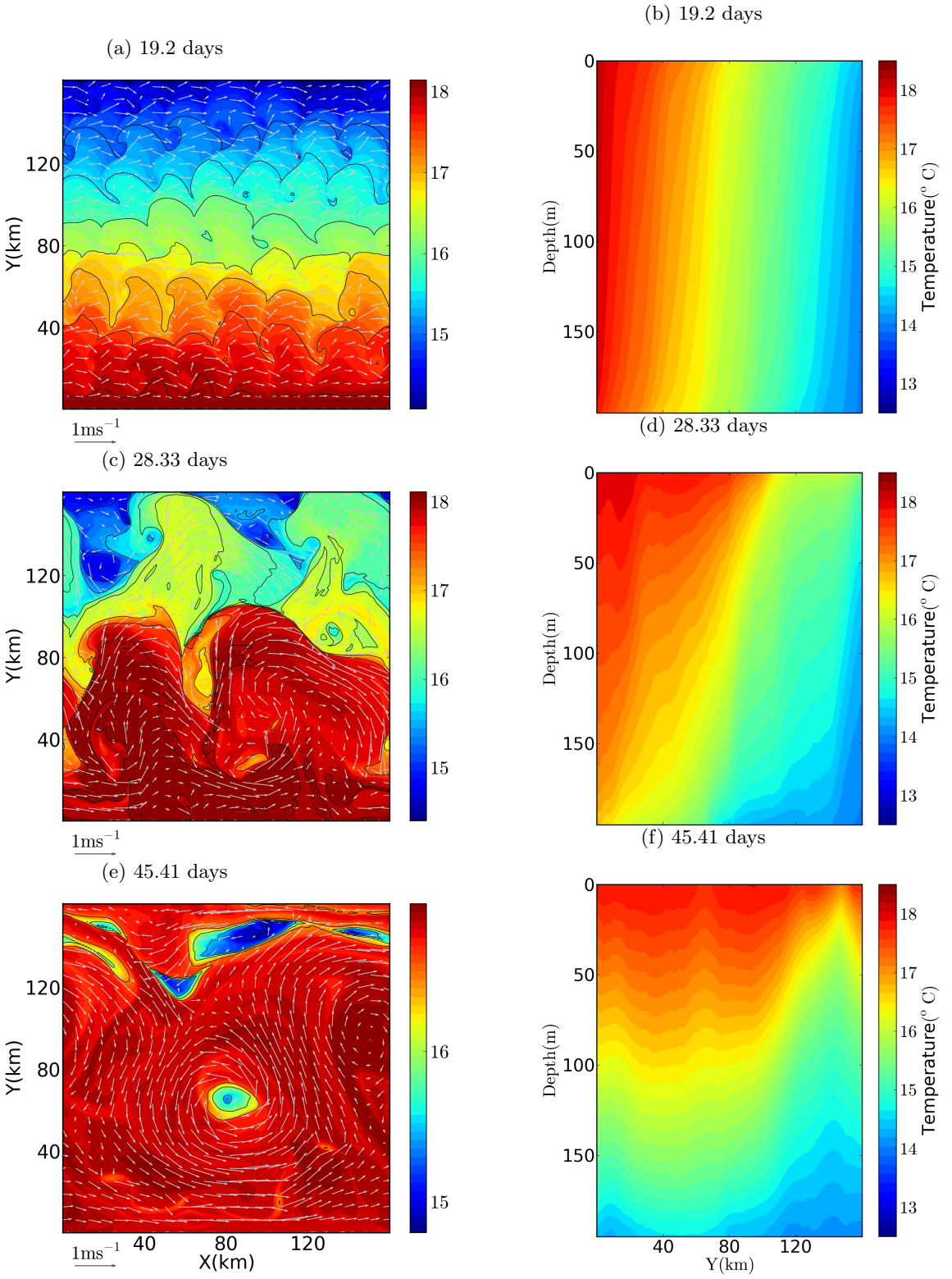

Figure 5.8: The configuration with $Ro = 0.8$ of baroclinic instability test case using MP5 advection scheme for resolution D. (a,c,e): contours of horizontal surface temperature and velocity field (arrows); (b,d,f): zonal average contours of temperature.

submesoscale. While small Rossby numbers are typical for most situations in the ocean interior, Rossby numbers of order one might be found within the upper ocean mixed layer. The grid sizes for the setups A, B, C, D for the submesoscale configuration are 5 km, 2.5 km, 1.25 km and 0.625 km and for the mesoscale configuration are 40.0 km, 20.0 km, 10.0 km and 5.0 km, respectively. To generate instability, small perturbations are added to the temperature field which grow continuously until finite amplitude baroclinic waves are developed (figures 5.7.a and 5.8.a). The zonal scale of the fastest growing modes, $\mathrm{L_s}$, the classical Eady solution for the mesoscale configuration and Stone's approximation for the finite Richardson numbers Ri, $\mathrm{k_s}$,

$$k_s = \sqrt{\frac{5/2}{1 + Ri}} \frac{f}{U_0} \tag{5.3}$$

for the submesoscale configuration are approximated as $L_s \approx 156 \ \mathrm{km}$ and $L_s \approx 25.175 \ \mathrm{km}$, respectively. In (5.3), k_s, U_0 and Ri are wavenumber, velocity scale and Richardson number, respectively. At the phase that finite amplitude baroclinic waves are developed, the computed scale of maximum instability based on spectral analysis of velocity field is 155 km and 25 km for both dynamical regimes, respectively. Growth of unstable waves (see figures 5.7.c and 5.8.c) is driven by a conversion of available potential energy into eddy kinetic energy. Later, the meanders gradually evolve into closed asymmetric eddies for the submesoscale configuration and symmetric dipoles for the mesoscale setup (see figures 5.7.e and 5.8.e). Note that the same advection schemes for all spatial directions are selected for the momentum and tracer equations. However, due to the fact that the MP5 and WENO schemes are very expensive algorithms they are selected here only for the horizontal direction. The vertical advection scheme applied together with the WENO and MP5 schemes is the P2-PDM scheme for both tracer and momentum equations. The P2-PDM scheme is also selected as vertical advection scheme for the third order upwind scenario.

5.2.1 Background potential energy

Figures 5.9.a and 5.9.b compare the time evolution of background potential energy (BPE) for the mesoscale and submesoscale configurations, respectively. It is indicated that a larger portion of available potential energy (APE) is dissipated for the mesoscale configuration than for the submesoscale configuration. The SPL-$\frac{1}{3}$ scheme, for example, dissipates 5 and 10 percent of initial mechanical energy of the submesoscale and mesoscale configurations. Figures 5.9.c and 5.9.d compare the BPE of the model for all four resolutions of both configurations when

Grids properties								
Configuration	**Configuration with** $Ro = 0.8$				**Configuration with** $Ro = 0.1$			
Resolution	A	B	C	D	A	B	C	D
Horizontal cells number (N_x, N_y)	32*32	64*64	128*128	256*256	32*32	64*64	128*128	256*256
Horizontal grid size (Δx, km)	5.0	2.5	1.25	0.625	40.0	20.0	10.0	5.0
Time step (Δt, s)	8.0	4.0	2.0	1.0	64.0	32.0	16.0	8.0

Parameters			
Name	**Symbol**		
Rossby number	Ro	0.8	0.1
Velocity scale	U_0	$0.2\ \mathrm{ms}^{-1}$	
Coriolis frequency	f_0	$5.0 \times 10^{-5}\mathrm{s}^{-1}$	
Rossby radius of deformation	$L_0 \approx \frac{U_0}{f_0 Ro} \approx \frac{NH}{f_0}$	5000.0 m	40000.0 m
Richardson number	$Ri = 1./Ro^2$	1.562	100
Channel width & length	$L_y \approx L_x \approx 32L_0$	160 km	1280 km
Water depth	H	200 m	1600 m
Aspect ratio	$(\delta = H/L_0)$	4.0×10^{-2}	
Vertical buoyancy gradient	$N^2 = (Lf_0/H)^2 = (f_0/\delta)^2$	$1.56 \times 10^{-6}\mathrm{s}^{-2}$	
Horizontal buoyancy gradient	$M^2 = U/(f_0 H) = [Ro/\delta f_0^2]$	$5.0 \times 10^{-8}\mathrm{s}^{-2}$	$6.25 \times 10^{-9}\mathrm{s}^{-2}$

Table 5.2: The resolutions and parameters used in the baroclinic test case.

approximately 70 and 65 percent of APE are released, respectively (the average percentage of maximum released APE of all advection schemes for resolution A in first phase). It is shown that refining the grids generally decreases the BPE. It is also shown that all advection schemes dissipate energy globally in the restratification phase. From the outset of the simulation until approximately day 40 for the submesoscale configuration and day 200 for the mesoscale configuration, the instability restratifies the fluid. During this phase the initial sharp temperature gradients are smoothed and all advection schemes present globally diffusive behaviour, as already seen in case B of the lateral shear instability setup (see figure 5.6.d), where all schemes are dissipative initially. After that stage which coincides with the threshold of switching from the initial semi-3D flow to a two-dimensional flow including eddies with larger size, the horizontal temperature gradients are weak, and the vertical heat flux is decreased. Consequently, the advection schemes are less diffusive in the second phase. In all configurations, SPL-$\frac{1}{3}$ and Superbee are the most diffusive and antidiffusive schemes, respectively.

Figures 5.10.a and 5.10.b compare the averaged numerical diapycnal diffusivity $k_{\mathrm{avg}}^{\mathrm{num}}$ of some advetcion schemes for case C. It becomes evident that the most diffusive schemes results in the largest effective diffusivity. In addition, the averaged numerical diapycnal diffusivity of different advection schemes in the mesoscale configuration are clearly distinct. In contrast, the results of different advection schemes of the submesoscale configuration are approximately

in the same order because all advection scheme are initially diffusive. In all configurations, SPL-$\frac{1}{3}$ and Superbee are the most diffusive and antidiffusive schemes, respectively.

Figures 5.10.c and 5.10.d compare the maximum averaged numerical diapycnal diffusivity of different advection schemes computed for the three different horizontal resolutions. Increasing the horizontal resolution decreases the maximum averaged numerical diapycnal diffusivity for the mesoscale configuration. In contrast, refining the grids, increases the maximum averaged numerical diapycnal diffusivity for the submesoscale configuration. A possible explanation for this is that the eddies in the resolutions with $\frac{\Delta x}{Rd}$ smaller than 0.5 are properly resolved. Thus, the denominator in (3.50) might be dominant.

5.2.2 Numerical dissipation

Figures 5.11.a and 5.11.b compare accumulated global numerically dissipated energy of the mesoscale configuration and the submesoscale configuration, respectively. very similar to the previous analysis, the numerical dissipation analysis, demonstrates that the numerical dissipation evolves in two phases. The first phase is during the restratification process which causes the highest level of dissipation, and the second phase is associated with a quasi two-dimensional flow. All advection schemes in the first phase are globally dissipative. However, in the second phase, when the momentum gradients are smooth, the antidissipative schemes represent negative global numerical dissipation..

In all configurations, SPL-$\frac{1}{3}$ and Superbee are the most dissipative and antidissipative schemes, respectively. The portion of dissipated energy in both regimes are approximately in the same order. Figures 5.11.d and 5.11.c compare the numerical dissipation of the model for the mesoscale and the submesoscale configurations when approximately 70 and 65 percent of APE are released, respectively. It is demonstrated that increasing the horizontal resolution generally decreases the numerical dissipation.

5.2.3 Available potential energy

Figures 5.12.a and 5.12.b compare the time evolution of the APE of different advection schemes. In the mesoscale configuration, the advection schemes generate different results. The antidissipative schemes reduce APE more than the others for all resolutions. The Superbee scheme reduces APE most and the difference of final APE of the Superbee scheme with the most diffusive advection scheme, SPL-max-$\frac{1}{3}$, is about 5 percent of total initial mechanical energy. The sensitivity analysis (see figures 5.13.a and 5.13.b) to the grid size demonstrates that the low resolution experiments release much less APE in the first phase than the high

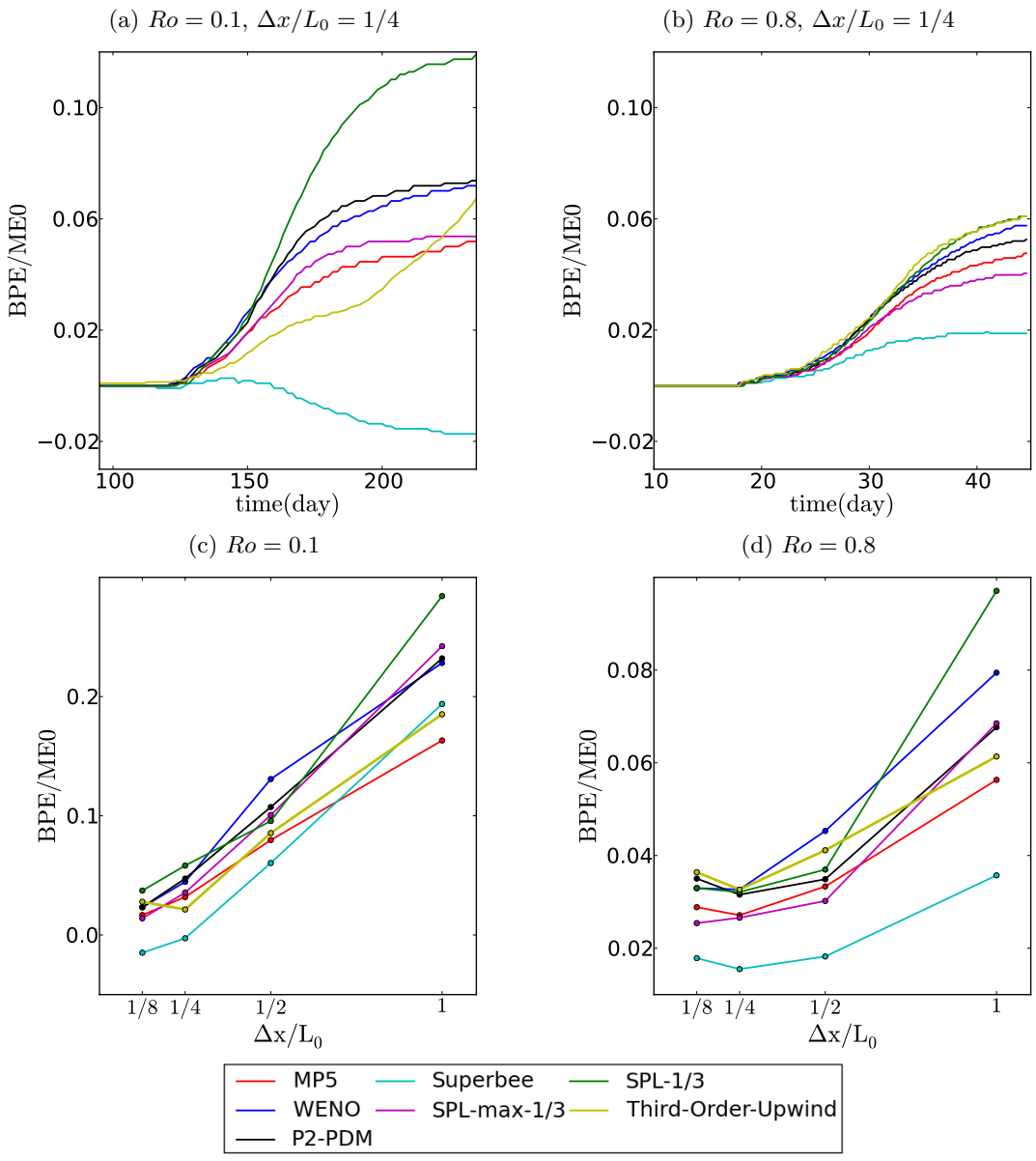

Figure 5.9: Baroclinic instability test case. Ratio of background potential energy to initial total mechanical energy. ME0, L_0 and Δx are initial total mechanical energy, initial Rossby radius of deformation and grid size, respectively. (a,b): Time evolution of background potential energy for the mesoscale configuration and the configurations with $L_0 = 0.8$ for resolution C; (c): Background potential energy of the submesoscale configuration when 70 % of available potential energy is released; (d): Background potential energy of the submesoscale configuration when 65 % of available potential energy is released.

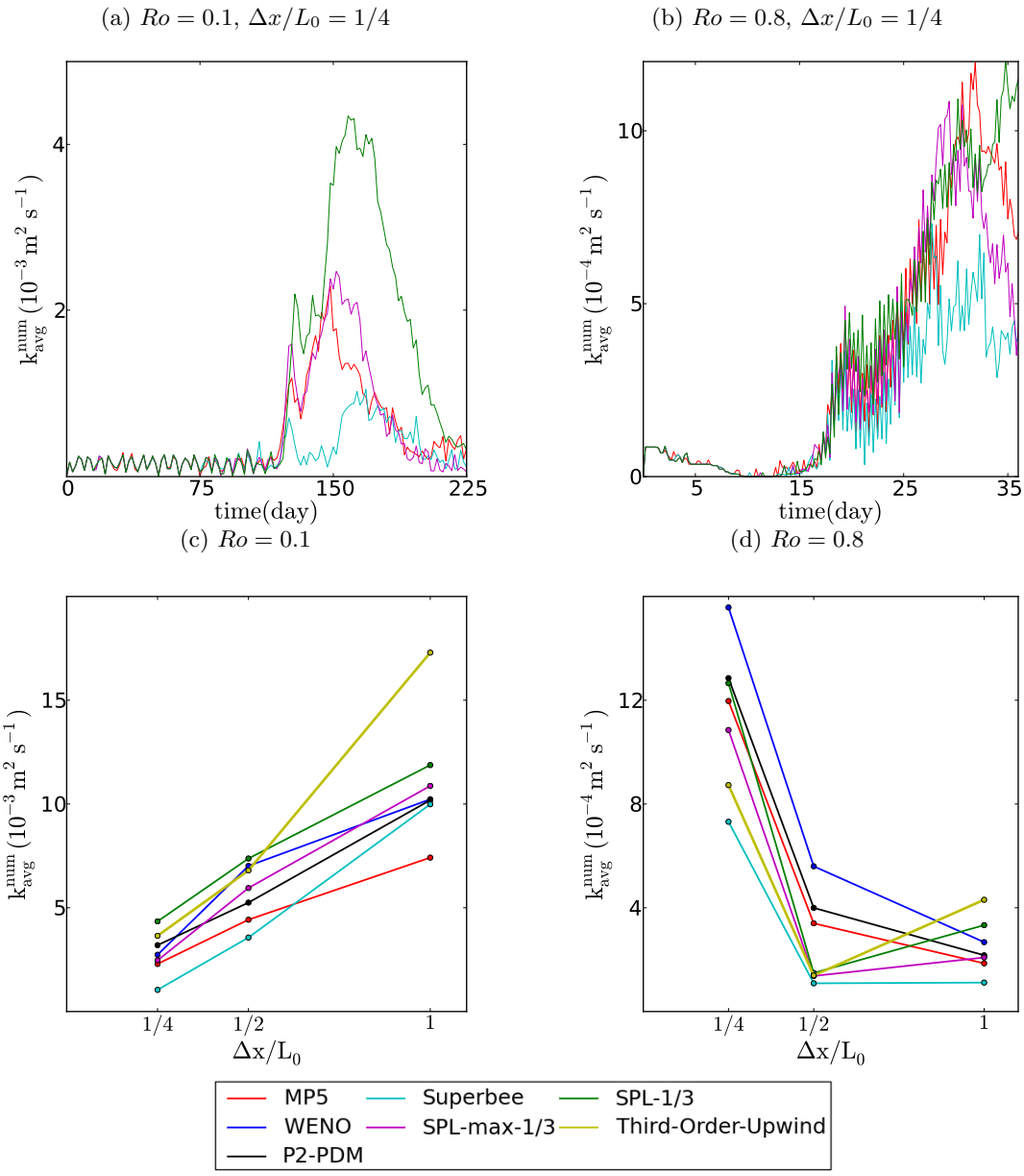

Figure 5.10: Baroclinic instability test case. L_0, $k_{\text{avg}}^{\text{num}}$ and Δx are initial Rossby radius of deformation, averaged numerical diapycnal diffusivity and grid size for resolution C for four different advection schemes (SPL-$\frac{1}{3}$, Superbee, MP5, SPL-max-$\frac{1}{3}$). (a,b): Evolution of numerical diapycnal diffusivity of the mesoscale and the submesoscale configurations; (c): maximum numerical diapycnal diffusivity of the mesoscale configuration; (d): maximum numerical diapycnal diffusivity of the submesoscale configuration.

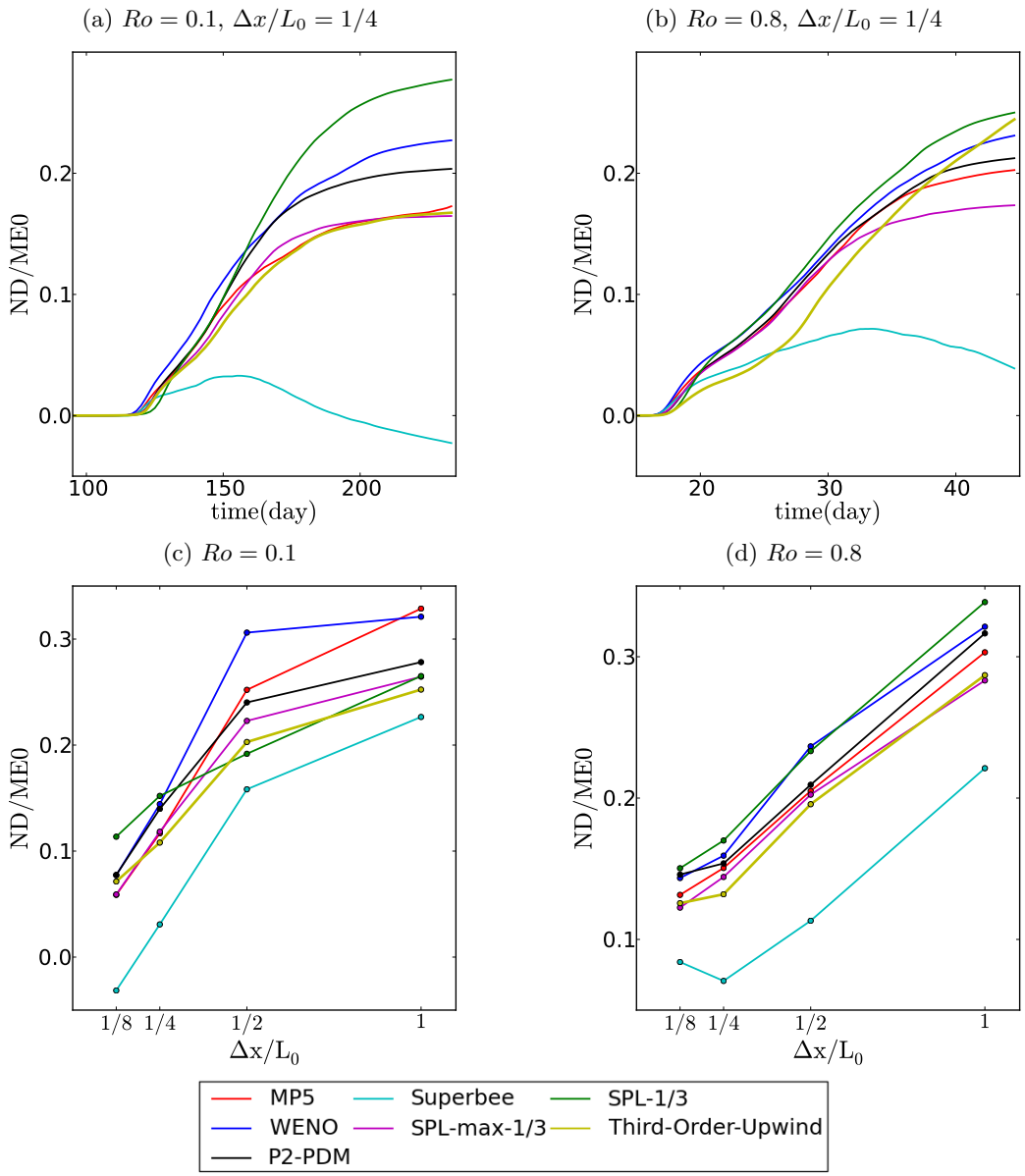

Figure 5.11: Baroclinic instability test case. Ratio of numerical dissipation to total initial mechanical energy. ME0, L_0 and Δx are initial total mechanical energy, initial Rossby radius of deformation and grid size. (a,b): Numerical dissipation of the mesoscale configuration and the submesoscale configuration for resolution C; (c): Numerical dissipation of the mesoscale configuration when approximately 70 % of available potential energy is released; (d): Numerical dissipation of the submesoscale configuration when 65 % of available potential energy is released.

resolution experiments.

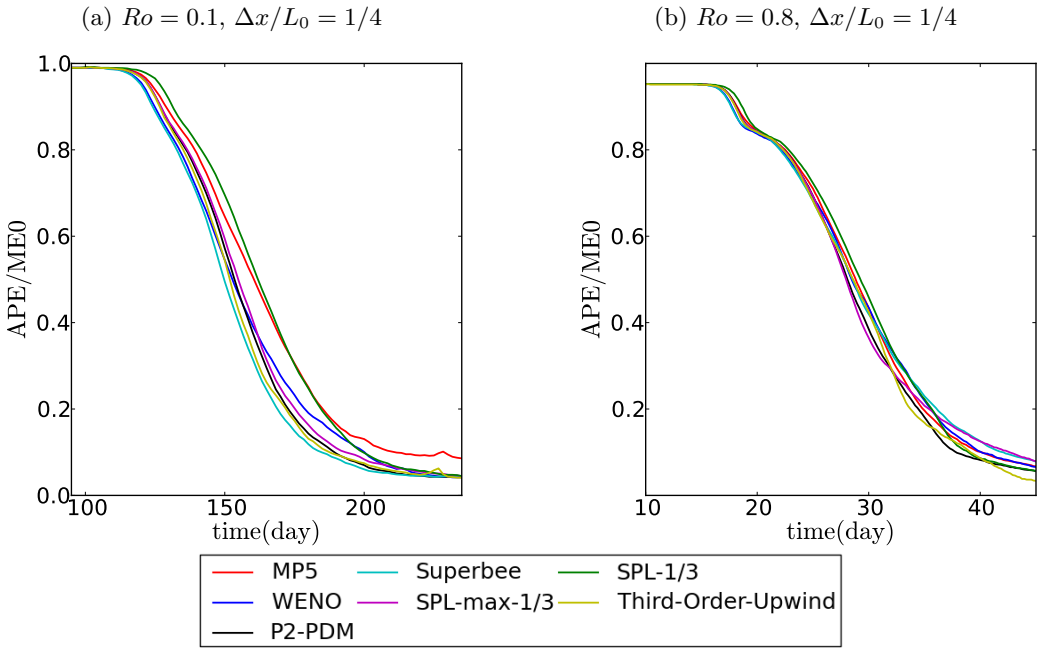

Figure 5.12: Baroclinic instability test case. Available Potential Energy (APE). ME0 is initial total mechanical energy. (a,b): Evolution of available potential energy of the mesoscale configuration and the submesoscale configuration for resolution C.

5.2.4 Eddy kinetic energy

Figures 5.14.a and 5.14.b compare the evolution of eddy kinetic energy for the meso- and submesoscale configurations, respectively. It is shown for both configurations that the Superbee scheme as the antidissipative scheme allows for the highest level of eddy kinetic energy. In addition, the SPL-$\frac{1}{3}$ scheme as the most dissipative scheme generates the lowest level. Thus, positive numerical dissipation decreases the level of final stratification. The comparison of case C of the submesoscale configuration indicates that the results do not clearly discriminate between the advection schemes. Thus, it is concluded that all schemes release a similar level of energy.

5.3 Summary and discussion

This study analyses the diffusive and dissipative effects of advection schemes on baroclinic and lateral shear instability under different dynamical conditions characterised by large and small Rossby numbers. It is shown that the WENO, MP5, Third order upwind, SPL-max-$\frac{1}{3}$

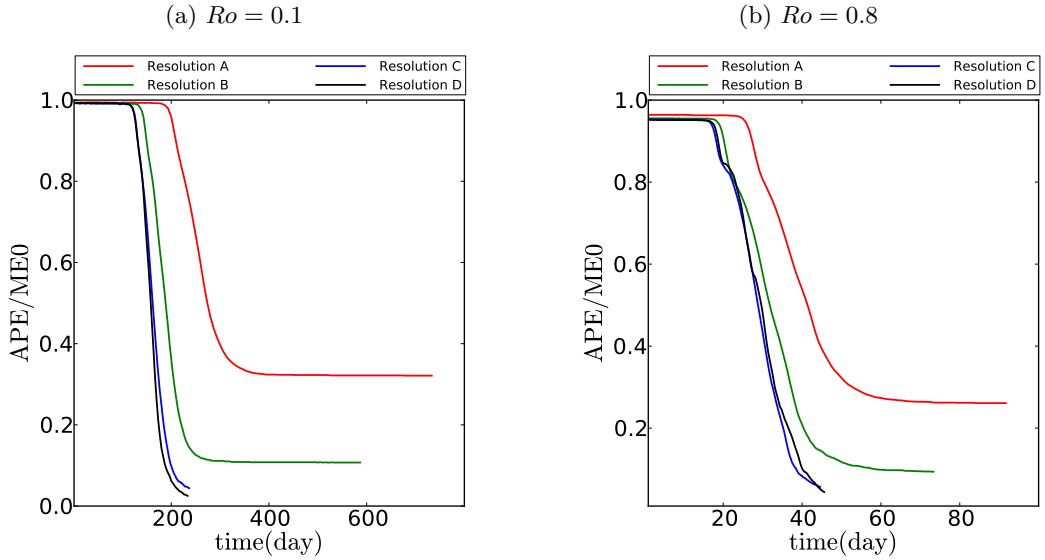

Figure 5.13: Baroclinic instability test case. Available Potential Energy (APE). ME0, is initial total mechanical energy. (a,b): Evolution of available potential energy of the mesoscale configuration and the submesoscale configuration for all resolutions using the SPL-$\frac{1}{3}$ advection scheme.

and P2-PDM advection schemes generate the smallest absolute value of numerical dissipation for dynamical regimes with low and large Ro. When eddies are resolved appropriately, the numerical dissipation and variation of background potential energy of simulations for coarser grids (e.g. case C of the submesoscale configuration of baroclinic instability and case R2 of lateral shear instability) using the MP5 and SPL-max-$\frac{1}{3}$ advection schemes are on the same order or less than the results of finer grids (case D of the submesoscale configuration of baroclinic instability and case R3 of lateral shear instability) using other advection schemes (see for example figures 5.9.d and 5.11.d and Table 5.1). Since MP5 and SPL-max-$\frac{1}{3}$ advection schemes generate the least absolute numerical dissipation in the shear instability test case,

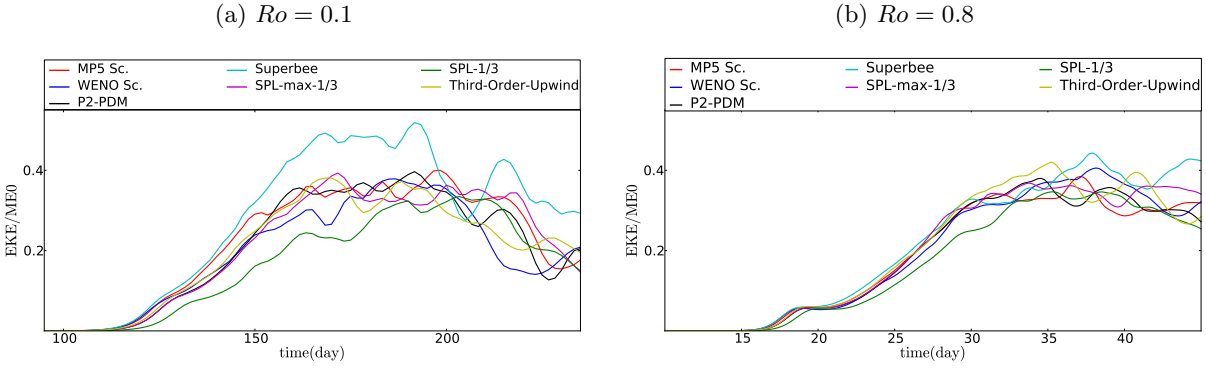

Figure 5.14: Baroclinic instability test case. (a,b): ratio of total Eddy Kinetic Energy (EKE) to total initial mechanical energy for resolution C. ME0 is initial total mechanical energy.

they are considered as the most accurate schemes for the tracer and momentum advection schemes. Furthermore, using a Third order upwind scheme as momentum advection scheme dissipates kinetic energy competitively to using MP5 and SPL-$\frac{1}{3}$ schemes in the baroclinic test case. However, MP5 and WENO schemes take approximately 2.3 times longer than the TVD schemes in our implementation.

The results of all experiments demonstrate that refining the grids reduces the total kinetic energy error and numerical mixing. Consequently, the global numerical viscosity of the lateral shear instability experiment and averaged numerical diffusivity of the configuration with small Ro of the baroclinic instability experiment are decreased. However, increasing the horizontal resolution in the configuration with large Ro increases the numerical diapycnal diffusivity. This might be due to the fact that the eddies are resolved appropriately for the high resolution setups. Therefore, the decrement of the diapycnal discrete gradient of density might be dominant in (3.50).

Energy in the baroclinic instability experiments is dissipated numerically in two phases. In the first phase, which is associated with baroclinic production of eddy kinetic energy, the advection schemes which are recognised as neutral schemes in the lateral shear instability experiment increase BPE approximately 5 percent of initial mechanical energy for all configurations when $\Delta x/L_0 = 1/4$. In addition, for the same resolution the neutral schemes dissipate approximately 15 to 20 percent of initial mechanical energy in all simulations. However, for the mesoscale configuration the diffusive scheme, SPL-$\frac{1}{3}$, and the antidiffusive scheme, Superbee, change BPE two times more than when these schemes are used in the submesoscale configuration. In contrast to the first phase, in the second phase, while turbulence is fully developed, BPE is approximately constant and kinetic energy is dissipated slightly. In general, the numerical dissipation and mixing rate in the first phase are much larger than in the second phase and all schemes are globally dissipative in the first phase. However, for the submesoscale experiment the advection schemes which are known mostly as antidiffusive schemes present partially globally antidissipative and antidiffusive behaviour in the second phase. The possible reason is that both momentum and tracer gradients are sharp in the first phase and smooth in the second phase. Therefore, the local dissipation and mixing rate are mostly positive in the first phase. The global numerical diffusivity in the baroclinic instability test case is increased up to a maximum value which occurs when approximately half of the available potential energy has been released. Then, the numerical diffusivity is diminished gradually. Similarly, the absolute global numerical viscosity in the lateral shear instability experiment is amplified up to a maximum value that occurs when approximately half of the eddy kinetic energy is produced.

It was shown that all advection schemes in the submesoscale configuration generate approximately the same level of eddy kinetic energy. However, when the flow is quasi two-dimensional the dissipative schemes generate less eddy kinetic energy than the antidissipative schemes and the final stratification levels are clearly distinct. In contrast, the final levels of the stratification of the fluid in the submesoscale configuration of all advection schemes are approximately the same.

5.4 Conclusions

The results of this chapter show that all tested advection schemes in the restratification phase of baroclinic instability experiment are numerically dissipative and increase the background potential energy. However, when the governing flow is 2D in both test cases the Superbee advection scheme is antidissipative, and the other schemes are dissipative. Another major outcome is that generally positive global numerical dissipation and positive background potential energy evolution delay the restratification process. Returning to the main question of this study, it is now possible to state that the MP5 and SPL-max-$\frac{1}{3}$ schemes generate the best results, with the MP5 scheme being computationally more demanding but more accurate. Taken together, these results suggest to use either the MP5 scheme as a high-order advection scheme or the SPL-max-$\frac{1}{3}$ scheme as a TVD advection scheme for eddy-resolving ocean models if new mixing parameterisations are to be derived or high accuracy of the results is demanded.

6 Summary and conclusions

This research was undertaken to resolve the ambiguity in selecting advection schemes in oceanic applications. The advection schemes in this research were initially categorised based on their dissipative behaviour performing two idealised 2D experiments. Then, a series of 3D simulations were conducted with the aim of assessing the effects of advection schemes on the restratification process for dynamical regimes with small and large Rossby numbers, interpreted here as mesoscale and submesoscale flows. The variety of the used advection schemes and the applied methodology, the innovation in designing the 2D experiments and the systematic analyses of the effects of advection schemes on the restratification process make this study distinctive and unique.

Previous studies and the 1D numerical advection transport experiment performed in this research have shown that the flux-limited advection schemes cause smearing and squaring effects near discontinuities and maxima in the solution. These effects cause positive and negative local numerical dissipation, respectively. The advection schemes that show positive and negative global numerical dissipation are called dissipative and antidissipative schemes, respectively. The most obvious finding of this study is that advection schemes, especially TVD schemes, do not necessarily present constant dissipative behaviour. For example, the advection schemes categorised as dissipative schemes generate also negative numerical viscosity but in smaller area than the antidissipative schemes. In contrast to dissipative and antidissipative schemes, the neutral schemes (e.g. the SPL-max-$\frac{1}{3}$, MP5 and WENO schemes) dissipate kinetic energy very slightly. For these schemes the regions of negative and positive local numerical viscosity are balanced. The results of the baroclinic instability experiments indicate that all tested advection schemes are dissipated in the restratification phase of the experiments. The results of the baroclinic instability experiments indicate that all tested advection schemes are dissipative in the restratification phase of the experiments. It seems that the dissipation in the restratification phase is mostly due to the vertical momentum and tracer advection schemes. However, when the flow is stratified, the main portion of global numerical dissipation and variation of background potential energy is due to horizontal advection schemes when the dynamics of the flow is 2D. The results of this research support the idea that positive numerical dissipation reduces the level of released eddy kinetic energy and delay restratification. Taken together,

these results suggest that the MP5 and SPL-max-$\frac{1}{3}$ schemes perform much better than other schemes. Although the WENO scheme provides promising accuracy in the 2D experiments, its combination with the P2-PDM advection scheme in 3D experiments is more dissipative and diffusive than the SPL-max-$\frac{1}{3}$. Therefore, for developing new mixing parameterisation on any scale or for performing highly accurate eddy-resolving simulations, it is recommended to use MP5 and SPL-max-$\frac{1}{3}$ schemes.

7 Recommendations for future work

It is recommended that further research be undertaken in the following areas:

1. An issue that was not addressed in this study is a small portion of mechanical energy that is not quantified. This can be seen in the stacked plot in figure 7.1 by comparing the final level of mechanical energy and the initial mechanical energy. This problem was also presented in the the previous studies, see for example Figure 3 of Klingbeil et al. (2014). It seems that this portion of mechanical energy is lost when kinetic energy is extracted from available potential energy due to discretisation errors in internal pressure terms. Analysing the kinetic energy budget might be a clue to find the reasons and to quantify the lost mechanical energy.

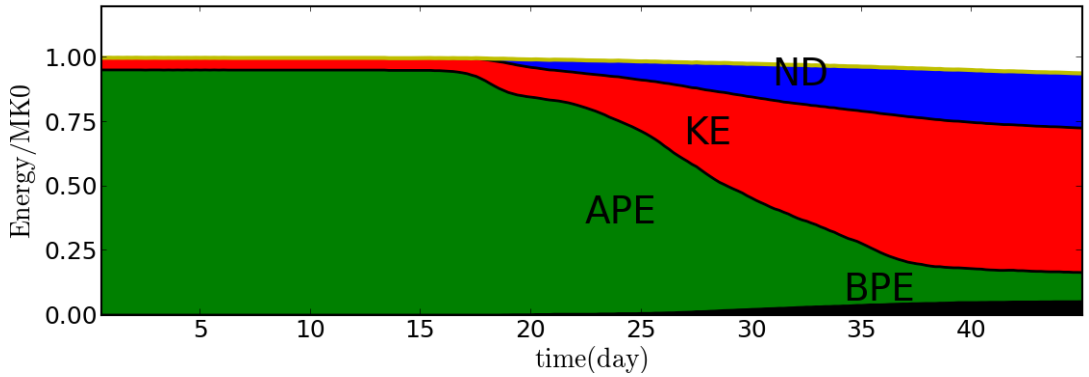

Figure 7.1: Evolution of global energy composition in the baroclinic instability test case. The experiment is performed for $Ro = 0.8$ and $\Delta x/L_0 = 1/4$ using the P2-PDM advection scheme. KE and MK0 are total kinetic energy and initial mechanical energy, respectively. BPE, APE and ND are explained in chapter 3

2. Further research regarding the effects of advection schemes on the pattern of flow would be interesting. As an example, a series of simulations following the work of Tartinville et al. (1998) are performed here to see the effects of advection schemes on the azimuthal wavenumber which was attributed by them to the discretisation errors of the horizontal advection of momentum. This test case consists of a column of relatively light fresh water which is initially in rest. Then, the fluid spreads over the surface because it is lighter than the ambient water.

Length and width of basin	60 km
Horizontal resolution	1 km
Water depth	20 m
Number of vertical layers	20
Coriolis parameter	$1.15 \times 10^{-4}\mathrm{s}^{-1}$
Depth of fresh water lens	10 m
Diameter of fresh water lens	3 km
Salinity within the lens (in psu)	$1.1\left(\frac{d}{3}\right)^{8} + 33.75$
Salinity out of the initial fresh water column (in psu)	34.85

Table 7.1: The resolutions and parameters used in the fresh water lens. d (in km) is the distance from the centre. The diffusivity and viscosity are set to zero. Salinity and water elevation in the boundaries are restored to the ambient water salinity and zero, respectively.

During the geostrophic adjustment, the fast inertial waves radiate out of the centre and the slow flows generate several vortex pairs which rotate around the centre. The simulation is designed here similar to the test case in the work of Tartinville et al. (1998) except that the length and width of the basin is doubled. Table 7.1 summarises the parameters used.

Tartinville et al. (1998) states that according to the results of laboratory experiment (Griffiths and Linden, 1981), the configuration designed for this test case should generate an order-two baroclinic instability. Figure 7.2 shows the results of the simulations after 30 days using the P2-PDM, Superbee, SPL-max-$\frac{1}{3}$, WENO and MP5 advection schemes. The P2-PDM scheme is used for the vertical direction when the WENO and MP5 schemes are selected for the horizontal direction. The last simulation (see figure 7.2.f) used the WENO and SPL-max-$\frac{1}{3}$ schemes for the horizontal direction of the tracer and momentum equations, respectively. The results show that the P2-PDM scheme generates a wavenumber-four instability. In addition, the Superbee and MP5 schemes generate a wavenumber-two instability. However, the resulting dipole structures using the MP5 scheme is much stronger and much more similar to the result of laboratory experiment shown in figure 7.3.a. The SPL-max-$\frac{1}{3}$ scheme generates also two dipole structures, but the fresh water fluid from the original central vortex is not removed completely. Interestingly, the WENO scheme (figure 7.2.e) and the last simulation (figure 7.2.f) produce a wavenumber-three instability. The laboratory results also show asymmetric structures for different initial conditions (see figures 7.3.b and 7.3.c). An explanation for this asymmetric structure might be that the WENO scheme is an adaptive stencil. Therefore, the WENO scheme uses variable coefficients in providing the convex combination of all possible stencils for computing interface values. Although MP5 generates results that are closest to the laboratory experiment, more evidence is still required to definitely conclude that the

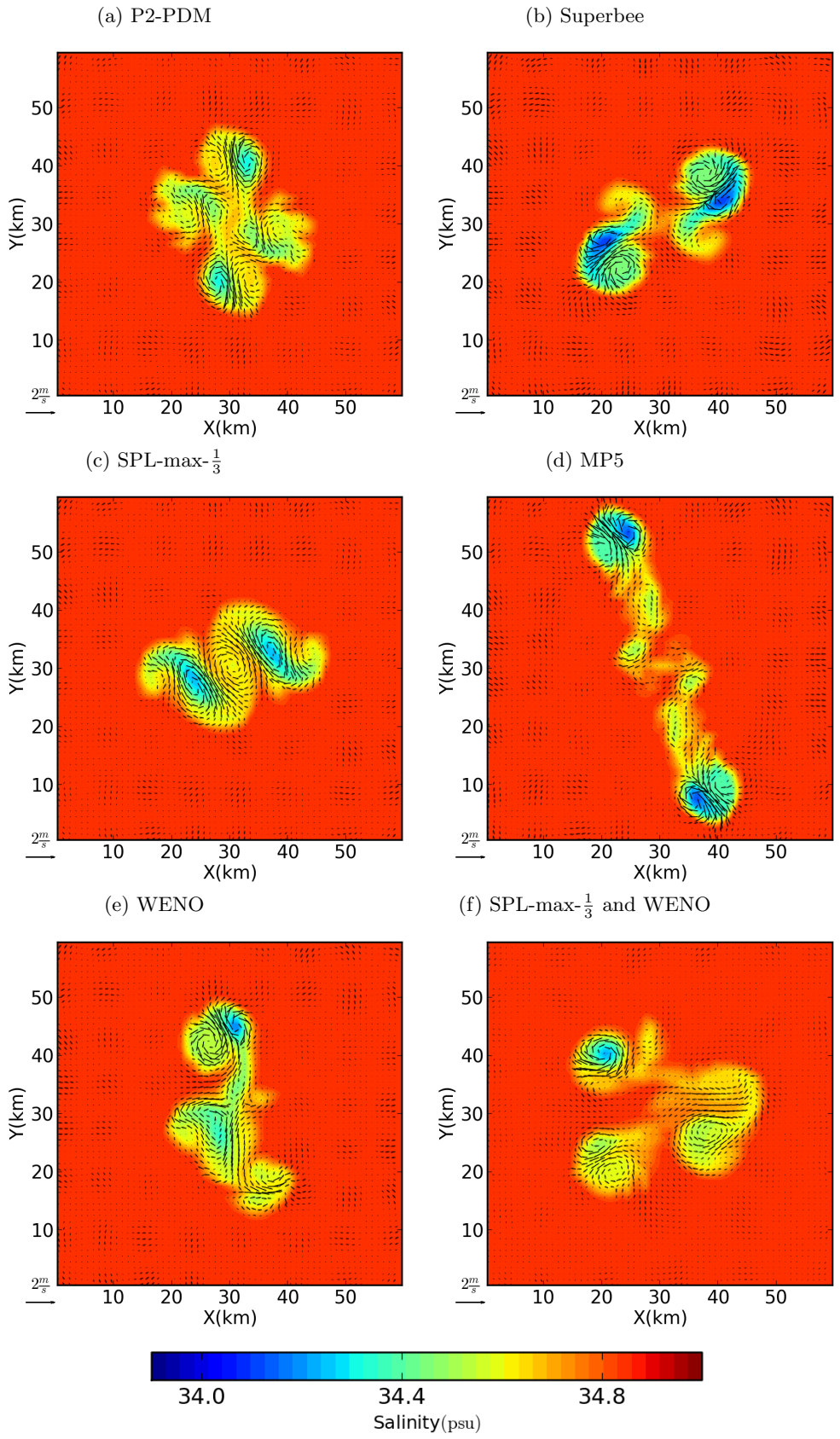

Figure 7.2: Fresh water lens test case. Velocity field (arrows) and sea surface salinity (color code) after 30 days using a) P2-PDM, b) Superbee, c) SPL-max-$\frac{1}{3}$, d) MP5, e) WENO and f) WENO-SPL-max-$\frac{1}{3}$ advection schemes. The contours show the isolines of the salinity in psu.

MP5 scheme generates the best results. Since baroclinic instabilities are very sensitive to initial conditions and there are some differences between laboratory experiment and numerical simulations, recognising the correct result is nontrivial.

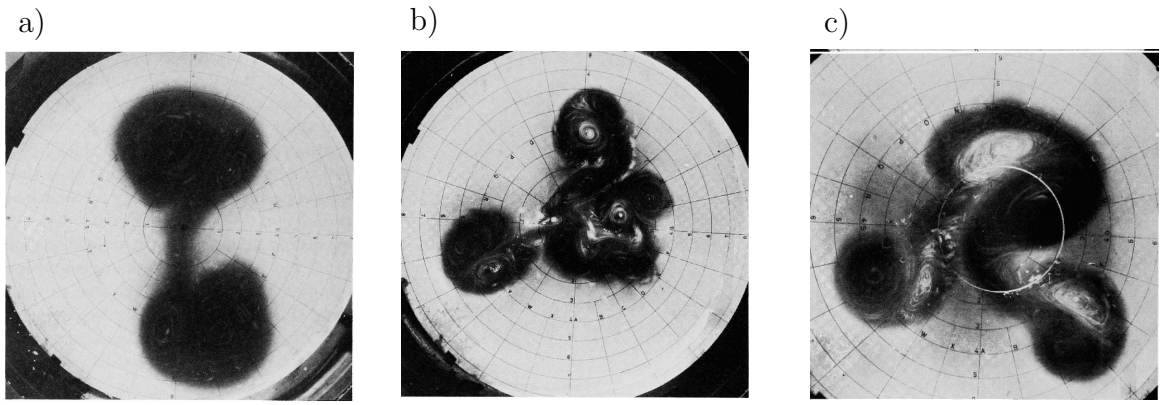

Figure 7.3: Plan view photographs of laboratory experiments (Griffiths and Linden, 1981). (a) Order-two baroclinic instability, two dipole structures separate from each other; (b) Order-three baroclinic instability, this experiment is for a large ratio of the initial height of freshwater column to water depth; (c) Order-three baroclinic instability, anticyclonic parts cover the big area of each dipole.

3. The current research has systematically assessed the effects of advection schemes on restratification processes. In a similar way it would be interesting to analyse the effects of advection schemes on other physical processes such as gravity currents and meridional overturning circulations. The penetration depth of the bottom gravity current and the balanced velocity of meridional overturning circulation might be influenced by the used advection schemes.

4. Although numerical mixing and dissipation are irreversible processes, it might be possible to compute antidissipative fluxes to reduce numerical mixing and dissipation similar to the FCT method. Antidissipative fluxes would be computed using local numerical viscosity. In addition to the methodology suggested in this research, it might be possible to solve a set of equations numerically to forecast the numerical viscosity.

5. A new hybrid advection scheme can be developed deploying local numerical mixing and dissipation analyses. This scheme diagnoses the numerical dissipation in each time step and switches smoothly and locally between dissipative and antidissipative TVD schemes based on the sign and intensity of local numerical dissipation to minimise the numerical effects. This method is very similar to the hybrid method introduced by Fringer and Armfield (2005). Their advection scheme switches globally between diffusive and antidiffusive limiters in case of de-

creasing and increasing background potential energy, respectively.

6. Developing an advection scheme that conserves kinetic energy, enstrophy etc is the aim of several advection schemes, e.g. Ketefian and Jacobson (2009). I suggest that these methods deploy the WENO and MP5 schemes instead of the central method for approximating the interface values. It might reduce the possibility of observing the numerical problems reviewed in chapter 1, although it has been mentioned that the results of the WENO scheme and quadratic conservative schemes are very sensitive to any variations in their algorithms.

Bibliography

Arakawa, A., 1966. Computational design for long-term numerical integration of the equations of fluid motion: Two-dimensional incompressible flow. Part I. *Journal of Computational Physics*, **1**, 119–143.

Arakawa, A., Lamb, V.R., 1977. Computational design of the basic dynamical processes of the UCLA general circulation model. *Methods in Computational Physics*, **17**, 173–265.

Banas, N.S., Hickey, B.M., Newton, J.A., Ruesink, J.L., 2007. Tidal exchange, bivalve grazing, and patterns of primary production in willapa bay, Washington, USA. *Marine Ecology Progress Series*, **341**, 123–139.

Baumert, H.Z., Simpson, J., Sündermann, J., 2005. Marine turbulence: theories, observations, and models. volume **1**. Cambridge University Press.

Bayly, B.J., Orszag, S.A., Herbert, T., 1988. Instability mechanisms in shear-flow transition. *Annual Review of Fluid Mechanics*, **20**, 359–391.

Bell, J.B., Colella, P., Glaz, H.M., 1989. A second-order projection method for the incompressible Navier-Stokes equations. *Journal of Computational Physics*, **85**, 257–283.

Berger, M., Aftosmis, M.J., Murman, S.M., 2005. Analysis of slope limiters on irregular grids. *43rd AIAA Aerospace Sciences Meeting and Exhibit*, **490**, 1–22.

Blanes, S., Casas, F., Murua, A., 2008. Splitting and composition methods in the numerical integration of differential equations. *Boletín de la Sociedad Espaola de Matemática Aplicada*, math.NA, 89–145.

Blumberg, A.F., Mellor, G.L., 1987. A description of a three-dimensional coastal ocean circulation model. *Three-Dimensional Coastal Ocean Models*, **4**, 1–16.

Boccaletti, G., Ferrari, R., Fox-Kemper, B., 2007. Mixed layer instabilities and restratification. *Journal of Physical Oceanography*, **37**, 2228–2250.

Book, D.L., Boris, J.P., Hain, K., 1975. Flux-corrected transport II: Generalizations of the method. *Journal of Computational Physics*, **18**, 248–283.

Boris, J.P., Book, D., 1976. Flux-corrected transport. III. minimal-error FCT algorithms. *Journal of Computational Physics*, **20**, 397–431.

Boris, J.P., Book, D.L., 1973. Flux-corrected transport. I. SHASTA, A fluid transport algorithm that works. *Journal of Computational Physics*, **11**, 38–69.

Borthwick, A.G.L., Kaar, E.T., 1993. Shallow flow modelling using curvilinear depth-averaged stream function and vorticity transport equations. *International Journal for Numerical Methods in Fluids*, **17**, 417–445.

Bott, A., 1988. A positive definite advection scheme obtained by nonlinear renormalization of the advective fluxes. *Monthly Weather Review*, **117**, 1006–1016.

Brüggemann, N., Eden, C., 2014. Evaluating different parameterizations for mixed layer eddy fluxes induced by baroclinic instability. *Journal of Physical Oceanography*, **44**, 2524–2546.

Burbeau, A., Sagaut, P., Bruneau, C.H., 2001. A problem-independent limiter for high-order Runge–Kutta discontinuous Galerkin methods. *Journal of Computational Physics*, **169**, 111–150.

Burchard, H., 2012. Quantification of numerically induced mixing and dissipation in discretisations of shallow water equations. *International Journal on Geomathematics*, **3**, 51–65.

Burchard, H., Bolding, K., Villarreal, M.R., 2004. Three-dimensional modelling of estuarine turbidity maxima in a tidal estuary. *Ocean Dynamics*, **54**, 250–265.

Burchard, H., Hetland, R.D., Schulz, E., Schuttelaars, H.M., 2011. Drivers of residual estuarine circulation in tidally energetic estuaries: Straight and irrotational channels with parabolic cross section. *Journal of Physical Oceanography*, **41**, 548–570.

Burchard, H., Rennau, H., 2008. Comparative quantification of physically and numerically induced mixing in ocean models. *Ocean Modelling*, **20**, 293–311.

Čada, M., Torrilhon, M., 2009. Compact third-order limiter functions for finite volume methods. *Journal of Computational Physics*, **228**, 4118–4145.

Colella, P., Sekora, M.D., 2008. A limiter for PPM that preserves accuracy at smooth extrema. *Journal of Computational Physics*, **227**, 7069–7076.

Colella, P., Woodward, P.R., 1984. The piecewise parabolic method (PPM) for gas-dynamical simulations. *Journal of Computational Physics*, **54**, 174–201.

Crowley, W.P., 1968. Numerical advection experiments I. *Monthly Weather Review*, **96**, 1–11.

Durran, D.R., 2010. Numerical methods for fluid dynamics: With applications to geophysics. volume **32**. Springer.

Eady, E.T., 1949. Long waves and cyclone waves. *Tellus*, **1**, 33–52.

Eden, C., 2010. Parameterising meso-scale eddy momentum fluxes based on potential vorticity mixing and a gauge term. *Ocean Modelling*, **32**, 58–71.

Eden, C., 2011. A closure for meso-scale eddy fluxes based on linear instability theory. *Ocean Modelling*, **39**, 362–369.

Ezer, T., 2006. Topographic influence on overflow dynamics: idealized numerical simulations and Faroe Bank Channel overflow. *Journal of Geophysical Research*, **111**, 1–18.

Farrow, D.E., Stevens, D.P., 1995. A new tracer advection scheme for Bryan and Cox type ocean general circulation models. *Journal of Physical Oceanography*, **25**, 1731–1741.

Fox-Kemper, B., Ferrari, R., Hallberg, R., 2008. Parameterization of mixed layer eddies. part I: Theory and diagnosis. *Journal of Physical Oceanography*, **38**, 1145–1165.

Friedrich, O., 1998. Weighted essentially non-oscillatory schemes for the interpolation of mean values on unstructured grids. *Journal of Computational Physics*, **144**, 194–212.

Fringer, O.B., Armfield, S.W., 2005. Reducing numerical diffusion in interfacial gravity wave simulations. *International Journal for Numerical Methods in Fluids*, **49**, 301–329.

Gerdes, R., Köberle, C., Willebrand, J., 1991. The influence of numerical advection schemes on the results of ocean general circulation models. *Ocean Dynamics*, **5**, 211–226.

Getzlaff, J., Nurser, G., Oschlies, A., 2010. Diagnostics of diapycnal diffusivity in z-level ocean models part I: 1-Dimensional case studies. *Ocean Modelling*, **35**, 173–186.

Godunov, S.K., 1959. A difference method for numerical calculation of discontinuous solutions of the equations of hydrodynamics. *Matematicheskii Sbornik*, **89**, 271–306.

Gottlieb, S., Shu, C.W., 1998. Total variation diminishing Runge-Kutta schemes. *Mathematics of Computation*, **67**, 73–85.

Gottlieb, S., Shu, C.W., Tadmor, E., 2001. Strong stability-preserving high-order time discretization methods. *SIAM Review*, **43**, 89–112.

Griffies, S.M., Pacanowski, R.C., Hallberg, R.W., 2000. Spurious diapycnal mixing associated with advection in a z-coordinate ocean model. *Monthly Weather Review*, **128**, 538–564.

Griffiths, R.W., Linden, P.F., 1981. The stability of vortices in a rotating, stratified fluid. *Journal of Fluid Mechanics*, **105**, 283–316.

Grotjahn, R., 2003. Baroclinic instability. *Encyclopedia of Atmospheric Sciences*, **I**, 179–188.

Harten, A., Engquist, B., Osher, S., Chakravarthy, S.R., 1987. Uniformly high order accurate essentially non-osicillatory schemes, III. *Journal of Computational Physics*, **71**, 231–303.

Harten, A., Zwas, G., 1972. Self-adjusting hybrid schemes for shock computations. *Journal of Computational Physics*, **9**, 568–583.

Hecht, M.W., 2010. Cautionary tales of persistent accumulation of numerical error: Dispersive centered advection. *Ocean Modelling*, **35**, 270–276.

Hirsch, C., 2007. Numerical computation of internal and external flows: The fundamentals of computational fluid dynamics. volume 1. Butterworth-Heinemann.

Hofmeister, R., Burchard, H., Beckers, J.M., 2010. Non-uniform adaptive vertical grids for 3d numerical ocean models. *Ocean Modelling*, **33**, 70–86.

Holland, W.R., Chow, J.C., Bryan, F.O., 1998. Application of a third-order upwind scheme in the NCAR ocean model. *Journal of Climate*, **11**, 1487–1493.

Hólm, E.V., 1995. A fully two-dimensional, nonoscillatory advection scheme for momentum and scalar transport equations. *Monthly Weather Review*, **123**, 536–552.

Hólm, E.V., 1996. Energy and enstrophy conservation properties of high-order non-oscillatory advection schemes. *Tellus*, **48**, 122–137.

Ilıcak, M., Adcroft, A.J., Griffies, S.M., Hallberg, R.W., 2012. Spurious dianeutral mixing and the role of momentum closure. *Ocean Modelling*, **45**, 37–58.

James, I., 2000. A high-performance explicit vertical advection scheme for ocean models: how PPM can beat the CFL condition. *Applied Mathematical Modelling*, **24**, 1–9.

James, I.D., 1996. Advection schemes for shelf sea models. *Journal of Marine Systems*, **8**, 237–254.

Ketefian, G.S., Jacobson, M.Z., 2009. A mass, energy, vorticity, and potential enstrophy conserving lateral fluid–land boundary scheme for the shallow water equations. *Journal of Computational Physics*, **228**, 1–32.

Ketefian, G.S., Jacobson, M.Z., 2011. A mass, energy, vorticity, and potential enstrophy conserving lateral boundary scheme for the shallow water equations using piecewise linear boundary approximations. *Journal of Computational Physics*, **230**, 2751–2793.

Klingbeil, K., Mohammadi-Aragh, M., Gräwe, U., Burchard, H., 2014. Quantification of spurious dissipation and mixing - discrete variance decay in a finite-volume framework. *Ocean Modelling*, **81**, 49–64.

Kundu, P.K., Cohen, I.M., 2008. Fluid Mechanics. Elsevier Academic Press.

Kuvshinov, B.N., Schep, T.J., 2000. Double-periodic arrays of vortices. *Physics of Fluids*, **12**, 32–82.

Lax, P., Wendroff, B., 1960. Systems of conservation laws. *Communications on Pure and Applied Mathematics*, **13**, 217–237.

Lee, M.M., Coward, A.C., Nurser, A., 2002. Spurious diapycnal mixing of the deep waters in an eddy-permitting global ocean model. *Journal of Physical Oceanography*, **32**, 1522–1535.

Leveque, R.J., 2002. Finite volume methods for hyperbolic problems. volume **31**. Cambridge University Press.

Liu, X.D., Osher, S., Chan, T., 1994. Weighted essentially non-oscillatory schemes. *Journal of Computational Physics*, **115**, 200–212.

Mahadevan, A., Oliger, J., Street, R., 1996. A nonhydrostatic mesoscale ocean model. part i: Well-posedness and scaling. *Journal of Physical Oceanography*, **26**, 1868–1880.

Maqueda, M., Holloway, G., 2006. Second-order moment advection scheme applied to arctic ocean simulation. *Ocean Modelling*, **14**, 197–221.

Marsaleix, P., Auclair, F., Floor, J.W., Herrmann, M.J., Estournel, C., Pairaud, I., Ulses, C., 2008. Energy conservation issues in sigma-coordinate free-surface ocean models. *Ocean Modeling*, **20**, 61–89.

McCorquodale, P., Colella, P., 2011. A high-order finite-volume method for hyperbolic conservation laws on locally-refined grids. *Communications in Applied Mathematics and Computational Science*, **6**, 1–25.

Namin, M., Lin, B., Falconer, R., 2004. Modelling estuarine and coastal flows using an unstructured triangular finite volume algorithm. *Advances in Water Resources*, **27**, 1179–1197.

Olbers, D., Willebrand, J., Eden, C., 2012. Ocean Dynamics. Springer.

Patnaik, G., Guirguis, R.H., Boris, J.P., Oran, E.S., 1987. A barely implicit correction for flux-corrected transport. *Journal of Computational Physics*, **71**, 1–20.

Pietrzak, J., 1998. The use of TVD limiters for forward-in-time upstream-biased advection schemes in ocean modeling. *Monthly Weather Review*, **126**, 812–830.

Rennau, H., Burchard, H., 2009. Quantitative analysis of numerically induced mixing in a coastal model application. *Ocean Dynamics*, **59**, 671–687.

Shu, C.W., 1987. TVB uniformly high-order schemes for conservation laws. *Mathematics of Computation*, **49**, 105–121.

Shu, C.W., 1998. Essentially non-oscillatory and weighted essentially non-oscillatory schemes for hyperbolic conservation laws. *Advanced Numerical Approximation of Nonlinear Hyperbolic Equations*, **1697**, 325–432.

Shu, C.W., 2003. High-order finite difference and finite volume WENO schemes and discontinuous Galerkin methods for CFD. *International Journal of Computational Fluid Dynamics*, **17**, 107–118.

Shu, C.W., Osher, S., 1988. Efficient implementation of essentially non-oscillatory shock-capturing schemes. *Journal of Computational Physics*, **77**, 439–471.

Shu, C.W., Osher, S., 1989. Efficient implementation of essentially non-oscillatory shock-capturing schemes, II. *Journal of Computational Physics*, **83**, 32–78.

Skyllingstad, E.D., Samelson, R.M., 2012. Baroclinic frontal instabilities and turbulent mixing in the surface boundary layer. part I: Unforced simulations. *Ocean Modelling*, **42**, 1701–1716.

Smolarkiewicz, P.K., 1984. A fully multidimensional positive definite advection transport algorithm with small implicit diffusion. *Journal of Computational Physics*, **54**, 325–362.

Spekreijse, S., 1987. Multigrid solution of monotone second-order discretizations of hyperbolic conservation laws. *Mathematics of Computation*, **49**, 135–155.

Staniforth, A., Côté, J., 1991. Semi-lagrangian integration schemes for atmospheric models-a review. *Monthly Weather Review*, **119**, 2206–2223.

Stone, P.H., 1966. On non-geostrophic baroclinic stability. *Journal of Atmospheric Sciences*, **23**, 390–400.

Suresh, A., Huynh, H.T., 1997. Accurate monotonicity-preserving schemes with Runge–Kutta time stepping. *Journal of Computational Physics*, **136**, 83–99.

Sweby, P.K., 1984. High resolution schemes using flux limiters for hyperbolic conservation laws. *Numerical Analysis*, **21**, 995–1011.

Tartinville, B., Deleersnijder, E., Lazure, P., Proctor, R., Ruddick, K., Uittenbogaard, R., 1998. A coastal ocean model intercomparison study for a three-dimensional idealised test case. *Applied Mathematical Modelling*, **22**, 165–182.

Taylor, G.I., 1923. On the decay of vortices in a viscous fluid. *The London, Edinburgh, and Dublin Philosophical Magazine and Journal of Science*, **46**, 671–674.

Thomas, L.N., Tandon, A., Mahadevan, A., 2008. Submesoscale processes and dynamics. *Ocean Modeling in an Eddying Regime*, Geophysical Monograph Series 177, 17–38.

Thomson, R.E., Emery, W.J., 2001. Data analysis methods in physical oceanography. Elsevier.

Thuburn, J., 1997. TVD schemes, positive schemes, and the universal limiter. *Monthly Weather Review*, **125**, 1990–1993.

Tremback, C.J., Powell, J., Cotton, W.R., Pielke, R.A., 1987. The forward-in-time upstream advection scheme: Extension to higher orders. *Monthly Weather Review*, **115**, 540–555.

Umlauf, L., Lemmin, U., 2005. Interbasin exchange and mixing in a large lake. The role of long internal waves. *Limnology and Oceanography*, **50**, 1601–1611.

Urakawa, L., Hasumi, H., 2014. Effect of numerical diffusion on the water mass transformation in eddy-resolving models. *Ocean Modelling*, **74**, 22–35.

Vallis, G.K., 2006. Atmospheric and oceanic fluid dynamics: Fundamentals and large-scale circulation. Cambridge University Press.

Van Albada, G.D., Van Leer, B., Roberts Jr, W.W., 1997. A comparative study of computational methods in cosmic gas dynamics. Springer.

Van Leer, B., 1973. Towards the ultimate conservative difference scheme I. the quest of monotonicity. *Proceedings of the Third International Conference on Numerical Methods in Fluid Mechanics*, **18**, 163–168.

Van Leer, B., 1979. Towards the ultimate conservative difference scheme. V. A second-order sequel to Godunov's method. *Journal of Computational Physics*, **32**, 101–136.

Van Leer, B., 1984. On the relation between the upwind-differencing schemes of Godunov, Engquist-Osher and Roe. *Journal on Scientific and Statistical Computing*, **5**, 1–20.

Van Leeuwen, S.M., Van der Molen, J., Ruardij, P., Fernand, L., Jickells, T., 2013. Modelling the contribution of deep chlorophyll maxima to annual primary production in the North Sea. *Biogeochemistry*, **113**, 137–152.

VonNeumann, J., Richtmyer, R.D., 1950. A method for the numerical calculation of hydrodynamic shocks. *Journal of Applied Physics*, **21**, 232–237.

Vreugdenhil, C.B., Wijbenga, J.H.A., 1982. Computation of flow patterns in rivers. *Journal of the Hydraulics Division*, **108**, 1296–1310.

Wang, R., Feng, H., Spiteri, R.J., 2008. Observations on the fifth-order WENO method with non-uniform meshes. *Applied Mathematics and Computation*, **196**, 433–447.

Wang, Y., Hutter, K., 2001a. Comparisons of numerical methods with respect to convectively dominated problems. *International Journal of Numerical Methods in Fluids*, 37, 721–745.

Wang, Y., Hutter, K., 2001b. Comparisons of numerical methods with respect to convectively dominated problems. *International Journal for Numerical Methods in Fluids*, **37**, 721–745.

Waterson, N.P., Deconinck, H., 2007. Design principles for bounded higher-order convection schemes–a unified approach. *Journal of Computational Physics*, **224**, 182–207.

Winters, K.B., D'Asaro, E.A., 1996. Diascalar flux and the rate of fluid mixing. *Journal of Fluid Mechanics*, **317**, 179–193.

Winters, K.B., Lombard, P.N., Riley, J.J., D'Asaro, E.A., 1995. Available potential energy and mixing in density-stratified fluids. *Journal of Fluid Mechanics*, **289**, 115–128.

Winton, M., Hallberg, R., Gnanadesikan, A., 1998. Simulation of density-driven frictional downslope flow in z-coordinate ocean models. *Journal of Physical Oceanography*, **28**, 2163–2174.

Yang, H.Q., Przekwas, A.J., 1992. A comparative study of advanced shock-capturing shcemes applied to Burgers' equation. *Journal of Computational Physics*, **102**, 139–159.

Zahran, Y.H., 2009. An efficient TVD-WENO method for conservation laws. *Numerical Methods for Partial Differential Equations*, **25**, 1443–1467.

Zalesak, S.T., 1979. Fully multidimensional flux-corrected transport algorithms for fluids. *Journal of Computational Physics*, **31**, 335–362.

Zalesak, S.T., 1987. A preliminary comparison of modern shock-capturing schemes: Linear advection. *Advances in Computer Methods for Partial Differential Equations*, **VI**, 15–22.

Zerroukat, M., Staniforth, A., Wood, N., 2010. The monotonic quartic spline method (QSM) for conservative transport problems. *Journal of Computational Physics*, **229**, 1150–1166.

Zerroukat, M., Wood, N., Staniforth, A., 2002. SLICE: A semi-lagrangian inherently conserving and efficient scheme for transport problems. *Quarterly Journal of the Royal Meteorological Society*, **128**, 2801–2820.

Zerroukat, M., Wood, N., Staniforth, A., 2005. A monotonic and positive–definite filter for a Semi-Lagrangian inherently conserving and efficient (SLICE) scheme. *Quarterly Journal of the Royal Meteorological Society*, **131**, 2923–2936.

Zerroukat, M., Wood, N., Staniforth, A., 2006. The parabolic spline method (PSM) for conservative transport problems. *International Journal for Numerical Methods in Fluids*, **51**, 1297–1318.